

Ultrafast Carrier and Magnetization Dynamics in EuO

M.C. Donker

Master Thesis

Supervisors: Dr. D.A. Mazurenko and prof. dr. ir. P.H.M. van Loosdrecht

Referent: Prof. dr. P. Rudolf

Period: September 2005 - August 2006

Group: Optical Condensed Matter Physics

Place: University of Groningen Materials Science Centre

Contents

1	Introduction and Outline	5
2	Theory	7
2.1	Physical Properties of Europium Oxide	7
2.1.1	Structure	7
2.1.2	Magnetic Properties	7
2.1.3	Transport Properties	8
2.1.4	Optical Properties	11
2.1.5	Magneto- Optical Kerr Effect and Faraday Effect	13
2.2	Electronic Configuration	13
2.2.1	Ground State of an Eu^{2+} - ion	13
2.2.2	$4f^7$ Configuration in the Hubbard Model	14
2.2.3	Energy of $4f^7$ Excited State Configurations	15
2.2.4	$5d^1$ Excited State Configuration in a Crystal Field	16
2.3	Exchange Interactions	19
2.3.1	$5d^1$ Configuration and Superexchange Interactions	19
2.3.2	Exchange Interactions in EuO	20
2.3.3	Exchange Interactions in the Eu Chalcogenides	22
2.3.4	Pressure Effects	22
2.3.5	EuO in the Ferromagnetic Kondo Lattice Model	22
2.3.6	$5d^1$ Excited State in the Degenerate Hubbard Model	25
2.3.7	Magnetism in the $4f^65d^1$ Excited State	26
2.4	Eu-rich EuO and Gd-doped EuO	27
2.5	Conclusion: Exchange Interactions in EuO	28
2.6	Magneto Optical Kerr Effect	29
2.6.1	Microscopic Mechanism	29
2.6.2	Macroscopic Description	30
2.7	TRMOKE Experiments in Literature	35
2.7.1	Carrier Dynamics in Semiconductors	35
2.7.2	Magnetization Dynamics in Magnetic Semiconductors	37
2.7.3	Conclusion	39
3	Hysteresis and Transient Hysteresis	40
3.1	Experimental Setup	40
3.2	Growth of EuO Films	42
3.2.1	Growth Conditions	42
3.2.2	Sample Characteristics	43
3.3	Results	44

3.3.1	Hysteresis Measurements	44
3.3.2	Transient Hysteresis Measurements	50
4	Transient Kerr Rotation and Reflectivity	63
4.1	Transient Kerr Rotation Measurements	63
4.2	Transient Reflectivity Measurements	64
4.3	Discussion and Conclusion	64
5	Conclusion and Outlook	67
6	Acknowledgements	69
A	Hysteresis	75
B	Transient Hysteresis	81
C	Transient Kerr Rotation	95
D	Transient Reflectivity	99

Chapter 1

Introduction and Outline

In this master thesis, a ferromagnetic semiconductor is studied. Ferromagnetic semiconductors are important in the field of spintronics since the spin injection from a semiconductor into another semiconductor can be more efficient than from a ferromagnetic metal into a semiconductor because of the absence of a Schottky barrier. For possible applications one would like to be able to control the magnetism and the conductivity in the ferromagnetic semiconductor. The properties of a material can be changed using strong femtosecond laser pulses. It is already known that in the diluted magnetic semiconductor (Ga,Mn) As, the magnetization can be increased using circularly polarized laser pulses [1]. In those experiments, the angular momentum of the photon has been used to increase the magnetization by generating a photoinduced spin polarization. In this thesis we report on a study of the ultrafast magnetization dynamics in a ferromagnetic semiconductor, EuO, in which the magnetization can be increased using linearly polarized light. The magnetic moments in EuO reside on the europium ion ($4f^7$) and the exchange interaction is thought to be mediated by the conduction electrons in the hybridized oxygen 2p-europium 5d conduction band. It is already known that when the conduction band is populated by chemical doping, the ordering temperature in (Eu,Gd)O can be increased by 100 K with respect to stoichiometric EuO [2], which has a magnetic ordering temperature of 69 K. In our experiments, the conduction band was populated optically, using 800 nm femtosecond linearly polarized laser pulses. By the use of this strong femtosecond laser pulses, one can try to control the magnetism and the conductivity of EuO. The induced changes in the magnetization and in the conduction band population have been studied using time-resolved magneto-optical Kerr effect and transient reflectivity experiments, respectively.

The organization of this thesis is as follows. In the first part of the Theory chapter 2, the physical properties of EuO are discussed: the magnetic properties, the transport properties and the optical properties. In the second part of the chapter, the magnetic properties are discussed in more detail: why is EuO ferromagnetic and how can the conduction electrons change the magnetic properties. The introduced models are very general and will give some insight what can happen after a strong optical excitation.

In order to study the magnetization and carrier dynamics, femtosecond laser pulses are used. A strong pump pulse can excite the system. By looking to the rotation of polarization of the reflected linear polarized probe pulse, we are able to study the magnetization dynamics on short timescales, since the rotation of polarization is proportional to the magnetization. This so-called Kerr effect is described in the Theory chapter as well. At the end of the chapter 2, the carrier dynamics in semiconductors and the magnetization dynamics in magnetic semiconductors are discussed. Finally, in chapters 3 and 4, the experimental setup, the film growth in Köln, the transient hysteresis, transient Kerr rotation and the transient reflectivity data are shown and discussed. There are large differences in the measured width and the height of the hysteresis loops of samples grown in (almost) the same conditions. On samples number 1 and 4 in the text, transient hysteresis measurement were performed. In EuO, the magnetization can be increased using 800 nm linearly polarized femtosecond laser pulses. At most temperatures, the induced effect increases towards an induced magnetization during the first 50 ps but decreases after 100 ps. The details are discussed in the chapter 3 and 4. Chapter 5 gives the final conclusion and an outlook.

Chapter 2

Theory

2.1 Physical Properties of Europium Oxide

This section is devoted to the physical properties of EuO. First the structural and magnetic properties are discussed followed by the transport properties and the optical properties. Some important physical properties of EuO are introduced like the Colossal Magneto Resistance (CMR), the spin splitting of the conduction band, the Metal Insulator Transition, the large Kerr effect and the effect of the chemically doping with Gd. The second section of this chapter discusses the origin of the ferromagnetism in EuO by describing the exchange interactions.

2.1.1 Structure

EuO has a rocksalt structure (spacegroup $Fm\bar{3}m$ nr. 225) with a lattice constant of 5.144 Å at room temperature and a lattice constant of 5.127 Å at 10 K. The divalent europium ions are octahedrally surrounded by divalent oxygen ions, as can be seen in figure 2.1 [3].

2.1.2 Magnetic Properties

Stoichiometric EuO has a ferromagnetic ordering temperature of 69.3 K. The saturation magnetization at 0 K is 1910 Gauss/ cm³ which corresponds to 6.8 μ_B per formula unit [4] [5]. When the magnetic susceptibility is fitted to the Curie-Weiss law, a paramagnetic Curie-Weiss temperature of 70.6 K is obtained which is very close to the ferromagnetic orderings temperature:

$$\chi = \frac{C}{T - \theta} \quad (2.1)$$

χ is the magnetic susceptibility, C the Curie constant, T the temperature and θ is the Curie-Weiss temperature. The paramagnetic effective magneton number calculated from the Curie constant C is 8.15 μ_B . The calculated value with the total angular momentum J=3.5, the spin angular momentum S=3.5 ($4f^7$) and the orbital angular momentum L=0 gives a g-factor of two and effective Bohr magneton number of 7.94 μ_B , which is close to the experimental

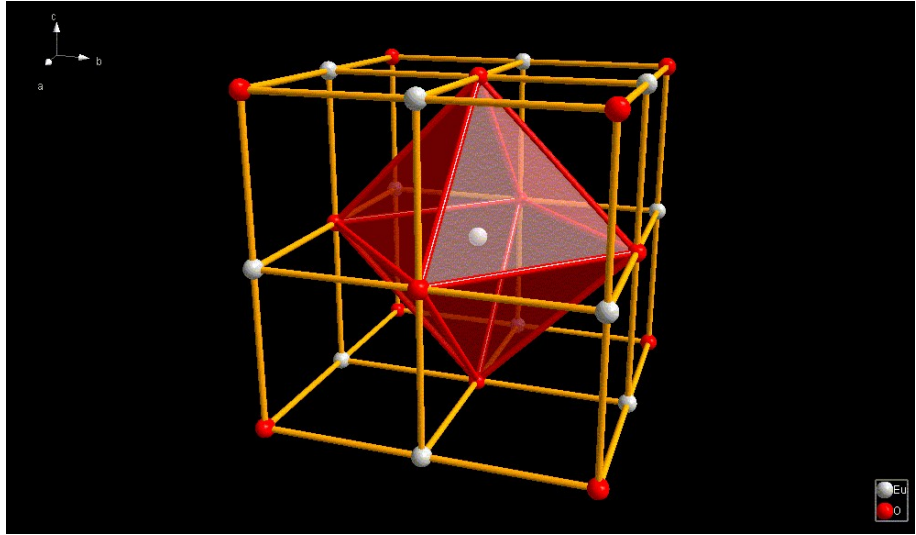


Figure 2.1: Crystal structure of EuO. The white and red balls represents europium and oxygen ions respectively.

value of $8.15 \mu_B$. Even in the absence of orbital angular momentum in the ground state, EuO has an easy axis of magnetization in the [111] direction [6]. The anisotropy energy in spherical coordinates is given by:

$$E = K_1(1/4\sin^2\theta\sin^22\phi + \cos^2\theta)\sin^2\theta + \frac{K_2}{16}\sin^22\phi\sin^22\theta\sin^2\theta \quad (2.2)$$

In which K_1 and K_2 are the anisotropy constants and θ and ϕ are the colatitude and the longitude respectively. For EuO K_1 is -0.00927 meV per Eu ion at 4 K and $K_1 \gg K_2$ [6] which is equal to $4.4 \times 10^4 J/m^3$. For comparison, the anisotropy constant in cobalt is $5 \times 10^5 J/m^3$. The reason for this, according to [7],[8], is the splitting of the $^8S_{7/2}$ levels of the 4f electrons in the octahedral crystal field, creating a single ion anisotropy.

2.1.3 Transport Properties

Resistivity and Mobility

The temperature dependence of the resistivity of stoichiometric EuO is shown in figure 2.2 (denoted by "dark") and is like a normal non-magnetic semiconductor with a bandgap of 1.2 eV. According to band structure calculations, EuO has an indirect band gap (X_{4f} to Γ_{6s} point) but close to this there is a direct band gap ($X_{4f \rightarrow 5d}$ point) [9]. However, the authors from [10] doubt if this is correct. They expect the 5d levels to have the lowest energy in the conduction band.

Below the ordering temperature, the conduction band is split into a spin up and a spin down band. The spin splitting follows the behavior of the magnetization: it is large at low temperatures and disappears at the ordering temperature. The spin splitting at 10 K is 0.6 eV, as determined by Steeneken *et al.* [3] and

the conduction electrons are fully spin polarized. In general, the electron and hole current density can be written as [4]:

$$\vec{J}_n = q\mu_n n \vec{E} \quad (2.3)$$

$$\vec{J}_h = -q\mu_p p \vec{E} \quad (2.4)$$

in which μ is the mobility, n is the electron density, p is the hole density, \vec{E} is the electric field and q is the elementary charge. Since the holes are more localized because they are in the 4f valence band, the conduction will be dominated by 5d electrons as is confirmed by Hall experiments [11]. In order to change the resistivity ρ , either the mobility μ or the electron concentration n has to change as can be seen from the following equations. The equation for the carrier density, n , holds for an intrinsic semiconductor:

$$\rho = \frac{1}{ne\mu_n + pe\mu_p} \quad (2.5)$$

$$\mu_n = \frac{e\tau}{m_n} \quad (2.6)$$

$$n(T) = 2 \left(\frac{k_B T}{2\pi\hbar^2} \right)^{3/2} (m_n m_p)^{3/4} e^{\frac{-E_g}{2k_B T}} \quad (2.7)$$

The electron mobility depends on the scattering time τ and the effective mass of the electron and hole, m_n and m_p , respectively. E_g is the value of the bandgap. No mobility measurements of stoichiometric EuO seem to be reported in the literature. The samples that were used in literature to measure the scattering time and carrier concentration show a metal insulator transition, indicating that the samples were not stoichiometric but europium rich, as shall be discussed in paragraph 2.4. The scattering time in Eu-rich EuO was found to be of the order of 10^{-15} s as was measured optically (in the Drude model) in a range of from 30 K to 150 K [3], [12]. The scattering time in one sample decreases from 2×10^{-14} s at 35 K to 1×10^{-15} s at 70 K and after that increases to 5×10^{-15} s at 150 K. The carrier concentration in this region show a similar behavior. It decreases from $1.0 \times 10^{20}\text{cm}^3$ at 30 K to $1.5 \times 10^{18}\text{cm}^3$ at 70 K and increases after that to $2.0 \times 10^{18}\text{cm}^3$ at 150 K. The mobility can now be calculated assuming an effective mass of two [12] and using the described scattering times. A value of $35 \text{ cm}^2\text{V}^{-1}\text{s}^{-1}$ at 30 K was obtained which is a bit lower than the experimental value determined from Hall experiments: $\sim 100 \text{ cm}^2\text{V}^{-1}\text{s}^{-1}$ [13] at 4 K. The Hall mobility has a value of $\sim 10 \text{ cm}^2\text{V}^{-1}\text{s}^{-1}$ around T_c , increases then slightly with increasing temperature and amounts to $\sim 20 \text{ cm}^2\text{V}^{-1}\text{s}^{-1}$ at 298 K.

If we assume that the effective mass is not dependent on temperature, the scattering time has to change with temperature in order to change the mobility. The scattering of electrons in semiconductors originates mainly from defects and phonons. The defect part is usually temperature independent, in contrast to the phonon contribution which is temperature dependent. At higher temperatures there are more phonons from which the electron can scatter and the mobility will decrease with temperature. In magnetic semiconductors electrons

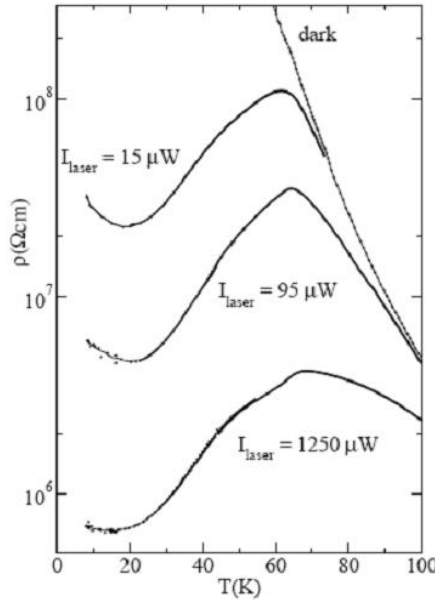


Figure 2.2: The temperature dependance of the photoconductivity of stoichiometric EuO , excited by a He-Ne laser ($\lambda = 632.8\text{nm}$) [3].

also may scatter on spin fluctuations. This scattering mechanism may play a dominant role near the ordering temperature [10][14]. The free carriers can have an indirect exchange interaction with the spin system:

$$H_{df} = -J \sum_i \sigma_i S_i \quad (2.8)$$

In which J is the df exchange constant, S is the spin angular moment of the impurity and σ is the conduction band spin operator. The magnetic scattering is used to explain the peak in the temperature dependance of the resistivity in Eu-rich and Gd-doped EuO . It was found [10] that an applied magnetic field can reduce these spin fluctuations and can result in the disappearance of the peak in the resistivity at higher magnetic fields. No peak or kink in the temperature dependence of the resistivity was seen in stoichiometric EuO .

Photoconductivity

The temperature dependent resistivity in figure 2.2 reveals that when stoichiometric EuO is illuminated by $15 \mu\text{W}$ 632.8 nm laser light, a metal insulator transition around the magnetic orderings temperature occurs. The transition occurs at $\sim 62 \text{ K}$ for $15 \mu\text{W}$ and at $\sim 68 \text{ K}$ for $1250 \mu\text{W}$. The change of the photoconductivity compared with the normal conductivity can be described by [15]:

$$\Delta\sigma = \Delta n e \Delta\mu \quad (2.9)$$

This equation tells that the MIT can occur because of a change in carrier concentration or due to changes in the mobility. The MIT in Eu-rich EuO is sometimes explained by the fact that electronic levels from electrons that are bound to oxygen vacancies, merge with the conduction band when the conduction band is shifted at the orderings temperature [11]. Similar to this, some authors explain the MIT by magnetic excitons [3] [16] consisting of a 5d electron and localized 4f hole which become dissociated at the orderings temperature and induce the MIT. In this way the MIT occurs due to an increase of free photocarriers. The discussion will be continued in paragraph 2.4, which is the paragraph about Eu-rich EuO.

The Hall mobility of the photoelectrons in stoichiometric EuO at 26 K was found to be independent of applied magnetic field and equals $250 \text{ cm}^2 \text{V}^{-1} \text{s}^{-1}$ [18]. In contrast, at 60 K, the mobility depends strongly on the applied magnetic field. At zero magnetic field it equals $90 \text{ cm}^2 \text{V}^{-1} \text{s}^{-1}$ but increases to 160 $\text{cm}^2 \text{V}^{-1} \text{s}^{-1}$ at 15 kOe. Therefore the authors of [18] concluded that the negative magneto- (photo) resistance near T_c can be explained by a change in the mobility.

Long relaxation times for $\Delta\sigma$ have been observed. $\Delta\sigma$ is the relative change in conductivity to the dark conductivity after stopping the illumination. At 15 K, $\Delta\sigma$ was 10 percent after 3000 s [3] and at 60 K, $\Delta\sigma$ was 0.6 percent after 800 s. The long relaxation time of $\Delta\sigma$ is thought to be caused by electrons that were excited to the spin minority band and can not recombine with valance band holes. The transition to these valance band levels is only weakly allowed by spin-orbit coupling. An alternative explanation is based on the assumption that the electrons are trapped in deep impurity levels and can live long. The electrons can be thermally excited from these levels and contribute to the conduction.

2.1.4 Optical Properties

Absorption Spectrum

The absorption spectrum of EuO is shown in figure 2.3. The first peak in the absorption spectrum, figure 2.3 A), was attributed by Mauger [10] to the Eu 4f- $5d_{t2g}$ transition, the second peak at 4.2 eV to the 4f-6s/6p transition, the third peak at 4.9 eV to the oxygen 2p-5d $_{t2g}$ transition, and the fourth peak at 5.2 eV as the 4f to 5d $_{eg}$ transition. In the absorption spectra of other Eu ions like EuF₂, a multiplet structure was attributed to different 4f⁶ terms: $J_{4f} = 0 \dots 6$. In EuO this multiplet is not observable due to the broadening of the peaks, however the (magneto-optical) spectrum does show a signature of the 4f⁶ multiplet[3].

From the temperature dependence of the absorption edge shown in figure 2.3B), one sees that in an applied magnetic field of 0.2 T, the absorption edge at lower temperature, is shifted with respect to the absorption edge at higher temperatures. This shift appears above the critical temperature, at a temperature higher than the MIT transition temperature. This is in contrast to the spin splitting in the 5d conduction band observed in spin resolved X-ray Absorption Spectroscopy (XAS) by Steeneken [3] in which the spin splitting

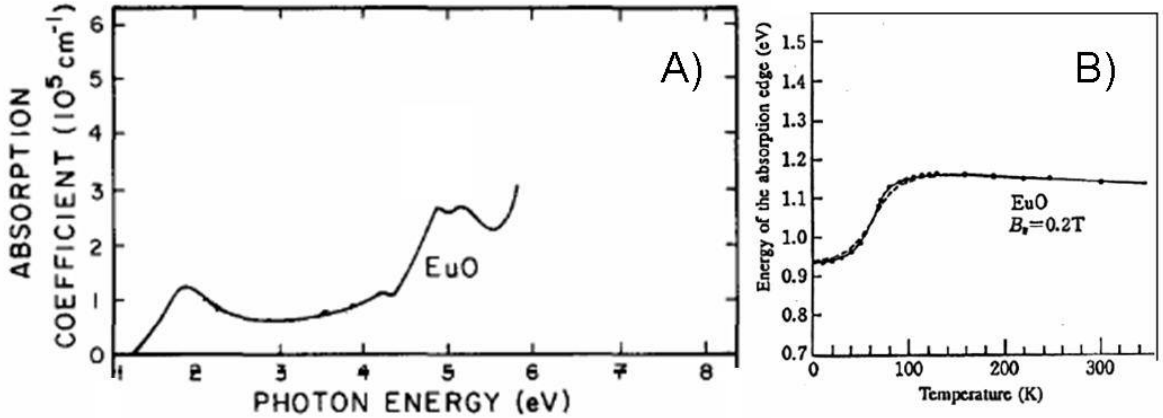


Figure 2.3: A) Absorption spectrum of EuO. B) shift of absorption edge induced in an external magnetic field of 0.2 T (see solid line) [10].

disappears above the critical temperature. In the normal absorption measurements in which a 4f to 5d transition is made, the 5d conduction electron can form a magnetic exciton with a 4f hole. Since above T_c there may be some short range order, still a magnetic exciton can be formed in which the electron is bound by exchange interaction. However, in the XAS measurement where an oxygen to Eu (5d) transition is made, the hole is on the oxygen ion and is separated from the $5d_{t_{2g}}$ europium electrons and no exciton can be formed, as was suggested by Steeneken [3].

There is one big difference between the two described experiments. In the XAS measurements the sample was remanently magnetized and the magnetization becomes zero at above the ordering temperature. However, the absorption edge experiments were done at 0.2 T which results in a non-zero magnetization at all temperatures. When the shift is proportional to the magnetization, this can (partly) explain the difference between the results.

Density of States

Steeneken [3] proposed the following (very) schematic picture of the density of states of EuO shown in figure 2.4. It costs 5.4 eV to flip one 4f spin. At 10 K, the Eu 5d conduction band is spin split by 0.6 eV. However the density of states diagram is drawn for 0 K and for $T > T_c$. The crystal field splitting of the 5d conduction band is about 2.0 eV. The valence band is a Eu 4f band. Below the valence band are the oxygen 2p bands situated.

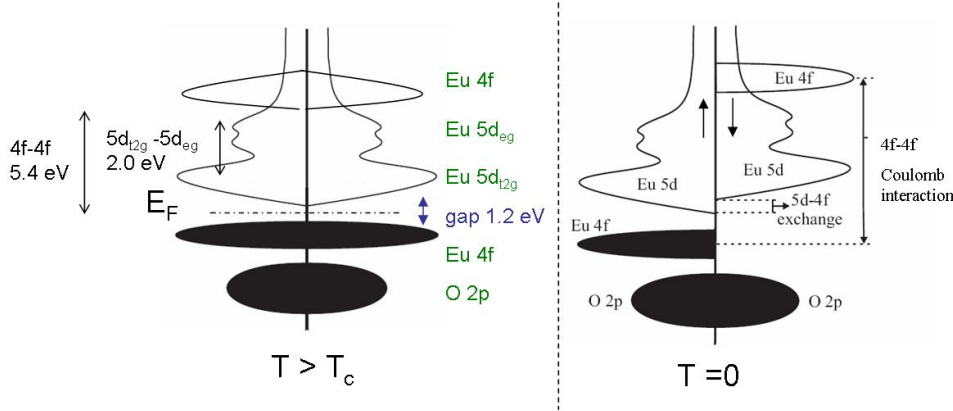


Figure 2.4: *Density of states above and below the orderings temperature. In the right picture the conduction band is spin split. The spin up and spin down part of the density of states is separated by the vertical black solid line.*

2.1.5 Magneto- Optical Kerr Effect and Faraday Effect

The magneto-optical Kerr spectrum of EuO is shown in figure 2.5. The Kerr effect is described in the next chapter: It is the rotation of polarization of light upon reflection from a magnetic medium. Apart from a rotation of polarization, the polarization also becomes elliptical. In the experiments 800 nm (1.55 eV) light is used. Both the Kerr rotation (θ) and the ellipticity (ε) have a maximum here and are large, as seen in figure 2.5. Depending on the wavelength, the magnitude as well as the sign of the Kerr rotation and ellipticity can differ. The analog of the magneto-optical Kerr effect in transmission geometry is called the Faraday effect. The Faraday spectrum of stoichiometric EuO is shown in figure 2.6. The resonances originate from europium 4f to 5d transition and from oxygen 2p to europium 5d transitions. The Kerr spectrum can be partly explained from the differences in absorption for right and left polarized light. For an Eu^{2+} ion in an cubic crystal field, the calculated spectrum, which is similar to the measured spectrum, arises from the different energies from the $4f^6$ final states and from the crystal field splitting energy of 2 eV for the difference in energy for the e_g and t_{2g} orbitals. The details of this calculations are described in paragraph 2.6.1.

2.2 Electronic Configuration

2.2.1 Ground State of an Eu^{2+} - ion

EuO is a ferromagnetic semiconductor and has an orderings temperature of 69.3 K. This section attempts to explain the source of the ferromagnetism in EuO. The discussion will start from the electronic configuration of free europium and free oxygen ions. Then different exchange processes are discussed. The oxygen

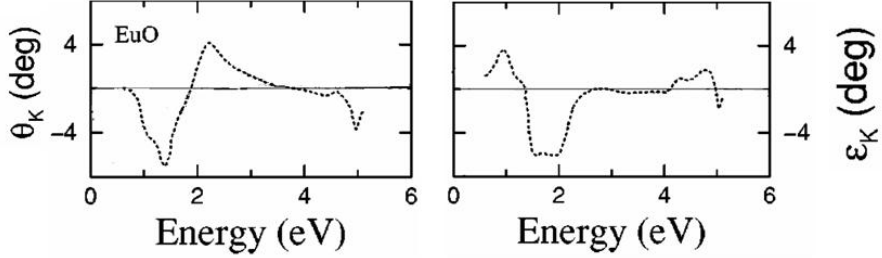


Figure 2.5: *Kerr spectrum of EuO* (figure adapted from [9]).

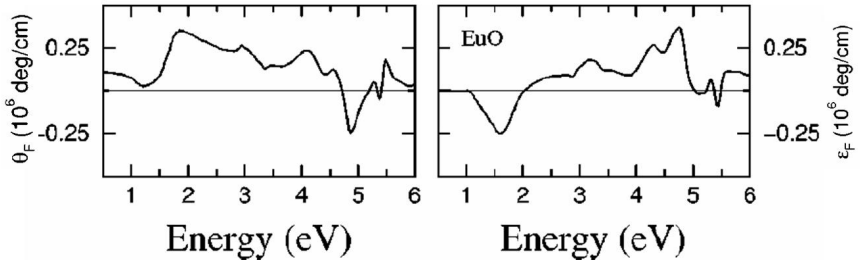


Figure 2.6: *Faraday spectrum of EuO* (figure adapted from [9]).

ions have a ‘non magnetic’ $1s^22s^22p^6$ electronic configuration [3]. However, the europium ions have a $[Xe]4f^75d^06s^0$ configuration and are magnetic. According to Hund’s first rule, Eu^{2+} ions have maximum spin configurations: $S=7/2$. Because of this, the electrons occupy states with $m_L = -3 \dots +3$, and the total orbital angular is zero: $L=0$. This gives a $^8S_{7/2}$ term as ground state.

2.2.2 $4f^7$ Configuration in the Hubbard Model

A situation is considered where the europium atoms and oxygen atoms form a crystal. The properties of the ions are modified by the crystal field. The influence of the crystal field on the 4f europium valence band is different from the influence on the 5d europium conduction band since the 4f orbitals are more localized than the 5d orbitals [3]. The localized nature of the 4f orbitals makes the intra-atomic Coulomb interaction very strong. Without the presence of the 5d conduction band this will make it a so-called Mott-Hubbard insulator. The Hubbard model describes the case of strong electron-electron interaction and starts from the tight-binding model with only on-site interaction. The Hamiltonian for a non-degenerate system looks like [19] [20]:

$$H = t \sum_{\langle ij \rangle, \sigma} c_{i,\sigma}^\dagger c_{j,\sigma} + U \sum_i n_{i,\uparrow} n_{i,\downarrow} \quad (2.10)$$

In which t is the transfer integral, $c_{i,\sigma}^\dagger$ is the creation operator of an electron on site i with spin σ , $c_{i,\sigma}$ is the annihilation operator, U is a measure of the on site Coulomb energy, and $n_{i,\uparrow}$ is the number operator of an electron with spin \uparrow at site i . In this model there is one electron and one level per site. Two electrons, one spin up and one spin down, can occupy one level. The situation in EuO where there are seven electrons and seven degenerate levels per site, is similar to this case. Due to the small 4f orbitals in EuO, t is small and U is large. To minimize its kinetic energy, an electron will try to go from one site to another site that becomes double occupied. However, to create a pair at one site it costs an energy U . In figure 2.7 is shown that there is no possibility for hopping, in the Hubbard model, when the spins are parallel because of the Pauli exclusion principle. However when the spins are antiparallel, hopping is possible but is cost an energy U .

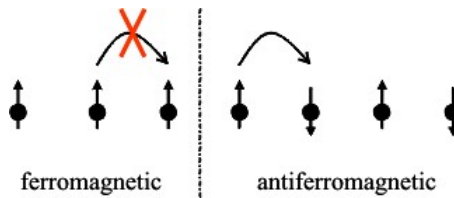


Figure 2.7: In the Hubbard model, where there is one electron per site, hopping is only possible when the spins are aligned.

Mott-Hubbard insulators have a tendency to antiferromagnetism, as can be shown in the case that there is only one electron (and one level) per site. When the kinetic energy part of the Hamiltonian is taken as a perturbation to the Coulomb energy part, in second order perturbation theory, the virtual hopping of a spin up electron to a neighboring site that contains also an electron with spin up is forbidden by Pauli's exclusion principle. Since delocalization lowers the kinetic energy, the electrons of neighboring sites tend to have opposite spin.

This means for EuO: when one electron will go from one site to a neighboring site, in a half filled f shell with $S=7/2$, only an electron can be added to the neighboring site when it has opposite spin. The antiferromagnetic exchange interaction is equal to $\frac{2t^2}{U}$. Since t is small in EuO and U is big, this leads to a small antiferromagnetic exchange from the 4f orbitals. However, this exchange is negligible compared to the ferromagnetic exchange interaction described in paragraph 2.3.2.

2.2.3 Energy of $4f^7$ Excited State Configurations

The energy of a certain 4f electronic configuration can be calculated by [3]:

$$E(N_\uparrow, N_\downarrow) = F^0 \sum_{n=1}^{N_\uparrow + N_\downarrow - 1} n - J_H \left(\sum_{n_\uparrow=1}^{N_\uparrow - 1} n_\uparrow + \sum_{n_\downarrow=1}^{N_\downarrow - 1} n_\downarrow \right) \quad (2.11)$$

Where F^0 is a Coulomb repulsion therm and J_H is a Hund's rule exchange term. The Coulomb repulsion, F^0 , can be partly compensated by J_H when

electrons have parallel spins. The energy of some relevant 4f electronic configurations is:

$$E = 21F^0 - 21J_H \quad ^8S \quad \uparrow\uparrow\uparrow\uparrow\uparrow\uparrow \quad (2.12)$$

$$E = 15F^0 - 15J_H \quad ^7F \quad \uparrow\uparrow\uparrow\uparrow\uparrow \quad (2.13)$$

$$E = 28F^0 - 21J_H \quad ^7F \quad \uparrow\uparrow\uparrow\uparrow\uparrow\downarrow \quad (2.14)$$

$$E = 21F^0 - 15J_H \quad ^6S \quad \uparrow\uparrow\uparrow\uparrow\uparrow\downarrow \quad (2.15)$$

Taking $F^0=6.5\text{eV}$ and $J_H=0.9\text{ eV}$ [3], one can calculate the energy using equation 2.11, $U_{effective}$, that it cost to transfer one electron from one $4f^7$ europium ion to another: $U_{eff} = E_{4f^8} + E_{4f^6} - 2E_{4f^6} = F^0 + 6J_H = 11\text{ eV}$. However, the energy to flip one spin in the valence band is $6 J_H = 5.4\text{ eV}$.

2.2.4 $5d^1$ Excited State Configuration in a Crystal Field

In the previous paragraph, the energy of the 4f orbitals was described and now we turn to the discussion on the energy diagram of the 5d orbitals. In the lowest excited state, $[\text{Xe}]4f^65d^1$, the 5d orbitals contain one electron. For the 5d orbitals the crystal field is more important than for the 4f orbitals [3]:

4f electrons: exchange splitting > spin- orbit coupling > crystal field

5d electrons: crystal field > exchange splitting > spin- orbit coupling

Let us first discuss a possible d^1 ground state configuration in the presence of an octahedral crystal field (O_h point group symmetry). In the d^1 configuration $S=1/2$ and $L=2$ which gives a 2D term symbol. The characters for a $L=2$ system in the O_h point group are 5, 1, -1, 1, -1 for the E , C_2 , C_4 , $C_{2'}$ and C_3 symmetry elements respectively. Decomposed in irreducible representations of the O_h group, a $L=2$ system has e_g and t_{2g} irreducible components.

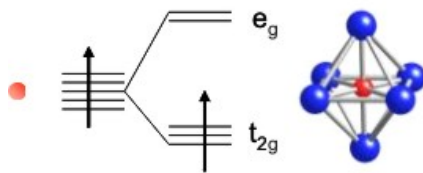


Figure 2.8: *Europium ion in an octahedral crystal field.*

As depicted in figure 2.8, without the presence of a crystal field, the five d-levels with $\Delta m_L = -2, -1, 0, 1, 2$ are degenerate. The degeneracy of the 5d orbitals is partially removed by the crystal field which split the levels in e_g and t_{2g} levels. This has important consequences for the orbital angular momentum. Without a crystal field, the wavefunctions ψ_{L,m_L} are complex functions, except for the $m_L = 0$ case. In the presence of the crystal field, two more real functions

have to be made out of linear combinations of the ψ_{L,m_L} functions [21] [22]. The t_{2g} functions will become:

$$t_{2g}^0 = \frac{1}{\sqrt{2}}(\psi_{d_2} - \psi_{d_{-2}}) \quad t_{2g}^1 = \psi_{d_1} \quad t_{2g}^{-1} = \psi_{d_{-1}} \quad (2.16)$$

The e_g functions look like:

$$e_g^a = \psi_{d_0} \quad e_g^b = \frac{1}{\sqrt{2}}(\psi_{d_2} + \psi_{d_{-2}}) \quad (2.17)$$

The e_g^a , e_g^b and the t_{2g}^0 functions have $m_L = 0$ while the t_{2g}^1 and t_{2g}^{-1} functions have $m_L = 1$ and $m_L = -1$ respectively. Let us now discuss the effect of spin-orbit coupling on the d^1 configuration. For 3d transition metals, the octahedral crystal field splitting is larger than the spin-orbit splitting and J is not a good quantum number anymore. However, for heavier atoms, the spin-orbit coupling is larger and sometimes it is not clear whether the crystal field splitting or the spin-orbit splitting dominates. We assume that in EuO the crystal field splitting is more important than the spin-orbit coupling [3] as can be seen in figure 2.9. First the 5d levels are split by the crystal field. Although the spin-orbit coupling does not split the e_g levels further, the t_{2g} levels are split. The representations are not one of the representation of the O_h group anymore ($A_{1g} (= \Gamma_1)$, $A_{2g} (= \Gamma_2)$, $E_g (= \Gamma_3)$, $T_{1g} (= \Gamma_4)$ and $T_{2g} (= \Gamma_5)$) but are representations of the double group O' ($\Gamma_{1..8}$). This is because S is non integral. This will make J a half integer which will have a double valued representation [22].

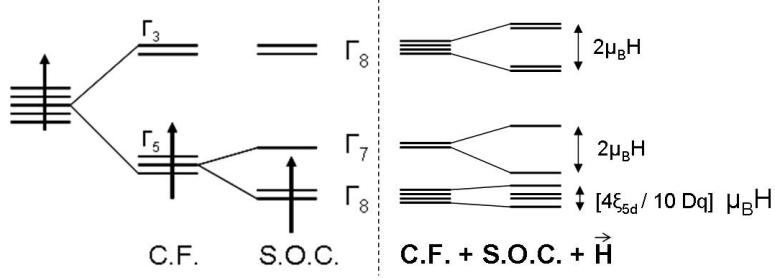


Figure 2.9: Influence of the crystal field and spin orbit coupling on the 5d levels. The levels are split by first by the crystal field, and then by the spin-orbit coupling $3/2 \xi_{5d}$. In the most right picture, the levels are split in an applied magnetic field H .

The wave functions $\Gamma_8(^2E_g)$, $\Gamma_8(^2T_{2g})$ and $\Gamma_7(^2T_{2g})$ including spin are [22] listed in order to determine the contribution of (excited) d-electrons to the total magnetization, as described in paragraph 2.3.7.

$$\Gamma_8^a(^2E_g) = e_g^b \beta \quad (2.18)$$

$$\Gamma_8^b(^2E_g) = -e_g^b \alpha \quad (2.19)$$

$$\Gamma_8^c(^2E_g) = e_g^a \beta \quad (2.20)$$

$$\Gamma_8^d(^2E_g) = -e_g^a \alpha \quad (2.21)$$

$$\Gamma_8^a(^2T_{2g}) = \frac{1}{\sqrt{3}}(-\sqrt{2}t_{2g}^0\beta + t_{2g}^1\alpha) \quad (2.22)$$

$$\Gamma_8^b(^2T_{2g}) = \frac{1}{\sqrt{3}}(-\sqrt{2}t_{2g}^0\alpha - t_{2g}^1\beta) \quad (2.23)$$

$$\Gamma_8^c(^2T_{2g}) = t_{2g}^{-1}\alpha \quad (2.24)$$

$$\Gamma_8^d(^2T_{2g}) = -t_{2g}^1\beta \quad (2.25)$$

$$\Gamma_7^a(^2T_{2g}) = \frac{1}{\sqrt{3}}(\sqrt{2}t_{2g}^0\beta + \sqrt{2}t_{2g}^1\alpha) \quad (2.26)$$

$$\Gamma_7^b(^2T_{2g}) = \frac{1}{\sqrt{3}}(-\sqrt{2}t_{2g}^0\alpha + \sqrt{2}t_{2g}^{-1}\beta) \quad (2.27)$$

α and β are (S, M_S) (1/2, 1/2) and (1/2, -1/2) respectively. When a magnetic field is applied, the levels can split further as is depicted in figure 2.9. In terms of the Zeeman effect, the $\Gamma_7(^2T_{2g})$ and $\Gamma_8(^2E_g)$ levels are split by $g\mu_B \vec{H}$ where g is the spectroscopic splitting factor and \vec{H} is the applied magnetic field. For both levels the g-factors equals two. The g-factor of the $\Gamma_8(^2T_{2g})$ levels is zero using non-perturbed functions. However, spin-orbit coupling leads to interaction between $\Gamma_8(^2T_{2g})$ and $\Gamma_8(^2E_g)$ levels which have the same symmetry. In first order approximation, the new wave function becomes:

$$\psi(\Gamma_8^n) = \Gamma_8^n(T_{2g}) - \sqrt{\frac{3}{2}} \frac{\xi_{5d}}{10Dq} \Gamma_8^n(E_g) \quad (2.28)$$

In which Dq is the crystal field splitting and ξ_{5d} is the spin orbit coupling constant. The g-factor for the $\psi(\Gamma_8^a)$ and $\psi(\Gamma_8^d)$ levels becomes now $\frac{4\xi_{5d}}{10Dq}$. Using the atomic value $\xi_{5d} = 67$ meV [3] and the experimental value for the crystal field $Dq = 2$ eV, the g-factor becomes 0.013. The $\psi(\Gamma_8^b)$ and $\psi(\Gamma_8^c)$ functions have $m_J = 1/2$ and $m_J = -1/2$, respectively and are not split by the magnetic field, but the $\psi(\Gamma_8^a)$ and $\psi(\Gamma_8^d)$ levels are split by 0.013 $\mu_B \vec{H}$.

2.3 Exchange Interactions

2.3.1 $5d^1$ Configuration and Superexchange Interactions

In EuO, the 5d orbitals are hybridized with oxygen 2p electrons that impose on the 5d orbitals some 2p character. This hybridization can change the picture of the $5d^1$ state in a crystal field. Interaction with oxygen orbitals may also lead to cation-anion-cation exchange interactions. Let us now describe the concept of superexchange interaction which will be used to explain the ferromagnetism of EuO in the next section. Generally, superexchange interaction can lead to ferromagnetism as well as antiferromagnetism. Two important factors in this are the bond angle and the type of the orbital: $p\sigma$ or $p\pi$. In the $5d^1$ (excited) state there can occur both 180° as well as 90° superexchange interactions. With the help of the sketches in figure 2.10, two of the possible contributions to superexchange will be discussed, namely the correlation effect and delocalization. The correlation mechanism takes into account the simultaneous partial bond formation on each side of the anion. In the delocalization mechanism, the electron is assumed to move from one cation to another. Let us first discuss the 180° correlation effect. In the case that there is only one electron in a t_{2g} level, this gives a very weak antiferromagnetic coupling, both for $p\sigma$ and $p\pi$ orbitals, because this is the only way that two bonds can be formed simultaneously [21]. Delocalization will lead to a ferromagnetic interaction because of Hund's first rule. For a d^1 configuration the 180° superexchange is negligible small [21].

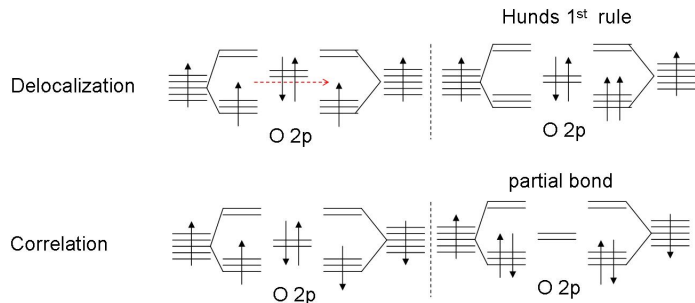


Figure 2.10: Two different superexchange mechanisms: delocalization and correlation.

Let us now turn to the 90° superexchange. The 90° delocalization exchange will be dominated by direct cation- cation exchange where no anion is involved. There are three possible correlation exchange processes in which electrons from different anion orbitals are involved. 1) Two s-electrons 2) Two electrons from the same p-orbital. Because of the geometry, this p-orbital will be a σ for one cation and a π one for another cation. 3) Electrons can come from two different p-orbitals. The signs for the delocalization 90° direct cation-cation exchange and the correlation 90° superexchange according to Goodenough [21] are anti-ferromagnetic and ferromagnetic, respectively. The superexchange mechanisms described for (excited) 5d electrons are similar to the exchange interactions responsible for ferromagnetism EuO, as will be described in the next paragraph.

2.3.2 Exchange Interactions in EuO

Till thus far the 4f orbitals were examined without the presence of the 5d orbitals and the other way around. In this paragraph we will take into account the interaction between the 4f and 5d orbitals. Finally, we will try to answer the main question: "Why EuO is ferromagnetic?". The proposed mechanisms includes both the d and f orbitals. Two different types of exchange interactions can be considered [3], [24]: 1) The indirect exchange between the nearest neighbor Eu cations, no oxygen anions are involved. 2) Superexchange.

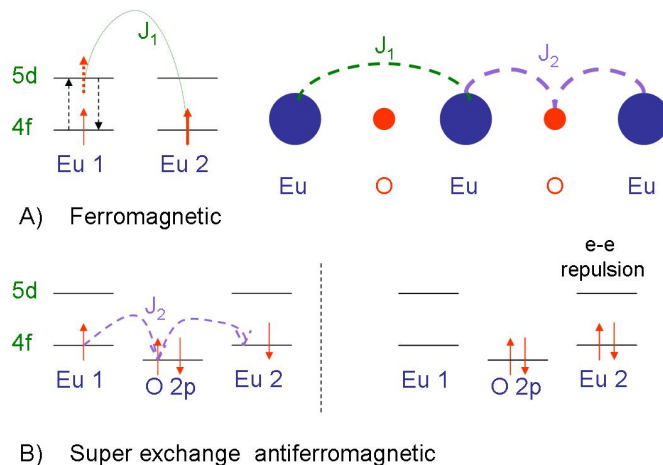


Figure 2.11: *Two types of exchange interactions that are important in EuO. A) Indirect exchange B) superexchange . Figure A) is the first type of exchange interaction described in the text. Figure B) is the a superexchange mechanism described in this paragraph. In the right picture one electron from the left europium ion has been transferred to the right europium ion.*

In the first type a 4f-electron makes a virtual transition to the 5d band and experiences an exchange interaction with the 4f spin on the nearest neighbor and returns to the ground state. This virtual excitation is shown in figure 2.11A. The interaction of the virtual excited 5d-electron with nearest neighbor 4f-electrons is ferromagnetic. One can compare this indirect exchange with the discussed delocalization superexchange mechanism. The difference is the that the delocalization is not via the p orbital of oxygen but via the 5d orbital (conduction band). The strength of this exchange is $J/(k_B) = 0.606 \pm 0.008 K$ [6].

In turn, there are three important superexchange interactions in EuO. In the first, a f-electron is transferred via an oxygen atom to an f-orbital on a neighboring site. This is shown in figure 2.11B: one electron from the left europium ion is transferred to the right europium ion. This can only happen when the spins are antiparallel and leads to antiferromagnetism. This delocalization effect is small because the transfer integral is small, and the Hubbard U is large. The second mechanism takes into account the d-orbitals. An oxygen p-electron

is transferred to a d-orbital of a neighboring europium ion and the other p-electron with opposite spin is transferred to the europium atom at the other site, see figure 2.12A. In turn, these electrons interact with the 4f electrons. This superexchange mechanism is also antiferromagnetic.

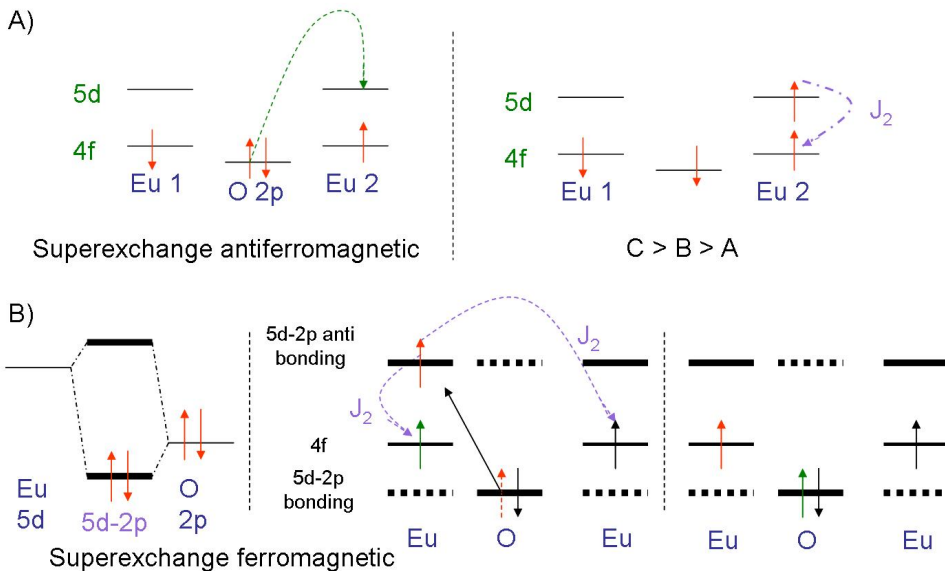


Figure 2.12: Two types of superexchange interactions: in A) an electron from the oxygen ion is transferred to the 5d band of a neighboring europium ion and experiences a ferromagnetic exchange. In B) the oxygen 2p-europium 5d band hybridization is included. The exchange mechanism is described in the text.

The last proposed exchange mechanism will lead to a ferromagnetic exchange interaction. Hybridization of the europium 5d and the oxygen 2p orbitals makes bonding orbitals with mainly 2p character and anti-bonding orbitals with mainly 5d character. This is shown in figure 2.12B. One electron can make a transition between the bonding and the anti-bonding molecular orbital. The excited electron can have an exchange interaction with two neighboring europium ions. This direct exchange is ferromagnetic. Now an 4f-electron can fill the hole in the bonding molecular orbital, after which the electron in the anti-bonding molecular orbital (5d character) fills the 4f hole. The last described superexchange mechanism is the most important and makes the net contribution due to superexchange ferromagnetic: $J_{superexchange}/k_B = 0.119 \pm 0.015 K$. To conclude, EuO is ferromagnetic because the ferromagnetic sign from the indirect exchange as well as from the superexchange mechanisms. When the values for the exchange constant are put in the mean field model, an ordering temperature of 46 K is obtained, which is lower than the observed ordering temperature of 69 K. The mean field model can not account for the ordering temperature of 69 K.

2.3.3 Exchange Interactions in the Eu Chalcogenides

Apart from EuO, also other europium chalcogenides are studied [10]. Whereas EuO is ferromagnetic with a ordering temperature of 69.3 K, EuS is ferromagnetic with $T_c = 16.6$ K and EuTe is antiferromagnetic with $T_N = 9.58$ K. EuSe is more complex: it is antiferromagnetic between 4.6 K and 2.8 K, ferrimagnetic in the range of $1.8 < T < 2.8$ K and antiferromagnetic again below 1.8 K. All the europium chalcogenides have a rocksalt structure. The magnetic properties of the europium chalcogenides can be understood from the competition between the indirect exchange and different superexchange mechanisms. Whereas in EuO the indirect exchange described in paragraph 2.3.2 dominates, when the ligand radius increases, the indirect exchange decreases and can compete with the superexchange.

The positive sign of the superexchange in EuO is explained by the described hybridization mechanism. For the other chalcogenides the net sign from superexchange processes is antiferromagnetic because of the antiferromagnetic exchange from the mechanism in which two electrons are transferred to two different Eu ions. The complex behavior in EuSe arises from competition between the positive indirect exchange and the negative superexchange processes.

2.3.4 Pressure Effects

In EuO the ferromagnetic ordering temperature at 1 bar can be enhanced to a maximum of 180 K at 250 kbar [31]. At 250 kbar EuO still has a rocksalt structure but the unit cell volume is now 85 percent of the volume at 1 bar [32]. With increasing pressure the optical gap decreases and approaches zero above 140 kbar [3]. Mössbauer experiments show that the valence of europium changes from 2.00 to 2.07 at 200 kbar [32].

Pressure can effect the exchange interaction in different ways. Firstly, the distance between the ions can decrease, leading to a stronger exchange interaction. Secondly, the EuO electronic bandgap decreases with increasing pressure and carriers in the conduction band can enhance the exchange interaction.

2.3.5 EuO in the Ferromagnetic Kondo Lattice Model

The magnetic properties of EuO will be discussed in terms of the ferromagnetic Kondo lattice model. The ferromagnetism of stoichiometric EuO in this model comes mainly from a Heisenberg term which includes the exchange from the processes described in section 2.3.2. However in excited EuO or doped EuO there is also the influence of the conduction electrons which can be taken into account in the ferromagnetic Kondo lattice model. As an introduction I will start by describing the normal Kondo model which describes the behavior of a magnetic impurity inside a metal. In a very dilute alloy in a non-magnetic host, the magnetic moments of the impurity ions can be considered as independent. They can only interact with the conduction electrons. At low temperatures a conduction electron can scatter from the magnetic impurity thereby flipping its own spin. The existence of this scattering channel results in an increase of the resistivity at low temperatures despite the fact that there are less phonons from which the electron can scatter. This increase of the resistivity at low temperature is called the Kondo effect. At low temperatures a cloud of conduction elections

with opposite spin relative to the localized magnetic moment screen the magnetic charge. The exchange interaction between the conduction electrons and localized magnetic moments is antiferromagnetic [20]. The interaction between d orbital conduction electrons and f orbital localized spins can be described by the following Hamiltonian:

$$H_{df} = -J \sum_i \sigma_i S_i \quad (2.29)$$

in which J is the d-f exchange constant, S is the spin moment of the impurity and σ is the conduction band spin operator. The details of the Kondo physics depend on the Fermi energy, conduction band bandwidth, position of the impurity level with respect to the conduction band and will not be discussed (the reader is referred to [20]). In the Kondo-lattice model however, there are no magnetic impurities anymore but there is a magnetic lattice described by the following Hamiltonian:

$$H = \sum_{ij\sigma} T_{ij} c_{i,\sigma}^\dagger c_{j,\sigma} - J \sum_i \sigma_i S_i \quad (2.30)$$

in which the first term is similar to the Hubbard model and represents the motion of the d orbital conduction electrons. The second term represent the antiferromagnetic interaction between the d-orbital conduction electrons and the localized spins of the impurities. Whereas in the case where the impurities were far apart the Ruderman Kittel Kasuya Yoshida (RKKY) interaction can be neglected, this is not the true in this case [25]. The interaction of the electron gas with the magnetic impurity gives an exchange interaction with oscillating sign [20]:

$$H_{RKKY} \sim \frac{J_{df}^2}{\epsilon_F} \frac{\cos(2k_F r + \phi)}{r^3} \quad (2.31)$$

in which J is the exchange interaction between the impurities and the conduction electrons and ϕ is a certain phase. This formula can only be used when the interaction of the conduction band electrons with the impurity is small (small exchange constant J) and the Fermi energy is large, since it is a perturbation in $\frac{J}{\epsilon_F}$. Also a sharp cutoff of the Fermi- distribution at k_F is needed: a Fermi surface. The RKKY interaction can give rise to magnetic ordering with an orderings temperature proportional to $\frac{J^2}{\epsilon_F}$. However also screening of the magnetic moment can take place giving a non magnetic ground state. The Kondo effect will occur below the Kondo temperature (in the case of large f-f repulsion U, large conduction band bandwidth W, and deep lying f- level) [20] [26]:

$$T_K \sim \epsilon_F e^{-\frac{1}{J\rho(\epsilon_F)}} \quad (2.32)$$

in which $\rho(\epsilon_F)$ is the density of states at the Fermi level. In this case there is a competition between magnetic and non-magnetic ground states [26]. Now the interaction between the conduction electrons and the localized moments can be

made ferromagnetic in the ferromagnetic Kondo lattice model, sometimes called s-d or s-f model, in which EuO can be described [27]:

$$H = \sum_{ij\sigma} T_{ij} c_{i,\sigma}^\dagger c_{j,\sigma} - J \sum_i \sigma_i S_i \quad (2.33)$$

This is the same as the Kondo lattice model apart from the fact that J now is taken positive. An additional factor can be added to account for other types of exchange interaction such as superexchange [29]:

$$H = \sum_{ij\sigma} T_{ij} c_{i,\sigma}^\dagger c_{j,\sigma} - J \sum_i \sigma_i S_i - J \sum_i S_i S_i \quad (2.34)$$

When the conduction band and localized electron interaction is ferromagnetic, this model can be seen as quantum mechanical variant of the well known double exchange model in which conduction electrons pulls up all localized moments because of Hund's intra atomic exchange and can induce ferromagnetism [28]. In $\text{La}_{1-x}\text{Ca}_x\text{MnO}_3$ for instance, the compound is a metal below the ferromagnetic orderings temperature and properties like giant magneto resistance can be observed [19]. This is because the motion of the conduction electrons is hindered when the background is not ferromagnetic. By applying a magnetic field, the spins align, giving a ferromagnetic background in which the conduction electrons can move.

However, for EuO the interaction between the conduction electrons and the localized moments is not of the Hund's rule type because the valance band is 4f and the conduction band is 5d. It is due to a direct d-f exchange process but is also ferromagnetic. When one wants to discuss magnetism in (doped) EuO one can not explain that just starting from the RKKY interaction since the RKKY interaction is calculated as perturbation in $\frac{J}{\epsilon_F}$ and in EuO, J is large and ϵ_F is small ($n \approx 0$) [20]. Apart from that, EuO is a semiconductor and has no Fermi surface which is required for the described RKKY interaction [10], [30].

When J is small and ϵ_F is large, the results from the ferromagnetic Kondo lattice model, as calculated by Nolting in [29] (conduction bandwidth $W = 1$ eV, $S = 7/2$, no Heisenberg term), corresponds well to the previous RKKY interaction, however, for stronger coupling the oscillations become less clear. This group also calculated the temperature dependent band structure of stoichiometric EuO [29]. The spin splitting of EuO calculated within the LSDA approach gives an energy splitting of 0.875 eV. The band structure reveals that EuO is an indirect band gap semiconductor from the X point to the Γ point [9]. Close to this gap there is a direct gap at the X point. However, the band gap from this calculations is about 3 eV, different from the absorption edge which is 1.2 eV. The obtained spin splitting is equivalent to JS , giving a d-f exchange constant of 0.25 eV. Now this value can be used in the multiband (two conduction bands) ferromagnetic Kondo lattice (FKL) model as was done by Nolting *et al.* [29]. For the exchange constants in the Heisenberg term $\sum -J_{ij} S_i S_j$, experimental values are taken: $J_1/k_B = 0.625K$ and $J_2/k_B = 0.125K$ for nearest neighbor (Eu-Eu) and next nearest neighbor (Eu-O-Eu), respectively. The FKL calculations were used to model the red shift of the conduction band below the orderings temperature. The obtained result is 0.35 eV, which is a bit higher

than half of the experimental value of the spin splitting, 0.3 eV [3]. The ferromagnetism in this calculations comes from the Heisenberg term (superexchange and indirect exchange) and not from the J_{df} term in the Hamiltonian. This can be seen from the calculations from Nolting where there is no Heisenberg term included [29]. According to this calculation with $J_{df} = 0.25$ eV and n=0, which is the case for EuO, the system will of course not order since there are no conduction electrons at 0 K. In order to get the temperature dependent band structure one electron was put in an otherwise empty conduction band.

Although the conduction band is empty at T=0, at elevated temperatures or after an optical excitation there are electrons in the conduction band. In this case, according to the model, the total exchange interaction can be enhanced because of the conduction band electrons. There can be also carriers introduced by doping EuO with for instance Gd. Experiments show that in this case the Curie temperature can be enhanced [2] indicating that indeed the exchange interaction can be enhanced. The FKL model can be used to explain the enhanced Curie temperature of Gd doped EuO, however ,to explain the ferromagnetism in stoichiometric EuO, the indirect and superexchange mechanism described in the previous paragraphs have to be invoked.

2.3.6 $5d^1$ Excited State in the Degenerate Hubbard Model

Whereas in the FKL model no interaction between the conduction electrons was incorporated, some interaction between them can be described in the degenerate Hubbard model. In a system with a degenerate d^1 ground state a ferromagnetic interaction between spins can be expected from the degenerate Hubbard model, which includes an additional term $J_H \sum_i \vec{S}_{i1} \vec{S}_{i2}$ with respect to the normal Hubbard model [19]:

$$H = t \sum_{\langle ij \rangle, \alpha\beta\sigma} c_{i,\alpha\sigma}^\dagger c_{j,\beta\sigma} + U \sum_{i,\alpha\beta\sigma\sigma'} n_{i\alpha\sigma} n_{i\beta\sigma'} + J_H \sum_i \vec{S}_{i1} \vec{S}_{i2} \quad (2.35)$$

where the J_H term is Hund's first rule intra atomic exchange, different from the Hubbard U which describes the intra atomic Coulomb repulsion. The one and two on spin S stand for different degenerate orbitals and the α and β for different degenerate levels. When the electrons on different sites are alternatingly in different degenerate orbitals, but have parallel spin, the energy due to the Hund's first rule intra atomic exchange is minimized. This is shown in figure 2.13. In figure A) hopping is not possible because of the Pauli exclusion principle. In B,C,D) when an electron hops from one site to another already occupied site, the energy of the site that becomes double occupied is minimized when the spins are parallel because of Hund's rule. This all leads to ferromagnetism in this model. This model was introduced to show that interactions between 5d electrons might also be important. From this model the d electrons are expected to have parallel spins.

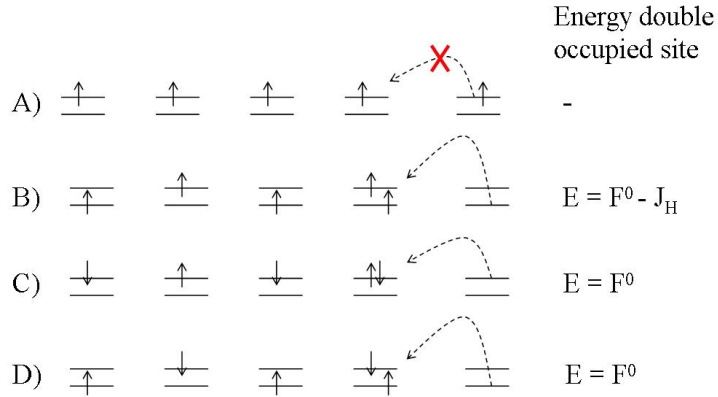


Figure 2.13: *Various configurations in the degenerate Hubbard model. A) no hopping is possible because of Pauli's exclusion principle. B) hopping is possible and energy is minimized according to Hund's rule. C,D) hopping is possible but the energy is higher than in B).*

2.3.7 Magnetism in the $4f^65d^1$ Excited State

The lowest excited states in EuO have a [Xe] $4f^65d^1$ configuration. This configuration gives rise to many terms. However not every $4f^7$ to $4f^65d^1$ transition can be made optically because of selection rules. In the first place the intrinsic angular momentum of a photon can interact only with the orbital angular momentum of an electron. Since the spin is not affected, the difference in total spin angular momentum must be zero: $\Delta S = 0$. The selection rule for the total angular momentum is $\Delta L = 0, \pm 1$. However, because $\Delta L = 0$ transitions are parity forbidden in this case since $L=0$, only $\Delta L = +1$ ($\Delta L = +1$, since the ground state is $L=0$) transition are allowed [3]. This will give a 8P excited state. Depending on the polarization of the light, Δm_L will be 0, plus 1 or -1 for linear polarized light, right circular polarized light and left polarized light respectively.

In the presence of spin-orbit coupling, the total angular momentum J will be $5/2$, $7/2$, or $9/2$ giving ${}^8P_{5/2}$, ${}^8P_{7/2}$ and ${}^8P_{9/2}$ terms, respectively. When there is spin-orbit coupling, the spin angular momentum and the orbital angular momentum are not good quantum numbers anymore but the total angular momentum J is. Depending on the strength of the spin-orbit coupling, L and S are more or less meaningless. The selection rules for strong spin-orbit coupling are $\Delta J = 0, \pm 1$, $\Delta m_J = 0, \pm 1$ and the selection rules for weak spin-orbit coupling are: $\Delta J = 0, \pm 1$, $\Delta m_J = 0, \pm 1$, $\Delta L = 0, \pm 1$. In the latter case the selection rule for the total spin angular momentum $\Delta S = 0$ not rigorous anymore. A photon can transfer angular momentum to the orbital angular momentum of an electron and because of the spin-orbit interaction, the spin can be flipped.

Thus, after an optical excitation with a photon energy of 1.55 eV, the system will end in a $4f^65d^1$ configuration with $L = 1$, $S = 7/2$ and $J = 9/2, 7/2, 5/2$. No oxygen 2p to Eu 5d transition can be made with a photon energy of 1.55 eV, as was used in our experiments. However, S can also become $5/2$ because of the spin-orbit coupling. Spin-orbit coupling can mix states with the same J that differ by $\Delta S = 1$ and can give the J final states some $S = 5/2$ character. In

an atomic picture, the $J = 9/2, 7/2, 5/2$ states have an effective number of Bohr magnetons of 8.84, 7, 69 and 6.76, respectively and a g-factor of 1.78, 1.94 and 2.29, respectively. From this analysis, right after excitation the total magnetic moment could increase or decrease depending on which J state is excited.

When after an optical excitation from the valance band to the conduction band, the holes can relax within the valence band and the electrons within conduction band, one can consider a 'ground sate' of the $4f^65d^1$ configuration. The used coupling scheme for obtaining J will be as followings: first the 4f angular momenta couple to L_{4f^6} and S_{4f^6} and finally to J_{4f^6} which is the ground state configuration of a valence band hole. $J_{4f^6} = L_{4f^6} - S_{4f^6} = 3 - 3 = 0$, $J_{5d^1} = L_{5d^1} + S_{5d^1} = 1 + 1/2 = 3/2$, see for a detailed discussion the analysis of the d^1 state in an octahedral crystal field as described in paragraph 2.2.3. The g- factor of this state is 0.013. From this analysis, the effective magnetic moment is expected to (almost) vanish. The most important conclusion is that an optical excitation of EuO can affect the magnetization and that this can come from changes in exchange constant but also from changes in the total (atomic) magnetic moment. According to this analysis the total moment will decrease.

2.4 Eu-rich EuO and Gd-doped EuO

In this paragraph, Eu-rich EuO and Gd-doped EuO is treated. Both compounds show a MIT at the ordering temperature, have CMR effects can have an enhanced ordering temperature when the conduction band is populated. One way to introduce additional carriers in the conduction band is to make Eu-rich EuO in which oxygen vacancies are generated. Konno and co-workers [17] have shown that in this way the ordering temperature can be increased to 150 K which can be explained by an enhancement of the exchange interaction by the conduction electrons. For lower vacancy concentrations the ordering temperature is still around 69 K. Another way to introduce carriers in the conduction band is to chemically dope it with Gd. Gd³⁺ is 4f⁷ and doping can add one electron to the conduction band. Recently a T_c of 170 K was achieved in 4 % Gd-doped EuO films [2]. Ott *et al.* [2] also showed that the Gd spins couple ferromagnetically with the Eu spins. So this compound is a model system for what can happen when the conduction band is filled. At low doping concentrations, < 1.3%, the additional electrons are localized on the Gd-ions by a ferromagnetic exchange interaction in a so-called Bound Magnetic Polaron (BMP). At higher concentration the carriers become delocalized. Now these (conduction) electrons can increase the exchange interaction giving use to an enhanced ordering temperature. The same BMP model can be used to describe the transport properties of Eu-rich EuO: two electrons are bound to the vacancy by the Coulomb interaction. The electrons can increase the ferromagnetic coupling of the surrounding Eu moments via indirect exchange. As a result, the increased magnetization will enhance the binding energy of the electron to the vacancy. The electron will be mainly bound due to the exchange interaction. However sometimes also the so-called He model is described where two electrons form a singlet and are bound to the positive vacancy (2+) by the Coulomb attraction. The increased ordering temperature in Eu-rich EuO can be explained in the same way. At a high non-stoichiometry, the electrons are not bound anymore and can increase the exchange interaction.

Eu-rich EuO and Gd-doped EuO have a MIT around the ordering temperature [3]. This can be understood from the Bound Magnetic Polaron model (BMP) as well [11]. The MIT is explained by Steeneken *et al.* by the shift of the conduction band upon magnetic ordering. The conduction band then crosses a vacancy level and the electrons can delocalize in the conduction band. The resistivity of Eu-rich EuO can decrease more than six orders of magnitude around T_c [13] when a magnetic field is applied. Steeneken *et al.* proposed for the CMR a similar model as for the MIT: a magnetic field aligns the 4f spins and by a d-f exchange interaction, this induces a shift of the conduction band such that it crosses the occupied states. In this way it does not matter for the MIT if it is the applied magnetic field that aligns the magnetic moments or that the moments aligns because T_c is crossed. Part of the decrease in resistivity can be also explained because of the decrease in magnetic scattering as described before [10].

Now let us come back to the MIT in the photoconductivity in stoichiometric EuO. When EuO is illuminated, a MIT can be observed which is also sensitive to the applied magnetic field around the ordering temperature. There is a negative magnetoresistance in the photoconductivity. If one assumes that magnetic excitons are formed, a MIT can occur because the exciton dissociates upon magnetic ordering. In this way the MIT occurs because of a change in the amount of free carriers and not only because of a change in the mobility, as suggested by Steeneken. However, mobility measurements of photocarriers reveal that the mobility changes from $90 \text{ cm}^2\text{V}^{-1}\text{s}^{-1}$ at 60 K to $250 \text{ cm}^2\text{V}^{-1}\text{s}^{-1}$ at 20 K indicating that also changes in mobility are important. There seems to be some similarity between the MIT and GMR in Eu-rich EuO and the MIT and the magneto-resistance seen in the photoconductivity measurements on stoichiometric EuO.

2.5 Conclusion: Exchange Interactions in EuO

In this section, after discussing a lot of different models, a summary will be given. Stoichiometric EuO is ferromagnetic because of the indirect exchange interaction in which a 4f electron makes a virtual excitation to the 5d band and has an exchange interaction with the nearest neighbor europium ion, and because of the described superexchange interaction in which the hybridized oxygen 2p and europium 5d bands are involved. The ferromagnetism can not be explained in the FKL model without Heisenberg exchange term since there are no conduction electrons. When there are conduction electrons, the exchange interaction can be enhanced as described in the FKL model. One can see this as follows: the exchange interaction does no longer involve virtual excitations from the 4f electrons to the 5d conduction band, but arises of the carriers in the conduction band. It is already known that chemical doping can enhance the ordering temperature because in this way carriers are introduced to the conduction band.

The FKL model neglects interaction between 5d electrons. As was shown in the degenerate Hubbard model, the existence of Coulomb interaction between the conduction electrons may favor a parallel spin orientation in the degenerate Hubbard model in order to minimize the Coulomb repulsion. The discussed antiferromagnetic exchange interaction from the Hubbard model is negligible

small.

2.6 Magneto Optical Kerr Effect

The title of this thesis is: "ultrafast carrier and magnetization dynamics in EuO". The final goal of the project is to study and control the magnetism and conductivity in EuO. One thing that was measured is the transient hysteresis: this is the change in magnetization after a short ($\sim 50\text{ fs}$) light pulse. Normal hysteresis loops are usually measured using Superconducting QUantum Interference Device (SQUID) magnetization measurement systems. However, to get access to the magnetization on a femto second time scale, a different approach will be used. By looking to the Magneto-Optical Kerr Effect (MOKE), which is proportional to the sample's magnetization, and using femtosecond laser pulses, the magnetization can be followed on short time scales. First a linear polarized intense pump pulse will excite the system. Then after a certain delay, which can be varied, a weaker linear polarized probe pulse will hit the sample on the same place. By catching the reflection of the probe pulse and looking at the rotation of polarization, the magnetization can be studied. First the Kerr effect will be described microscopically followed by the macroscopic picture.

2.6.1 Microscopic Mechanism

The Kerr effect occurs because the off diagonal elements in the dielectric tensor give a different absorption coefficient and refractive index for left and right circular polarized light. As shall be shown, spin-orbit coupling as well as exchange interactions are needed for a spontaneous Kerr effect (without applied magnetic field). This is done by discussing the electronic configuration of EuO. The ground state has an $L=0, S=7/2$ configuration. The electron can make transitions to states that have $L=1, S=7/2, 5/2$ configurations when also spin flip transition are considered. The electric dipole transition probability for the spin flip transitions will be zero when there is no spin-orbit coupling, as stretched out in figure 2.14. Without spin-orbit coupling but with exchange interaction, the $S=7/2$ and $S=5/2$ levels are split by the exchange interaction. This is shown in the second picture in figure 2.14, where the spin of the electron is shown that makes the transition. No spin flip transition can be made since there is no spin-orbit coupling. The transition probability for left and right circular is the same.

Now the spin-orbit interaction can be switched on. The levels with the same S and L but different m_L are now split. Because of this, the transition probabilities are different for left and right circular polarized light giving the Kerr effect. The Kerr effect in EuO however is mostly described in a slightly different way. As described before, the energy of the final state is mostly determined by the six 4f electrons, $J_{4f^6} = 0..6$. Now the following transition probability can be calculated: $R_{J_z,4f} \sim | \langle \psi_{5d_{t_{2g}}} | \epsilon \cdot \mathbf{r} | \psi_{4f,m_{L_{4f}}} \rangle |^2$. In which ϵ is the polarization operator and can be constructed from spherical harmonics. The polarization operators for linear, right circular and left circular polarized light are proportional to $Y_{1,0}, Y_{1,1}/\sqrt{2}$ and $Y_{1,-1}/\sqrt{2}$ respectively. In [3] for the t_{2g} orbitals, linear combinations of atomic wavefunctions were taken in order to make them real. Since the radial part for all transitions is the same, it is not

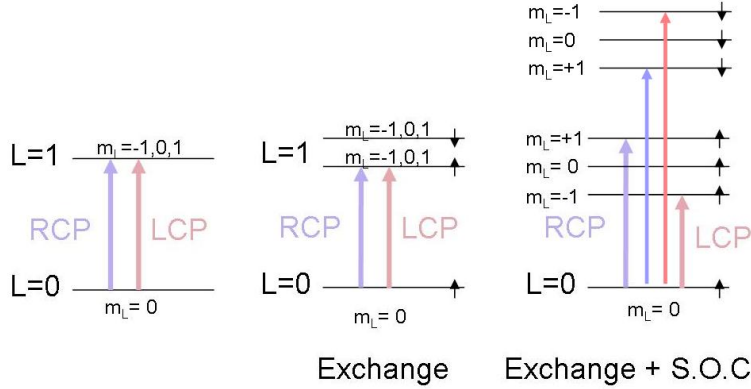


Figure 2.14: *Origin of the Kerr effect. Both S.O.C. and exchange interactions are needed. In the left picture there is no exchange nor S.O.C. In the middle picture, there is only exchange and in the right picture there is both exchange and S.O.C.*

important for explaining the Kerr effect. Now first $R_{J_z,4f}$ have to be calculated for right and left polarized light, see bottom left scheme in figure 2.15. $J_{z,4f}$ of the remaining six 4f electrons is: $J_{z,4f^6} = S_{z,4f^6} + L_{z,4f^6} = 3 - m_L$. Each of the $J_{z,4f}$ final state is a superposition of the different J states: $J_{z,4f} = 0$ is a superposition of $J = 0 \dots 6$ states, see the top scheme in figure 2.15. Now all the contributions have to be summed in order to get the transition probability $R_{J_{4f}}$ to a J final state as can be clearly seen in the top right scheme in figure 2.15:

$$R_{J_{4f}} \sim \sum_{|J_{z,4f}| \leq J_{4f}} \frac{R_{J_{z,4f}}}{7 - |J_{z,4f}|} \quad (2.36)$$

This was done by Steeneken [3] in order to calculate the difference in absorption between left and right circular polarized light, the magnetic circular dichroism spectrum. For the energy of the different J states, the values of the multiplet of Eu in another crystal, EuF₂, was used. The obtained MCD spectrum is similar to the experimentally obtained MCD spectrum indicating that it is a good approach to calculate this magneto-optical effect.

2.6.2 Macroscopic Description

As mentioned, the Kerr effect is the rotation of polarization of linear polarized light. Polarized light can be described by Jones vectors. For linear polarized light in a linear basis this gives:

$$E_x = \begin{pmatrix} 1 \\ 0 \end{pmatrix} \quad E_y = \begin{pmatrix} 0 \\ 1 \end{pmatrix} \quad (2.37)$$

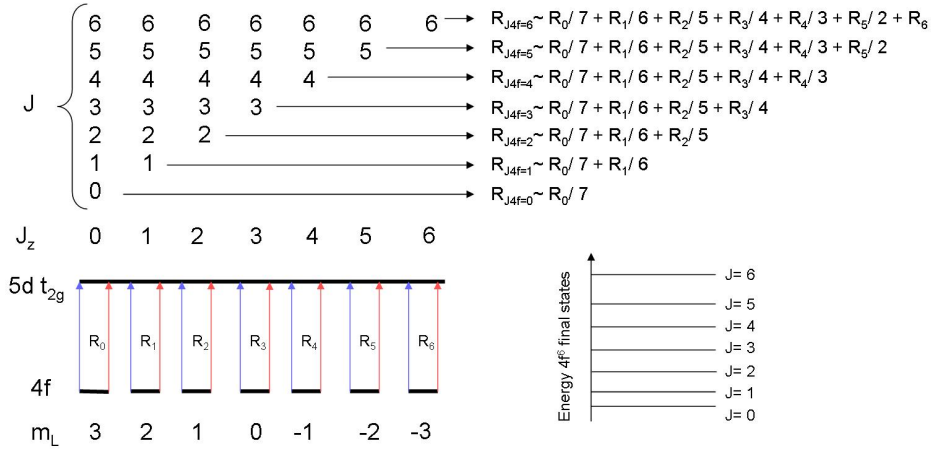


Figure 2.15: Calculations of a MCD spectrum. The blue and pink arrows represent a transition with left and right circular polarized light respectively.

The polarization of the light can be rotated counter clockwise by an angle θ using a rotation matrix. The rotation matrix is:

$$R(\theta) = \frac{1}{\sqrt{2}} \begin{pmatrix} \cos \theta & -\sin \theta \\ \sin \theta & \cos \theta \end{pmatrix} \quad (2.38)$$

Also right and left circular polarized light can be described in the Jones matrix formalism. In circular polarized light the x component is π out of phase with the y component. In the Jones vector this phase shift gives $e^{i\pi} = i$:

$$E_{LCP} = \frac{1}{\sqrt{2}} \begin{pmatrix} 1 \\ -i \end{pmatrix} \quad E_{RCP} = \frac{1}{\sqrt{2}} \begin{pmatrix} 1 \\ i \end{pmatrix} \quad (2.39)$$

Light can also be elliptically polarized. The ellipticity ϵ is defined as the ratio between the minor axis b and the major axis a of an ellipse: $\epsilon = b/a = \tan \beta$, in which β is the ellipticity angle. The Jones vector for elliptical light is:

$$E_{elliptical} = \begin{pmatrix} \cos \beta \\ i \sin \beta \end{pmatrix} \quad (2.40)$$

Sometimes it is more convenient to work in circular basis E_+ and E_- . The transformation matrixes are:

$$\mathbf{F}_{cart \rightarrow circ} = \frac{1}{\sqrt{2}} \begin{pmatrix} 1 & -i \\ 1 & i \end{pmatrix} \quad \mathbf{F}_{circ \rightarrow cart} = \frac{1}{\sqrt{2}} \begin{pmatrix} 1 & 1 \\ i & -i \end{pmatrix} \quad (2.41)$$

Also a polarization variable χ can be defined as the ratio of E_+ to E_- . Then in general, for rotated elliptical light:

$$\chi_{pol} = \frac{E_+}{E_-} = \frac{1 + \tan\beta}{1 - \tan\beta} e^{-2i\theta} = \frac{1 + \epsilon_k}{1 - \epsilon_k} e^{-2i\theta} \quad (2.42)$$

From which the rotation and ellipticity can be written as:

$$\theta = -\frac{1}{2} \arg \chi_{pol} \quad \epsilon_k = \frac{|\chi_{pol}| - 1}{|\chi_{pol}| + 1} \quad (2.43)$$

Now let us look to the reflection of light at normal incidence:

$$r(\omega) \equiv \rho(\omega) e^{i\Theta(\omega)} = \frac{\tilde{n} - 1}{\tilde{n} + 1} \quad (2.44)$$

in which \tilde{n} is the complex refractive index. The Kerr rotation is defined for the case of light at normal incidence and the magnetization parallel to the propagation direction of the light. Suppose that the complex refractive index is different for left and right polarized light. The polarization variable for the reflected light is:

$$\chi_{pol} = \frac{E_{out}^+}{E_{out}^-} = \frac{r^+}{r^-} \frac{E_{in}^+}{E_{in}^-} = \frac{r^+}{r^-} = \frac{\rho_+}{\rho_-} e^{i(\Theta_+ - \Theta_-)} \quad (2.45)$$

The Kerr rotation and ellipticity for light with normal incidence is:

$$\theta_K = -\frac{1}{2}(\Theta_+ - \Theta_-) \quad \epsilon_K = \frac{\rho_+ - \rho_-}{\rho_+ + \rho_-} \quad (2.46)$$

The Kerr effect occurs because the complex refractive index is different for right and left circular polarized light. A more general equation can be introduced by relating the equations for the Kerr effect to the dielectric tensor. The dielectric tensor for a cubic, non birefringent, crystal that does not have any Kerr effect, in cartesian coordinates, is:

$$\epsilon = \begin{pmatrix} \epsilon_{xx} & 0 & 0 \\ 0 & \epsilon_{xx} & 0 \\ 0 & 0 & \epsilon_{xx} \end{pmatrix} \quad (2.47)$$

However, for a cubic crystal that does have a Kerr effect [33] [34]:

$$\epsilon = \begin{pmatrix} \epsilon_{xx} & -i\varepsilon_{xx}Qm_z & i\varepsilon_{xx}Qm_y \\ i\varepsilon_{xx}Qm_z & \epsilon_{xx} & -i\varepsilon_{xx}Qm_x \\ -i\varepsilon_{xx}Qm_y & i\varepsilon_{xx}Qm_x & \epsilon_{xx} \end{pmatrix} \quad (2.48)$$

which can also be written as:

$$\epsilon = \epsilon_{xx} \begin{pmatrix} 1 & 0 & 0 \\ 0 & 1 & 0 \\ 0 & 0 & 1 \end{pmatrix} + \epsilon_{xx} \begin{pmatrix} 0 & -iQm_z & 0 \\ iQm_z & 0 & 0 \\ 0 & 0 & 0 \end{pmatrix}_{Polar} + \quad (2.49)$$

$$+ \epsilon_{xx} \begin{pmatrix} 0 & 0 & Qm_y \\ 0 & 0 & 0 \\ -iQm_y & 0 & 0 \end{pmatrix}_{Longitudinal} + \epsilon_{xx} \begin{pmatrix} 0 & 0 & 0 \\ 0 & 0 & -iQm_x \\ 0 & iQm_x & 0 \end{pmatrix}_{Transverse} \quad (2.50)$$

in which Q is the magneto-optical constant, $Q = i \frac{\epsilon_{xy}}{\epsilon_{xx} m_{x,y,z}}$; m_x, m_y and m_z define the direction of the magnetization relative to the k-vector of the light. In turn, the k-vector of the light defines the plane of incidence as illustrated in figure 2.16). When $m_x = m_y = 0$ and $m_z = 1$, the magnetization is in plane with the plane of incidence and parallel to the surface normal. This magneto optical effect is called the polar Kerr effect. When $m_x = m_z = 0$ and $m_y = 1$, the magnetization is in the plane of incidence and perpendicular to the surface normal. This is called the longitudinal Kerr effect. Finally when $m_y = m_z = 0$ and $m_x = 1$, the magnetization is perpendicular with the plane of incidence and perpendicular to the surface normal. This magneto optical effect is called the transverse Kerr effect.

In a compound without a Kerr effect, the reflection process can be described with a reflection matrix:

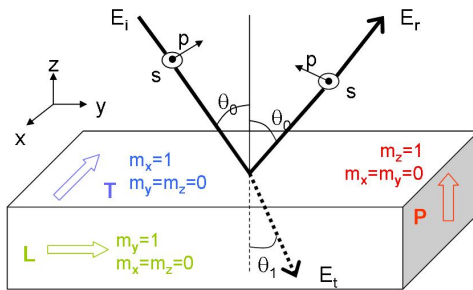


Figure 2.16: Different types of Kerr effect, P=polar Kerr effect, L=longitudinal Kerr effect, T=transverse Kerr effect.

$$\begin{pmatrix} E_p \\ E_s \end{pmatrix}_{Out} = \begin{pmatrix} r_p & 0 \\ 0 & r_s \end{pmatrix} \begin{pmatrix} E_p \\ E_s \end{pmatrix}_{In} \quad (2.51)$$

Where r_p and r_s are the reflection coefficients for p and s polarized light respectively, given by the Fresnel equations [35]:

$$r_s = \frac{\mu_1 \tilde{n}_0 \cos(\theta_0) - \mu_0 \tilde{n}_1 \cos(\theta_1)}{\mu_1 \tilde{n}_0 \cos(\theta_0) + \mu_0 \tilde{n}_1 \cos(\theta_1)} \quad r_p = \frac{\mu_0 \tilde{n}_1 \cos(\theta_0) - \mu_1 \tilde{n}_0 \cos(\theta_1)}{\mu_0 \tilde{n}_1 \cos(\theta_0) + \mu_1 \tilde{n}_0 \cos(\theta_1)} \quad (2.52)$$

However, for a Kerr medium, the reflection matrix becomes:

$$\begin{pmatrix} E_p \\ E_s \end{pmatrix}_{Out} = \begin{pmatrix} r_{pp} & r_{ps} \\ r_{sp} & r_{ss} \end{pmatrix} \begin{pmatrix} E_p \\ E_s \end{pmatrix}_{In} \quad (2.53)$$

The Fresnel equations become [36]:

$$r_{ss} = \frac{\mu_1 \tilde{n}_0 \cos(\theta_0) - \mu_0 \tilde{n}_1 \cos(\theta_1)}{\mu_1 \tilde{n}_0 \cos(\theta_0) + \mu_0 \tilde{n}_1 \cos(\theta_1)} \quad (2.54)$$

$$r_{pp} = \frac{\mu_0 \tilde{n}_1 \cos(\theta_0) - \mu_1 \tilde{n}_0 \cos(\theta_1)}{\mu_0 \tilde{n}_1 \cos(\theta_0) + \mu_1 \tilde{n}_0 \cos(\theta_1)} - \frac{i2\mu_0\mu_1\tilde{n}_0\tilde{n}_1\cos(\theta_0)\sin(\theta_1)m_xQ}{\mu_0\tilde{n}_1\cos(\theta_0) + \mu_1\tilde{n}_0\cos(\theta_1)} \quad (2.55)$$

$$r_{sp} = \frac{iQ\mu_0\mu_1\tilde{n}_0\tilde{n}_1\cos(\theta_0)[m_z\cos(\theta_1) + m_y\sin(\theta_1)]}{[\mu_1\tilde{n}_0\cos(\theta_0) + \mu_0\tilde{n}_1\cos(\theta_1)][\mu_0\tilde{n}_1\cos(\theta_0) + \mu_1\tilde{n}_0\cos(\theta_1)]\cos(\theta_1)} \quad (2.56)$$

$$r_{ps} = \frac{iQ\mu_0\mu_1\tilde{n}_0\tilde{n}_1\cos(\theta_0)[m_z\cos(\theta_1) - m_y\sin(\theta_1)]}{[\mu_1\tilde{n}_0\cos(\theta_0) + \mu_0\tilde{n}_1\cos(\theta_1)][\mu_0\tilde{n}_1\cos(\theta_0) + \mu_1\tilde{n}_0\cos(\theta_1)]\cos(\theta_1)} \quad (2.57)$$

in which $r_{ss} = r_s$, r_{pp} is equal to r_p plus an additional term for the transverse Kerr effect, and the only difference between r_{ps} and r_{sp} is a minus in the brackets of the nominator. The most important part of the equation is the $[m_z \cos(\theta_1) + m_y \sin(\theta_1)]$ term in which θ_1 is the angle of the refracted beam with the surface normal. In the polar case, r_{sp} is maximum when $\theta_1 = 0^\circ$ and is minimum when $\theta_1 = 90^\circ$. In the longitudinal Kerr effect it is the opposite, r_{sp} is minimum when $\theta_1 = 0^\circ$ is zero and is maximum when $\theta_1 = 90^\circ$. In the experiments p-polarized light is used. The magnitude of the r_{sp} matrix element, which determines the Kerr effect, is proportional to $\vec{k} \cdot \vec{M}$. \vec{k} is the k vector of the refracted beam and \vec{M} is the magnetization direction.

In the equations above, equation 2.55-2.57, the direction of the magnetization can be set by changing $m_{x,y,z}$. A change in the magnitude of the magnetization will result in a change in Q parameter. From the reflection matrix it can be seen that the polarization of the light can also be rotated by the diagonal components if the incoming light is not p or s polarized. However, this is because of the Kerr effect. The Kerr effect will now be defined for p or s polarized light:

$$\theta_k^s = Re(r_{ps}/r_{ss}) \quad \theta_k^p = Re(r_{sp}/r_{pp}) \quad (2.58)$$

The simplified formulas for the polar and longitudinal effect for $\mu = 1$ are [37]:

$$\theta_k^p = Re \left(\frac{\cos(\theta_0)(m_y \tan(\theta_1) + m_z)}{\cos(\theta_0 + \theta_1)} \frac{iQ\tilde{n}_0\tilde{n}_1}{(\tilde{n}_1^2 - \tilde{n}_0^2)} \right) \quad (2.59)$$

$$\theta_k^s = Re \left(\frac{\cos(\theta_0)(m_y \tan(\theta_1) - m_z)}{\cos(\theta_0 - \theta_1)} \frac{iQ\tilde{n}_0\tilde{n}_1}{(\tilde{n}_1^2 - \tilde{n}_0^2)} \right) \quad (2.60)$$

When the magnetic field is in plane of incidence but is not a pure longitudinal nor a pure polar Kerr effect $m_{y,z}$ is between 0 and 1:

$$m_y = M_y/M = -\sin \alpha \quad (2.61)$$

$$m_z = M_z/M = \cos \alpha \quad (2.62)$$

α is the angle of the magnetization with the surface normal (the angle is defined the same way as for the refracted beam). Since the diagonal components of the dielectric function in EuO are known [3], the complex refractive index can be determined. The only unknown in the formulas is the complex off diagonal component of the dielectric tensor. It is possible to determine this value when the Kerr rotation is measured at least two different angles of incidence.

2.7 TRMOKE Experiments in Literature

In this section some carrier dynamics and magnetization dynamics experiments are discussed, especially on Ni and Mn doped GaAs which is a diluted magnetic semiconductor. First the carrier dynamics in non-magnetic semiconductors will be discussed.

2.7.1 Carrier Dynamics in Semiconductors

When a short laser pulse hits a solid, more specifically a semiconductor, the energy of the excitation pulse is transferred first to electrons and then to the lattice. Various steps are illustrated in figure 2.17 [39] [40]:

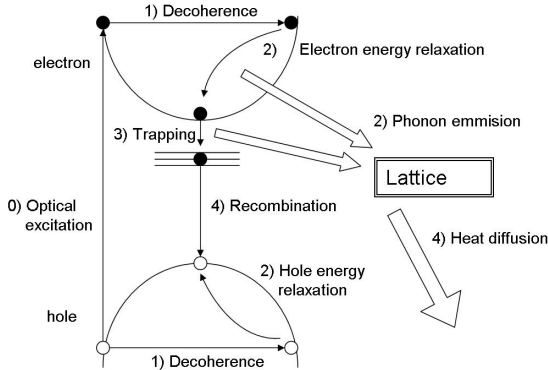


Figure 2.17: *Carrier dynamics in semiconductors.*

0) Carrier excitation. In the first step that can be identified, carriers are excited by a short laser pulse.

1) Decoherence. This is the loss of phase coherence between the laser pulse and the excited carriers. This will usually happen on a very short time scale (<100 fs) and is due to scattering from dislocations, impurities and surfaces.

2) Redistribution, thermalization and cooling. By electron-electron and electron-phonon scattering the free carriers will transfer to the bottom of the conduction band and approach a Fermi distribution. In the phonon emission processes, energy is transferred from the electron system to the lattice and the electrons can relax within the conduction band. The same mechanisms account for the relaxation of the holes in the valence band. An electron can emit a phonon with small k vector and remains in the same valley of the conduction band, this is called intravalley scattering, but can also emit phonons with large k vector and can transfer to a different valley, this is called intervalley scattering: an electron can scatter for instance from a Γ point to the X point in the conduction band. These phonons do not constitute an equilibrium thermal distribution, which preferentially populates the low energy acoustic modes. The phonons will thermalize resulting in an equilibrium distribution.

3) Trapping, recombination and carrier diffusion. On even longer timescales the electrons can recombine with the valence band holes, can be trapped, or even diffusion of electrons to another place in the sample with less conduction electrons can take place.

4) Recombination from trap levels and heat diffusion. The recombination from traps can be non-radiative and result in heating of the lattice. The sample will locally heat and the lattice cools down via heat transfer by phonons to the surrounding temperature bath.

Typical time scales for these processes in semiconductors are shown in figure 2.18 [40]. The characteristic timescales depend on the carrier density and consequently on the excitation strength. This is indicated in figure 2.18 by a gradient within the bar. The dark end indicates for processes at high carrier density (10^{22} cm^3) while the light end represents low density (10^{17} cm^3).

The interaction of electrons and the lattice in metals is sometimes described by a two temperature model in which the electron gas and the lattice have different temperatures and heat capacities, and interact with each other by an electron-phonon interaction [39]. In principle this model can not be applied to semiconductors since the holes and the electrons can have different temperatures. However, when one assumes that the hole and electron temperatures are the same, the two-temperature model is still applicable to semiconductors. Another big difference between the semiconductor and metal case is that the electronic heat capacity will be much smaller in intrinsic semiconductors.

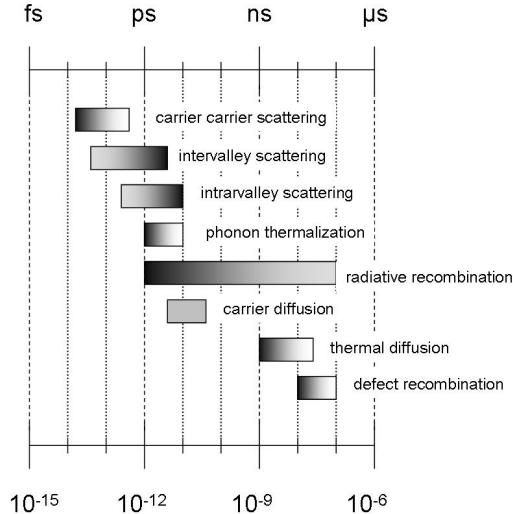


Figure 2.18: *Characteristic timescales for carrier and lattice dynamical processes in semiconductors.* Adapted from [40].

2.7.2 Magnetization Dynamics in Magnetic Semiconductors

In the final part of this theory chapter, we shall attempt to describe the magnetization dynamics in magnetic semiconductors with a similar general picture as the one illustrated before for carrier dynamics in semiconductors. This will be done by introducing different mechanisms, as described in the literature, on ferromagnetic metals like Ni, and Mn-doped GaAs and other materials. Since studying magnetization dynamics by TRMOKE is relatively new, a lot of things are still unclear. Let us start by identifying different steps in the magnetization dynamics:

0) As described before, the total angular momentum during excitation can change with a maximum of one. The electron can end up in the spin-up or spin-down sub-band of the conduction band when there is spin-orbit coupling. However, most electrons are expected to make the spin-up to spin-up transition. Depending on the polarization of the light, linear or right/left circular polarized, the electron can go the different m_L states.

There is a big discussion about the fast demagnetization rate ($\tau_M = 100\text{-}300$ fs) in Ni [41] [42]. Zang and Hübner [43] calculated that the simultaneous acting of spin-orbit coupling and laser field can be responsible for this since spin-orbit coupling mixes the singlet and triplet states. However, since a transition is governed by selection rules and conserves J partially, $\Delta J = 0, \pm 1$, this mechanism can only give a weak demagnetization or magnetization in EuO.

1) The phase coherence between the laser field and the conduction electrons can be lost because of momentum scattering. In a electron-impurity scattering

process the angular momentum of the electron is not conserved: the spatial part of the electronic wavefunction interacts during a scattering event giving a finite probability for a spin flip. This spin-flip mechanism was suggested as a source of fast demagnetization ($< 1\text{ps}$) in Mn doped GaAs [44] [45]. A flow of polarization from the Mn ions to the holes caused by a p-d spin flip scattering, followed by the demagnetization of the holes by the described spin-flip mechanism was proposed to account for the ultrafast demagnetization. The strength of this process depends on the momentum scattering rate, which is in the order of 10 fs in Mn doped GaAs, and the spin-orbit coupling strength. The described possible increase of exchange constant in the FKL model can also occur on very short timescales. Right after excitation, when the conduction band is populated, the exchange interaction can be enhanced because of the delocalized electrons.

2) In electron-electron, or hole-hole scattering processes, the total angular momentum J is conserved, whereas the effective g-factor can change on different places in the conduction band. See for a detailed discussion the paragraph about a $5d^1$ configuration in a octahedral crystal field where is described that different crystal field levels have different g-factors, paragraph 2.2.3. This can give magnetization as well as demagnetization. The electrons can also emit phonons and relax to the bottom of the conduction band. Both can happen for spin-up and spin-down electrons within the spin up and spin down conduction band but can also happen for holes in the valance band. In this phonon emission processes the total angular momentum is not conserved. The lower part of the valance band can correspond to different J states than the top of the valance band. The electrons and the holes will relax to the bottom of the conduction band and to the top of the valance band, respectively, and from the analysis of the $4f^65d^1$ excited state, this relaxation can lead to demagnetization because the hole will end up in a $J=0$ state.

However also spin flip processes can occur. The spin of a conduction electron can couple via spin-orbit coupling to the anisotropic fluctuations of the crystal field produced by phonons. In this way, electrons from the spin down band can go to the spin up part of the conduction band and vice versa [46].

3) By recombination and carrier diffusion carriers are removed from the system. This can affect the exchange constant when the exchange constant is dependent of the carrier concentration but it can also affect the magnitude of the angular momentum J and the g-factor: the system will end up in the $J=S=7/2$, $L=0$ ground state.

4) By heat diffusion the system can cool down and reach the ground state configuration again. Whereas the carrier in non-magnetic metals can be described in the two temperature model, ferromagnetic metals like Ni are sometimes described in the three temperature model in which the temperature of the lattice, the electrons and the spins are considered separately. When electrons are excited by a laser pulse, the electron temperature will increase. By phonon emission, energy is transferred to the lattice. Now by electron-spin interaction (for instance the Elliot-Yafet mechanism) and a spin-lattice interaction, the temperature of the spins can increase resulting in the demagnetization.

For EuO even additional temperature baths are needed for a complete description: both electrons and holes can have different temperatures, there is

the spin temperature of the electrons, the lattice temperature but also the spin temperature of the holes. In principle this hole spin temperature is not just a spin temperature but is the temperature of the 4f magnetic moments which can have both orbital and spin angular momentum. The interaction between the different baths can give a demagnetization on long timescales because of the overall heating after an optical excitation. However, it is also possible that the conduction electrons increase the exchange interaction, thereby effectively decreasing the temperature of the localized moments.

2.7.3 Conclusion

To summarize for EuO. After excitation the system can end up in another J state giving a induced magnetization or demagnetization. On short timescales the exchange interactions are expected to change, giving an increase in magnetization, but after the relaxation of electrons and holes in the conduction and valance band, respectively, the magnetization is expected to decrease. On longer timescales, the magnetization is expected to decrease as well because of the heating. In this section an overview was given in what kind of processes might be important in the transient magnetization measurements. In the next section the experimental results are shown.

Chapter 3

Hysteresis and Transient Hysteresis

3.1 Experimental Setup

A schematical picture of the used setup for the time-resolved magnetization and carrier dynamics measurements is shown in figure 3.1.

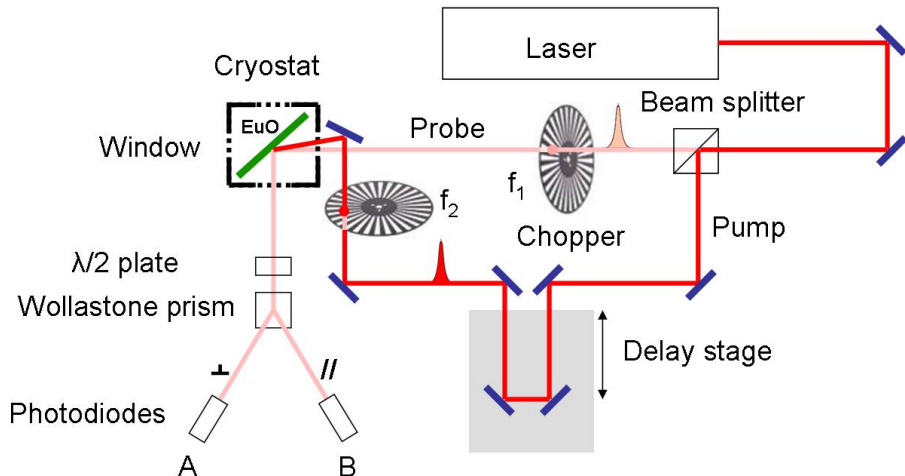


Figure 3.1: **TRMOKE and Transient Reflectivity setup.** The beam from the laser is split by a 75% / 25% beam splitter. The pump is chopped at f_2 and can be delayed. The probe is chopped as well, at f_1 . Both pump and probe are focussed using the same spherical mirror in such way that they overlap on the EuO sample in the cryostat. The probe reflection is catched and send to a half wave plate which can rotate the polarization of the light. The Wollaston prism splits the beam into a horizontal polarized component and a vertical polarized component. Finally both components are measured using two photodiodes coupled to two lock-in amplifiers. On one lock-in amplifier detector B was measured. On a second lock-in amplifier the difference signal was measured: detector A - detector B.

A mode-locked Ti:Saphire laser provides femtosecond laser pulses: linear polarized laser pulses with a duration of ~ 50 fs and a central wavelength of 800 nm. The repetition rate could be varied from 200 kHz to 80 MHz. The pump and probe beam in the cavity dumped setup were made using a 75% / 25% beam splitter and were chopped at frequency f_2 and f_1 respectively. Then the pump and probe pulses were focussed on the sample inside the cryostat using a spherical mirror. The cryostat at this setup includes a superconducting magnet, $0 \leq B \leq 8$ T. The beam diameter of the pump and probe in focus was $\sim 100 \mu\text{m}$. The reflection of the probe was caught and send to the detection system. This consists of a half wave plate, which can rotate the polarization of the light, and a Wollaston prism, which splits the beam in a horizontally polarized part and a vertical polarized part. The intensity of the two beams were measured using two balanced photodiodes coupled to a lock-in amplifier. On one lock- in amplifier detector B was measured. On a second lock-in amplifier the difference signal was measured: detector A - detector B. For the normal hysteresis measurements, in which only a probe pulse was used, the Kerr rotation can be calculated using the following equation.

$$I = \frac{I_H - I_V}{I_H + I_V} = \frac{I_0 \sin^2(45 + \theta) - I_0 \cos^2(45 + \theta)}{I_0 \sin^2(45 + \theta) + I_0 \cos^2(45 + \theta)} \quad (3.1)$$

H stands for horizontal, V stands for vertical. This equals $2\theta_K$ when θ is small. I_0 is the total intensity before the Wollaston prism. By a half wave plate the polarization of the light is rotated in such a way that without applied magnetic field and above the magnetic orderings temperature the difference between the intensity of the vertical photodiode and horizontal photodiode approaches zero. This can be done by rotating the light in such way that it reach the Wollaston prism at 45° . In the equation the difference between the detectors is divided by the sum of them in order to be insensitive to changes in the total reflectivity.

The pump and the probe beam were chopped at two different frequencies. The modulation of the pump and probe light can be expressed mathematically by a multiplication of the maximum intensity of the probe beam by $\Theta(\sin 2\pi f_2 t)$ and $\Theta(\sin 2\pi f_1 t)$, respectively where f_1 is the probe chopper frequency, f_2 is the pump chopper frequency and t is the time:

$$\Theta(x) = 0, x < 0 \quad 1, x \geq 0 \quad (3.2)$$

Since the used chopper frequency is around 1 kHz and the repetition rate of the laser is at least 800 kHz, several laser pulses can pass during the time that the chopper is open. When the modulation of the maximum of the pump and probe beam is expanded in Fourier series, the total intensity of the reflected probe light measured at the sum of the chopper frequency of the pump and the probe becomes [39]:

$$I_R(f_1 + f_2) = \frac{2}{\pi^2} \Delta R I_{probe}^A \quad (3.3)$$

in which ΔR is the difference in reflectance of the probe because of the acting of the pump pulse and I_{probe}^A is the maximum intensity of the probe pulse before

the reflection. The signal amplitude $I_R(f_1)$ of the probe without pump pulse at f_1 is:

$$I_R(f_1) = \frac{2}{\pi} R I_{probe}^A \quad (3.4)$$

From this, the transient reflectivity can be calculated:

$$\frac{\Delta R}{R} = \pi \frac{I_R(f_1 + f_2)}{I_R(f_1)} = \pi \frac{I_{R,H}(f_1 + f_2) + I_{R,V}(f_1 + f_2)}{I_R(f_1)} \quad (3.5)$$

The big advantage of this double modulation technique over the single modulation technique in which only the pump is chopped to determine the transient reflectivity, is that it is insensitive to scattered pump light. The same can be done for the measured difference of the horizontal and vertical component of the reflected probe beam at the sum frequency, in order to calculate changes in the Kerr rotation:

$$\Delta\theta_K = \frac{\pi}{2} \frac{I_{R,H}(f_1 + f_2) - I_{R,V}(f_1 + f_2)}{I_{R,total}(f_1)} \quad (3.6)$$

which holds only for small $\Delta\theta_K$, small ΔR and balanced photo detectors which means that the light arrives at 45° on the Wollaston prism. The transient reflectivity is a probe for the carrier dynamics whereas the transient Kerr rotation is a probe for the magnetization dynamics. They can be determined at the same time using the described setup.

3.2 Growth of EuO Films

Some of the experiments were done on an ‘old’ sample made a few years ago by P.G. Steeneken during his PhD in Groningen. In his PhD thesis the synthesis of the used sample is exactly described [3]. The other samples were made by myself and Ronny Sutarto at the University of Cologne in the group of Prof. L.H. Tjeng. The samples were only characterized by Kerr hysteresis measurements, checking if the magnetic orderings temperature was 69 K. They were made by a recipe of P.G. Steeneken as described in his PhD thesis and with the experience of Ronny Sutarto. In this section I will describe the growth conditions and give a description of the different samples.

3.2.1 Growth Conditions

The EuO films were grown by Molecular Beam Epitaxy (MBE) in a ultrahigh vacuum system with a base pressure of about $10^{-10} mbar$. High purity Eu metal was evaporated from an effusion cell. Molecular oxygen was added simultaneously through a leak valve. In order to prevent the formation of higher oxides Eu_2O_3 and Eu_3O_4 and Eu metal clusters, a recipe from Steeneken was used. The substrate temperature was kept higher than 350 °C and an excess of Eu was present on the substrate. In this way all the oxygen will react with Eu and no higher oxides will be formed. However, due to the high temperature of the

substrate, the excess of Eu on the substrate surface will re-evaporate into the vacuum and no Eu metal clusters will be formed. In one sample the substrate was kept at 300 °C in order to make Eu- rich EuO

For the old sample a 16 molar % yttrium stabilized ZrO₂ (YSZ) substrate was used in order to minimize the lattice mismatch between the substrate and EuO. In the new samples, double-side epi polished (100) MgO substrates were used. The lattice constant of MgO is 4.1 Å whereas the lattice constant of EuO is 5.1 Å, resulting in a lattice mismatch. Before starting the growth, the substrates were annealed for one hour in a 1×10^{-7} mbar oxygen atmosphere. Eu metal was sublimed at 515 °C giving a growth rate around 9 Å/ min as was checked with a quartz crystal thickness monitor. The oxygen partial pressure near the substrate during the growth was 5×10^{-8} mbar as monitored by a mass spectrometer. The samples were protected from oxidation by a Au/ Al or MgO capping layer. The gold was evaporated at 1150 °C giving a growth rate of about 0.8 Å/ min and after that the Al was evaporated at 900 °C giving a flux rate of about 2.4 Å/ min. The substrate was not heated. For the MgO capping the substrate temperature was 225°C and the Mg was sublimed at about 296 °C giving a flux rate of about 4.1 Å/ min. The oxygen atmosphere during the capping was about 2.7×10^{-7} mbar. On two samples 30 nm Cr contacts were sublimed. Cr was sublimed at 1300 °C as 3mm x 10 mm strips on the edge of the sample. On top of that EuO was grown followed by the capping layer.

3.2.2 Sample Characteristics

The sample characteristics are shown in the following table. The 'old sample' is sample number 1.

	Nr.	Thick-ness	Capping layer/ Thickness	Substrate Temperature	Details
1	GRON	20nm	MgO, 20nm	350 °C	Cr contacts
2	A031	25nm	Au/Al, 10/10nm	350 °C	half covered with EuO
3	A032	60nm	Au/Al, 10/10nm	350 °C	half covered with EuO
4	A033	25nm	MgO, 23nm	350 °C	half covered with EuO
5	A035	60nm	MgO, 23nm	350 °C	half covered with EuO
6	A036	60nm	MgO, 23nm	355 °C	30 nm Cr contacts
7	A037	60nm	MgO, 24nm	300 °C	30 Cr contacts, Eu- rich

Only half of the area (10 x 10 mm) of samples 2-5 was covered with EuO. The other half contains only the substrate and the capping layer. On the edge of sample 6 and 7, 30 nm Cr contacts were evaporated. On top of sample 6 and 7, 60 nm EuO was grown followed by 23 and 24 nm MgO respectively. The resistivity of sample 1 was measured by Steeneken. No MIT was observed indicating that stoichiometric EuO was grown.

3.3 Results

The samples 1, 3, 4, 5 and 6 were characterized by MOKE hysteresis experiments. Samples 2 and 7 were not characterized yet. The results are shown in this section. First the measurements are described and in the last paragraph, the results are discussed. The next section is about the transient hysteresis and transient reflectivity measurements.

3.3.1 Hysteresis Measurements

Sample 1

MOKE measurements for sample 1 at different temperatures are shown in figure 3.2. The angle of incidence was 45° . From this the coercivity, remanence and saturation magnetization can be determined as shown in figure 3.3. For this measurements 800 nm probe pulses were used. The magnetic field makes an angle of 45° degrees with the plane of the film as is shown in figure 3.3 either. The saturation Kerr rotation is 0.67 degrees at 12 K. At this temperature the remanence Kerr rotation is 0.55 degrees and the coercivity is 11 mT. The remanence Kerr rotation and coercivity disappears around 69 K, indicating that the orderings temperature of this sample is around 69 K. The same was done in the polar geometry in which the magnetic field is in plane of incidence and parallel to the surface normal. The result at 10 K is shown in figure 3.4. The Kerr rotation is small, 0.08 degrees at 100 mT, and no hysteresis was observed. Finally, for characterization, also a transmission spectrum was measured at room temperature as can be seen in figure 3.5.

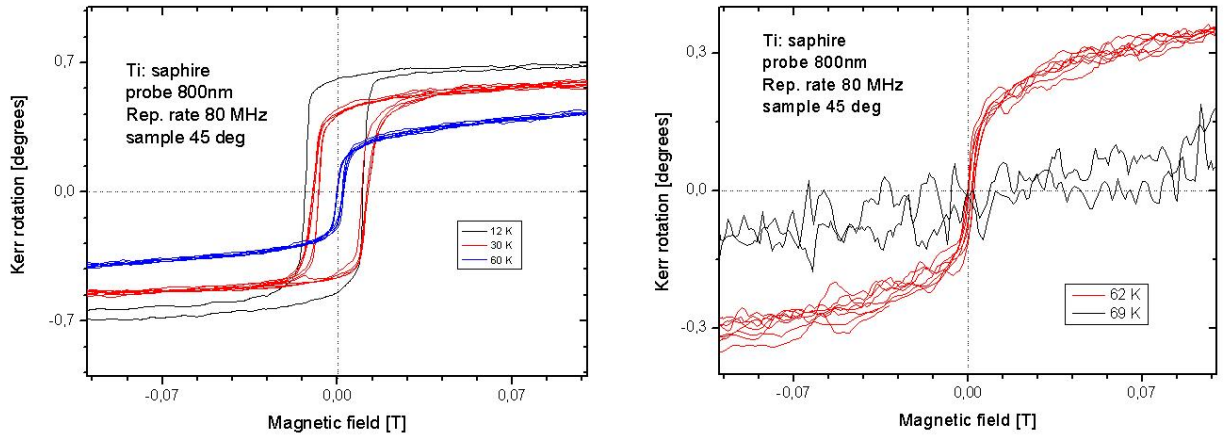


Figure 3.2: Hysteresis loop of sample 1 at different temperatures.

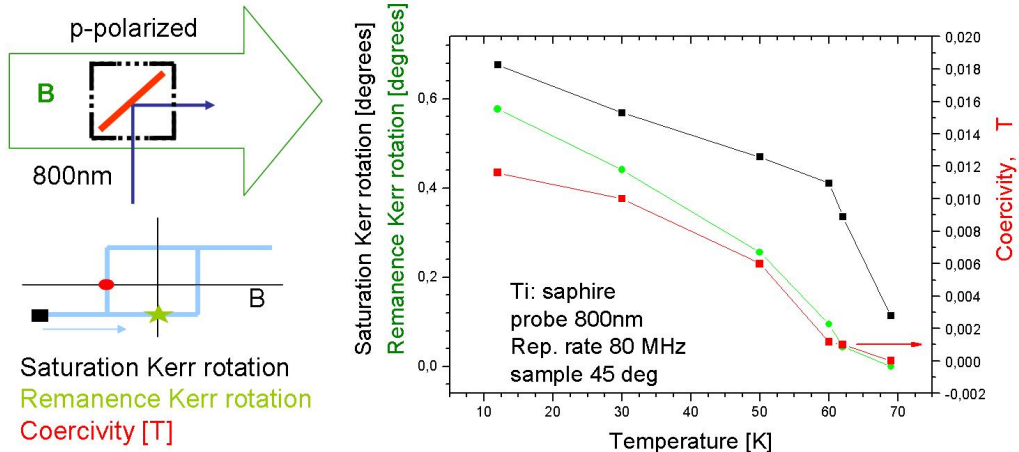


Figure 3.3: Left) the big green arrow represents the direction of the applied magnetic field. The red bar represents the EuO film. The blue arrow is the p-polarized laser beam and the black box is the optical cryostat. The black dotted lines represents the cryostat windows. Right) Coercivity, remanence and saturation magnetization at different temperatures for sample 1.

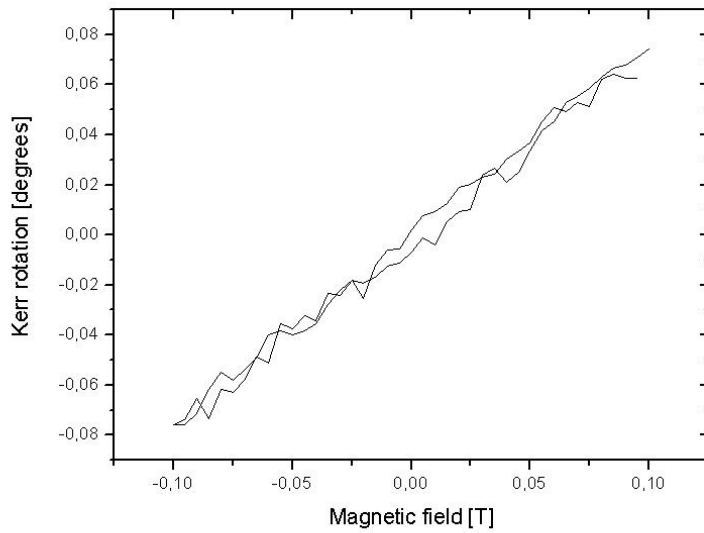


Figure 3.4: Hysteresis loop of sample 1 in the polar geometry at 10 K.

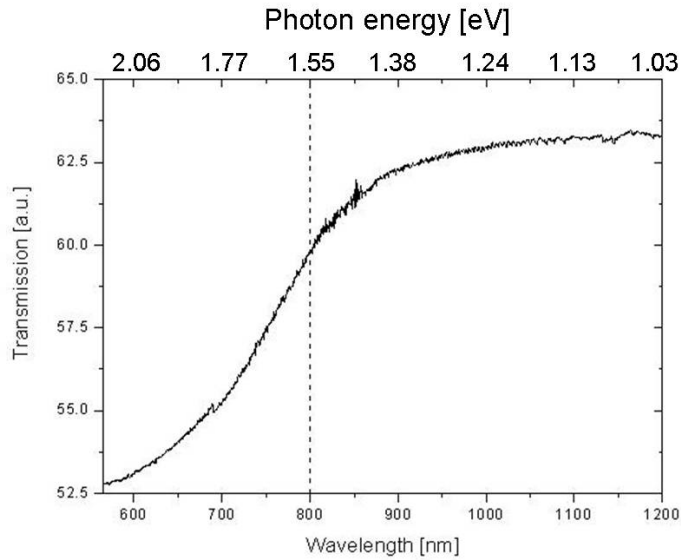


Figure 3.5: *Transmission spectrum at room temperature for sample 1.*

Sample 3

For sample 3 only a hysteresis loop was measured at 4 K in the described 45° degrees geometry, see figure A.1 in the appendix. Because the saturation Kerr rotation is small compared with the other samples, this sample is not used in the transient hysteresis experiments. The coercivity is much larger than in sample 1: 11 mT in sample 1 at 10 K and 30 mT in sample 3 at 4 K. The reasons for this difference will be discussed later in the discussion section.

Sample 4

Hysteresis loops at different temperatures are shown in figure A.2 in the appendix. Processed data is shown in figure 3.6. The magnitude of the coercivity is comparable with sample 1, 11 mT at 10 K. However, the saturation Kerr rotation at 10 K is much larger, 1.7 degrees.

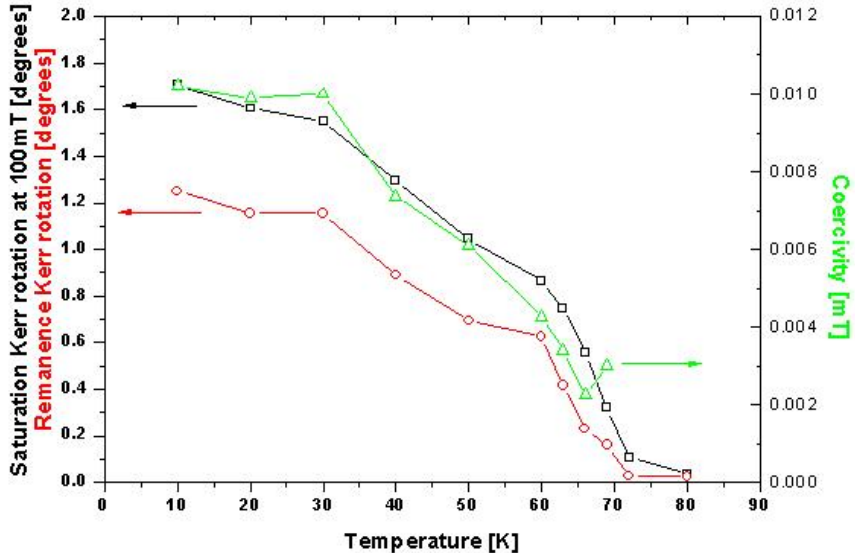


Figure 3.6: *Coercivity, remanence and saturation magnetization at different temperatures for sample 4.*

Sample 5

The same was done for sample 5, as shown in figure A.3 in the appendix and in figure 3.7. The reflection of this sample was very bad due to the inhomogeneity. The saturation Kerr rotation is quite large, 1.1 degrees, but the coercivity is small, 8.0 mT.

Sample 6

Hysteresis loops at different temperatures are shown in figure A.4 in the appendix. Processed data is shown in figure 3.8. The saturation Kerr rotation at 100 mT and 10 K has a value of 0.47 degrees and the coercivity at 10 K has a value of 33 mT.

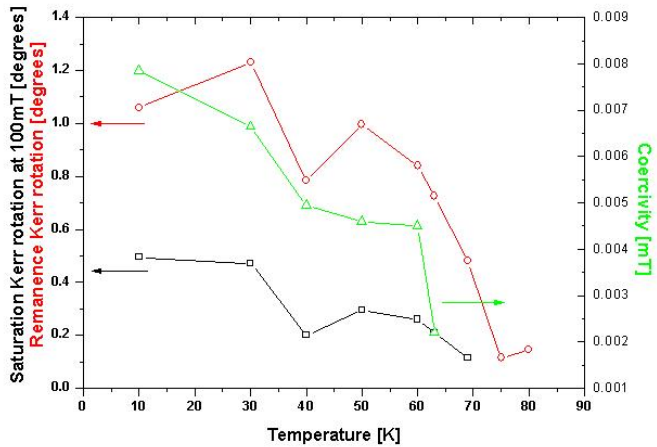


Figure 3.7: *Coercivity, remanence and saturation magnetization at different temperatures for sample 5.*

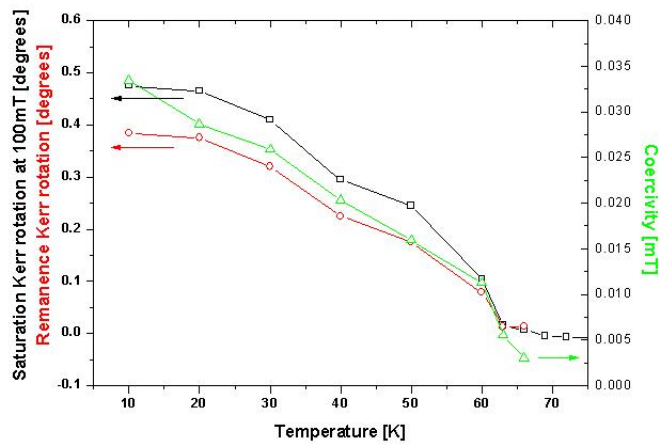


Figure 3.8: *Coercivity, remanence and saturation magnetization at different temperatures for sample 6.*

Discussion

Some important results from this section are shown in the following table. In this table the magnitude of the saturation Kerr rotation and coercivity at a temperature of 12 K for sample 1, at a temperature of 4 K for sample 3 and at a temperature of 10 K for samples 4, 5 and 6 are listed. The measurement temperatures are slightly different but this is not very important for the comparison since the slope of the magnetization in the magnetization versus temperature graph is very small at low temperatures. In all the samples the ordering temperature is around 69 K.

Nr.	Thickness EuO film	Coercivity [mT]	Saturation [degrees]
1	20nm	11	0.67
3	60nm	30	0.70
4	25nm	11	1.7
5	60nm	8.0	1.1
6	60nm	33	0.47

The observed values for the saturation Kerr rotation are between 0.47 - 1.1 degrees whereas the coercivity is between 8.0 mT and 33 mT. The magnitude of the coercivity is related to the samples anisotropy, single ion and shape anisotropy, and to the direction of magnetization relative to the applied magnetic field. For all the samples the single ion anisotropy is the same, assuming that perfect stoichiometric EuO was made, and can not lead to changes in the coercivity. However, also the amount of defects in the different samples can differ, leading to a different value for the coercivity. It is unclear how exactly the number of defects is related to the magnitude of the coercivity. The samples can also have different anisotropy due to the sample's shape. In principle one can state, the thinner the EuO film, the higher the shape anisotropy. However, no thickness/coercivity trend is observed in our measurements indicating that not only the shape anisotropy is important.

Finally, in another attempt to explain the results, a single domain particle model can be used: the Stoner-Wohlfarth model [30], where one only needs to consider the coherent domain rotation. When the direction of the applied magnetic field to the easy axis of magnetization is 90° , no hysteresis will be observed. However, when the applied magnetic field is parallel to the easy axis, the observed hysteresis (coercivity) will be maximum. When there are a lot of domains, with all possible orientations, the hysteresis loops have to be averaged and there will be some hysteresis. In the EuO samples there must be a lot of domains in order to minimize the energy associated with dipolar (magnetic) fields. When there is shape anisotropy, the preferred magnetization orientation of these domains can be in-plane. In our experimental geometry, the applied magnetic field makes an angle of 45° with the film plane, resulting in a decreased coercivity compared to the case when the applied magnetic field is in plane. According to the Stoner-Wohlfarth model, the 'real' coercive field, in the case that the applied magnetic field is parallel to the easy axis, is twice the value as measured when the applied magnetic field is at 45° .

SQUID measurements done by Lettieri *et al.* [47] on an 66 nm epitaxial EuO film reveal that the magnetization must be in-plane : when the applied magnetic field is in plane, hysteresis with a coercivity of 75 mT is observed. However, when the applied field is parallel to the surface normal, no hysteresis was observed. In our experiments in the polar geometry, in which the refracted light makes a small angle with the surface normal, no hysteresis could be observed either. From this, together with the SQUID measurements, can be concluded that the magnetization is most likely in-plane in the 20 nm thick sample 1.

In the polar case, at saturation, the magnetization is parallel to the k-vector of the refracted beam giving a large Kerr effect. The observed value of the Kerr effect is, for unknown reasons smaller, than in the 45° geometry. In the 45° geometry, the light is refracted and according to Snell's law, the angle of the refracted 800 nm light with the surface normal can be calculated, which becomes 18 degrees (in an air/MgO/EuO interface). In this case the magnetization makes an angle of 18 degrees with the k-vector of the refracted beam. Since the Kerr rotation is proportional to $\vec{k} \cdot \vec{M}$, the Kerr rotation is expected to be large as well and experiments confirm this.

The coercivity of the 60 nm thick sample 3 is 30 mT whereas the coercivity of the 60 nm thick sample 5 is 8.0 mT. Finally after introducing different possibilities for this, we can attribute the differences to a different number of defects, to the Eu-O stoichiometry and to a possible change in the samples' structure at the interface structure. Since the Kerr effect is the rotation of polarization of the reflection from a magnetic medium, it is sensitive to interface. EuO is grown on MgO which has a smaller lattice constant, 5.1 Å for EuO and 4.1 Å for MgO at room temperature. Due to the large lattice mismatch, in the first few EuO layers the strain in the EuO film has to relax. Change in the interface structure can affect magnitude of the Kerr effect. Despite an attempt was made to maintain the same grow conditions in every sample, small changes lead to large differences in the magnitude of the Kerr rotation and coercivity.

To conclude, the differences in coercivity and saturation Kerr rotation are most likely due to differences in the samples' structure: stoichiometry, interface structure, number of defects and thickness. No thickness/coercivity trend is observed in our measurements. Most likely, the magnetization of sample 1 is in-plane.

3.3.2 Transient Hysteresis Measurements

The transient hysteresis data in this paragraph are divided into two sections. In one section the measurements on sample 1 are shown and in the other section, the measurements on sample 4 are shown. These are the only samples on which transient hysteresis experiments were performed. First the measurements are described: the shape can correspond to an induced magnetization or an induced demagnetization. In the final paragraph the results are discussed.

Sample 1

Transient hysteresis measurements on sample 1 and 4 were done in the 45 degree geometry (described before). Before showing the results, we would like to emphasize the importance of the absolute sign. In figure 3.9, a normal Kerr hysteresis loop is shown. The value of the Kerr rotation is denoted by θ . When

a pump pulse hits the sample, the Kerr rotation can change by $\Delta\theta$ leading to a value for the Kerr rotation of $\theta + \Delta\theta$. By a lock-in technique, the difference Kerr rotation $\Delta\theta$ is measured. In figure 3.9, an example is given where only the saturation and remanence Kerr rotation changes. Depending on the sign, the measured transient hysteresis can be an induced demagnetization as well as an induced magnetization. It is also possible that apart from the saturation and remanence Kerr rotation, also the coercivity changes. In figure 3.10 A the shape of a hysteresis loop when the saturation, coercivity and remanence Kerr rotation increases, is shown whereas in 3.10 B the shape of a hysteresis loop when the saturation, coercivity and remanence Kerr rotation decreases, is shown.

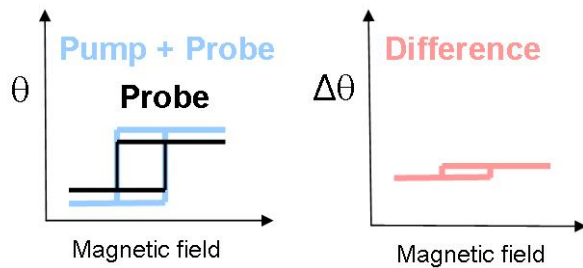


Figure 3.9: *The sign of the transient hysteresis loop is crucial. In this example an increase of the magnetization by a pump pulse is shown. The normal hysteresis loop θ is measured with a probe pulse. When also a pump pulse is acting, the signal becomes $\theta + \Delta\theta$. By the lock-in technique, the difference $\Delta\theta$ is measured.*

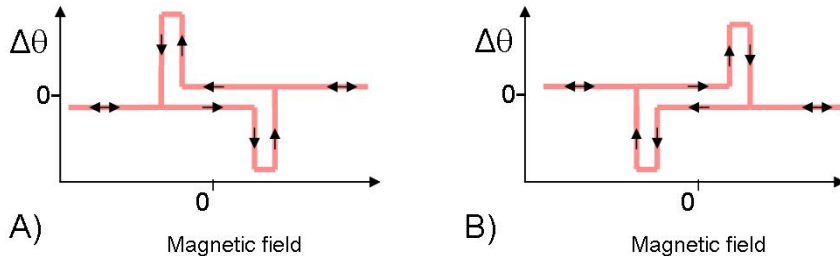


Figure 3.10: *A) transient hysteresis in the case of increased coercivity, remanence Kerr rotation and saturation Kerr rotation. B) transient hysteresis in the case of decreased coercivity, remanence Kerr rotation and saturation Kerr rotation.*

The transient hysteresis data for sample 1 at -1 ps and +1 ps delay at different temperatures are shown in figure 3.11. In the measurements for sample 1 it is unclear what the sign is. However, the relative sign of the minus 1 ps and plus 1 ps signal is known and one assumption can be made: the sign of sample 4 at negative delays corresponds to an induced demagnetization and it

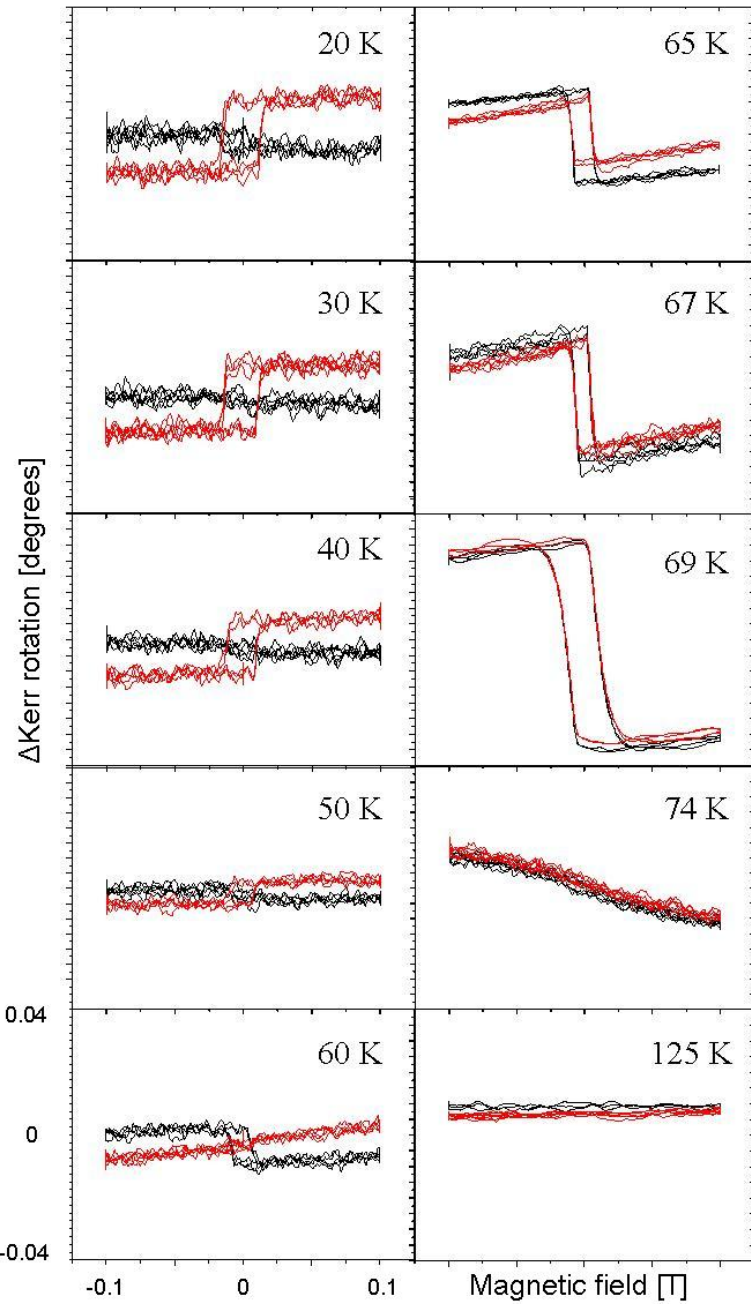


Figure 3.11: Transient Hysteresis of sample 1. Red corresponds to a delay of 1 ps (pump before probe), black corresponds to a delay of minus 1 ps (probe before pump).

is expected that this must be also the case for sample 1.

When at positive delays an opposite sign is measured compared to minus delays, there can be concluded that this is an induced magnetization process because the sign at negative delays is known (assumption) and corresponds to an induced demagnetization. At least when is assumed that the direction of the magnetization has not changed: an induced magnetization sign can be also measured when $\vec{k} \cdot \vec{M}$ increases but \vec{M} stays constant. This means that the direction of the magnetization has changed.

The shape of the transient hysteresis with a delay of + 1 ps and in the temperature range of 20-60 K corresponds to an induced magnetization as is shown in figure 3.10. The remanence and saturation Kerr rotation increases whereas the coercivity stays almost constant. The induced magnetization is decreasing with increasing temperature (the height of the loop decreases). In the 66-74 K temperature range, the shape corresponds to an induced demagnetization which means that the sign of the saturation Kerr rotation at +100 mT has changed sign compared to the sign in the 20-60 K range. Again, the coercivity stays constant. The temperature dependence of the saturation Δ Kerr rotation is shown in figure 3.12, which summarizes the data in figure 3.11.

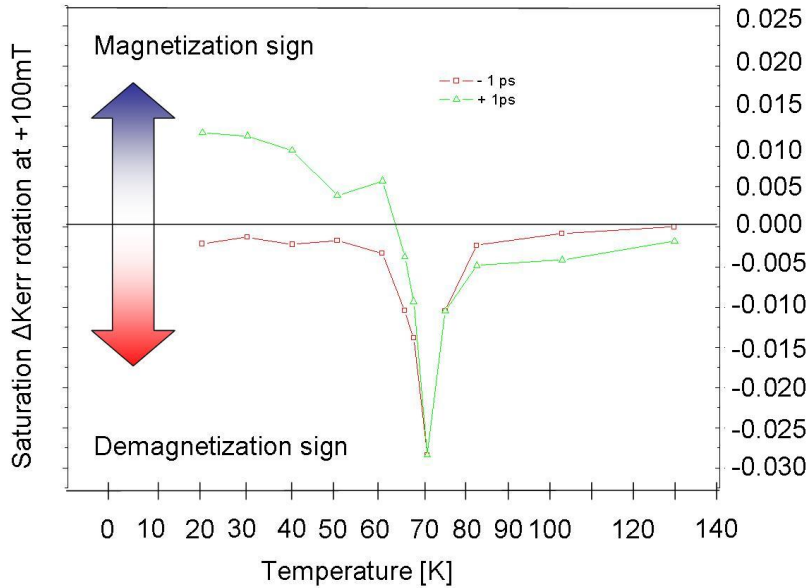


Figure 3.12: *Saturation Δ Kerr rotation at + 100 mT in degrees versus temperature for negative and positive delays in sample 1*

In order to calculate the magnitude of the induced electronic effect, the loop at negative delays in figure 3.12 have to be subtracted from the loop at positive delays in figure 3.12. The result of this is shown in figure 3.13, where the saturation Kerr rotation at (+100mT, +1ps) is subtracted from the saturation Kerr rotation at (+ 100mT, -1ps). The induced electronic effect is large at low temperatures and decreases with increasing temperature.

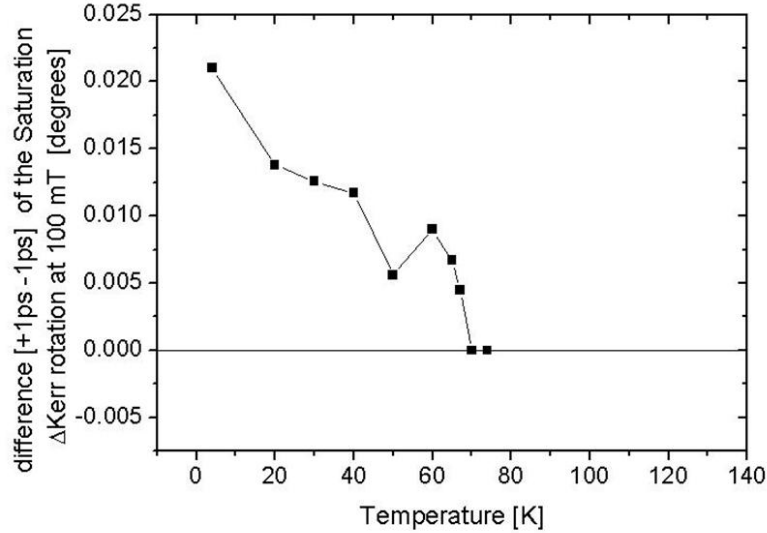


Figure 3.13: *Electronic effect in sample 1. Saturation Kerr rotation at (+100 mT, +1ps) is subtracted from the saturation Kerr rotation at (+100 mT, -1ps).*

Discussion

In the magnetically ordered state, below about 70 K, the sign of the electronic effect corresponds to an increase in magnetization. An explanation for this result can be found either in the described microscopical theory, or in a rotation of the magnetization. The transient Kerr rotation can be written as:

$$\Delta\theta \sim \Delta(f)\vec{k} \cdot \vec{M} + f\Delta(\vec{k} \cdot \vec{M}) \quad (3.7)$$

f is some proportionality constant, \vec{k} is the k-vector of the light, and \vec{M} is the sample's magnetization. The magnitude of the Kerr rotation can change due to a change in the proportionality constant. The proportionality constant can change due to changes in the complex refractive index (\tilde{n}_1) in EuO, which can be expected because of the photoexcited carriers in conduction band, see equation 2.59 and 2.60. This is not what is intended to be measured. We want to measure a change in the direction or magnitude of the magnetization. As suggested by Koopmans [41], also the Kerr ellipticity can be measured: when both the Kerr rotation and ellipticity change, this is an indication that we are looking to a change of the magnetization and not of the proportionality constant.

In our experiments only the Kerr rotation was measured and first is assumed that the proportionality constant does not change. However, it is possible that \tilde{n}_1 changes and because of this that the proportionality constant changes as well. Since the coercivity does not change, this is an indication that the anisotropy has not changed and the direction of the magnetization has not changed either.

The results can therefore be explained by a change in the magnitude of \vec{M} . As described in paragraph 2.7.2, about magnetization dynamics in magnetic semiconductors, we are in the regime where the electrons relax in the conduction band. The lattice temperature have increased already. The increased magnetization and thus the increased exchange interaction, can be explained by the FKL model in which the exchange interaction is thought to be mediated by the conduction electrons. In our experiments the photodoping, which can be calculated since the dielectric function and pump fluence is known, is about 0.4%. At higher temperatures, starting from 20 K, the induced electronic changes become smaller, as was shown in figure 3.13. The conduction electrons can increase the exchange constant less effectively when the localized magnetic moments are less ordered at higher temperatures. The signal at positive delays in the 80-125 K range is positive at positive and negative magnetic fields. No hysteresis is observed for this temperature range and it is unclear why there is a flat positive signal at all magnetic fields.

The induced demagnetization signal at negative delays becomes stronger at higher temperatures. In an first attempt to explain the results, let us consider the effect of overall heating. To do this a (normal, not transient) hysteresis loop at a higher temperature is subtracted from a hysteresis loop at a lower temperatures. The result is shown in figure 3.14. This signal corresponds to a heating signal which can be measured in the transient hysteresis. Heating will reduce not only the remanence and the saturation Kerr rotation but the coercivity as well. Since the remanence, saturation Kerr rotation and coercivity follow the temperature behavior of the magnetization, the expected change in percentages is almost the same for all parameters when the temperature is increased. However, changes in the coercivity will result in spikes in the difference hysteresis loop. Heating effects are expected to be more pronounced close to the ordering temperature due to the increased slope of the magnetization in the magnetization versus temperature graph, see figure 3.15A.

At 12 K, $\Delta\theta$ at minus delays is about 0.004 degrees which is 0.6 % from its original value θ . In order to get this effect from heating, the temperature has to rise by 0.5 K to 12.5 K. Then, the coercivity changes from 11.60 mT at 12 K to about 11.55 mT at 12.5 K. The change in coercivity is 0.05 mT and difficult to observe since the magnetic field step size was about 0.7 mT. At 62.0 K the slope in the magnetization temperature graph is steeper. Here to get the induced (saturation) demagnetization, the temperature has to increase 0.5 K as well, to 62.5 K. At this temperature, the (interpolated) coercivity is 0.92 mT whereas the coercivity is 0.99 mT at 62 K. The difference, which corresponds to the width of the coercivity spike is 0.07 mT. No spikes were seen in the transient hysteresis experiments indicating that the signal is probably not due to a heating effect but it is also possible that the magnetic field step size was too large. The expected width of the spikes coming from a change in the coercivity due to heating is about 0.05 mT whereas the step size was about 0.7 mT. The magnitude of the saturation Kerr rotation at minus delays follows the increase of the slope in magnetization temperature graph indicating that indeed heating might be important.

The effect of heating from a laser pulse can be estimated as followings using a film thickness of 50 nm. When 800 nm (photon energy 1.55 eV) 1 nJ pulse is absorbed in a volume of $50 \mu\text{m} \times 50 \mu\text{m} \times 50 \text{ nm}$, where $50 \mu\text{m}$ is the focus size (square) and 50 nm the film thickness, the temperature rise can be

calculated if the heat capacity is known. Taking into account the reflection at the interface and using the absorption coefficient, one can calculate that after passing the EuO film, the intensity of the transmitted beam is reduced by 24% with respect to the incoming beam due to absorption. At 20 K and 69 K the heat capacity is 5 J/mol K and 40 J/mol K respectively [5] giving an increase of the temperature of 7.7 K and 0.97 K at 20 K and 69 K, respectively. However, at long timescales, due to diffusion, the temperature rise is expected to be much lower. On short timescales an electron can absorb the 1.55 eV and relax to the bottom of the conduction band (1.2 eV) giving 0.35 eV to the lattice. The temperature increase on short timescales, when diffusion is neglected, is 1.7 K at 10 K and 0.21 K at 69 K. The calculated temperature rise on short timescales at 10 K gives a decrease in the coercivity of 0.17 mT. This corresponds to the expected width of the spikes in the transient hysteresis and is smaller than the magnetic field step size (0.6 mT).

The signal at negative delays is not only because of heating, also trapping of free carriers in the conduction band, and the subsequent thermal excitation of them, might play an important role. Steeneken [3] already showed that the photoconductivity lives very long after the laser is turned off there are still carriers in the conduction band 1250 ns after the pump pulse hits the sample. It was mentioned before that the ground state of the $4f^65d^1$ excited state has a lower value for the angular momentum and this can explain the observed induced demagnetization as well since the magnitude of the magnetization of this excited state is lower than the magnetization in the ground state.

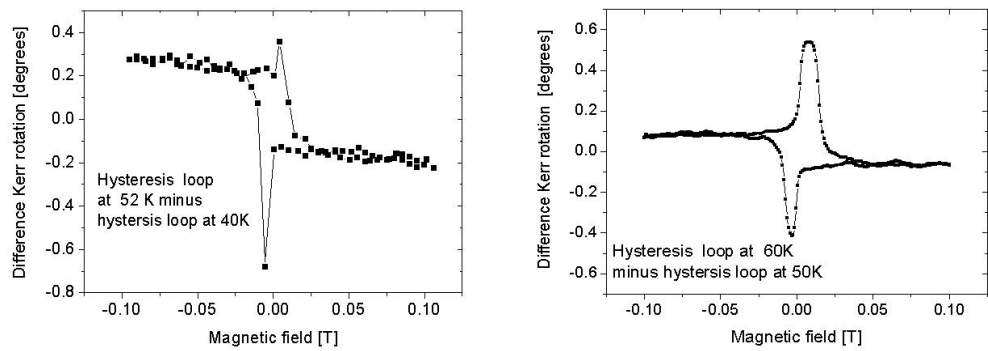


Figure 3.14: *A)* Difference Kerr rotation, high minus low temperature, for sample 4. *B)* Difference Kerr rotation for sample 1

In figure 3.15B also the transient hysteresis at 4 K is shown. The sign is opposite to the one at 20 K and corresponds to an induced demagnetization (at +1 ps). The sign is difficult to determine (we made the assumption that at negative delays there is an induced demagnetization, as was discussed) since there is almost no hysteresis and it might be that the sign is opposite. However it is difficult to increase the magnetization at this temperature because it is close to its maximum: all moments are aligned. The discussion will be continued in the

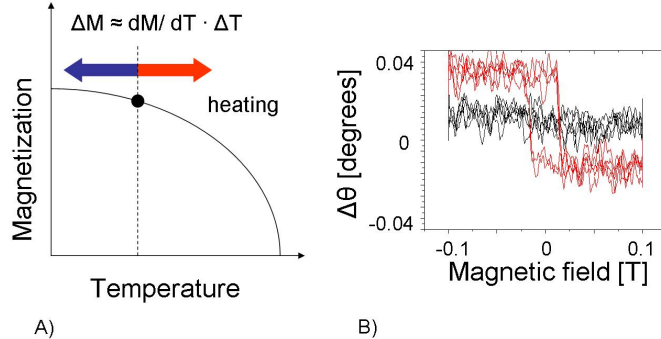


Figure 3.15: A) magnetization versus temperature for sample 1. B) Transient hysteresis at 4 K for sample 1.

following sections and at the end of chapter 4. The most important conclusion now is that the induced demagnetization at negative delays is most probably due to heating and due to electrons that are not recombined with holes. No change in the coercivity is observed. The expected changes in the coercivity due to heating are very small, probably too small to measure. Assumed is that the Kerr signal comes from a change in the magnetization and not in a change in the proportionality constant or change in the direction of the magnetization. This assumption has to be verified in future experiments. A possible change in the direction of the magnetization might result as well in a change in the coercivity. At +1 ps an induced magnetization was observed probably coming from an increase of the exchange interaction. This electronic effect becomes smaller closer to the ordering temperature.

In the next chapter transient hysteresis measurements on sample 4 are shown. The thickness of this sample is almost the same as for sample 1: 20 nm sample 1, 25 nm sample 4. The substrate however, is different. For sample 1 the substrate is YSZ in order to minimize the lattice mismatch. Sample 4 is grown on MgO and there is some strain in the first EuO layers.

Sample 4

The data from the measurements on sample 4 are different from the one described for sample 1. The sign for this measurement set is known and no assumptions have to be made. In this measurement set a lot of points in the delay/temperature plane are taken. The measurement conditions are the same as in the discussed transient hysteresis measurements of sample 1. On the next page the results for 20 K are shown. The data for the other temperatures, including a detailed description of the data, are shown in the appendix because of the huge amount of graphs.

In figure 3.16, the transient hysteresis results for 20 K are shown. At -10 ps there is a heating effect. Right after the pulse hits the sample at 0 ps, the shape of the graph (the sign of the saturation Kerr rotation) corresponds to an induced demagnetization. The sign of the electronic effect, which can be obtained when the graph at positive delays is subtracted from the graph at negative delays,

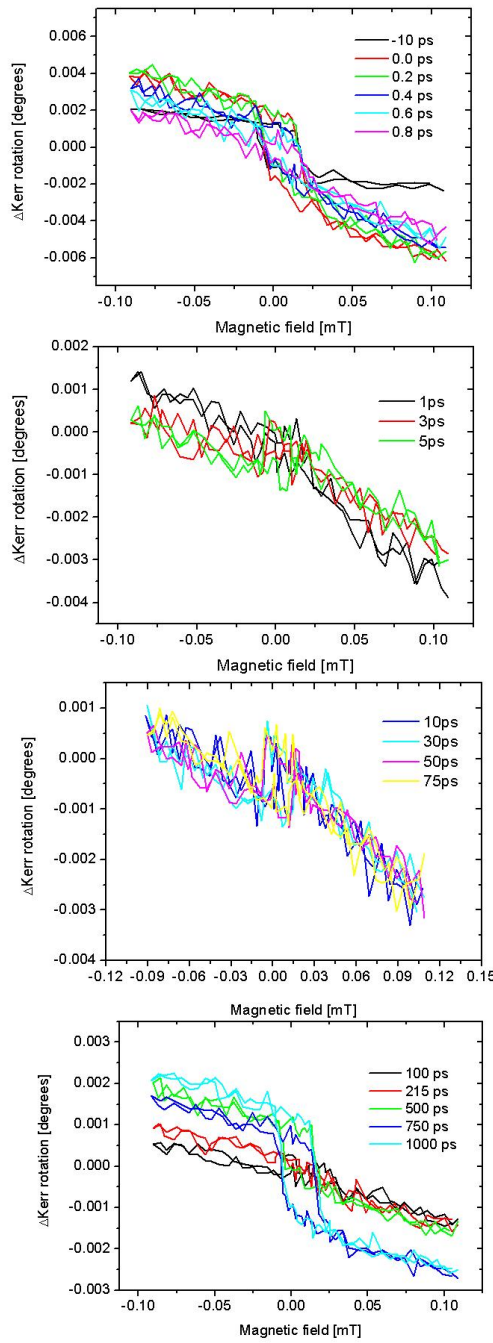


Figure 3.16: *Transient hysteresis for sample 4 at 20 K for different pump probe delays.*

corresponds to an induced demagnetization. Then, the induced demagnetization shape changes to an induced magnetization shape which reaches a maximum at about 75 ps. After that, from 75 ps, the induced magnetization changes gradually in an induced demagnetization again which reaches a maximum at 1000 ps. The data of the other temperatures can be found in the appendix. The results are summarized in figure 3.17 and discussed in the next section.

Discussion

The behavior of the transient hysteresis at different temperatures and delays is summarized in figure 3.17. A white bar means that the hysteresis loop stays constant with respect with the one at a smaller delay. A red bar means that the hysteresis loop changes towards an induced magnetization. A blue bar means that the hysteresis loop changes towards an induced magnetization. The first small bar on the left stands for the change in magnetization at 0 ps compared to -10 ps.

The general behavior for 20-69 K is as follows. First there is an instantaneous induced demagnetization followed by a change towards an induced magnetization in the first hundred picoseconds and by a change towards an induced demagnetization in the 100-1000 ps range. The transient hysteresis loops at -10 ps for different temperatures are shown in figure B.12 in the appendix, and to summarize, the saturation Kerr rotation at -10 ps is shown in figure 3.18.

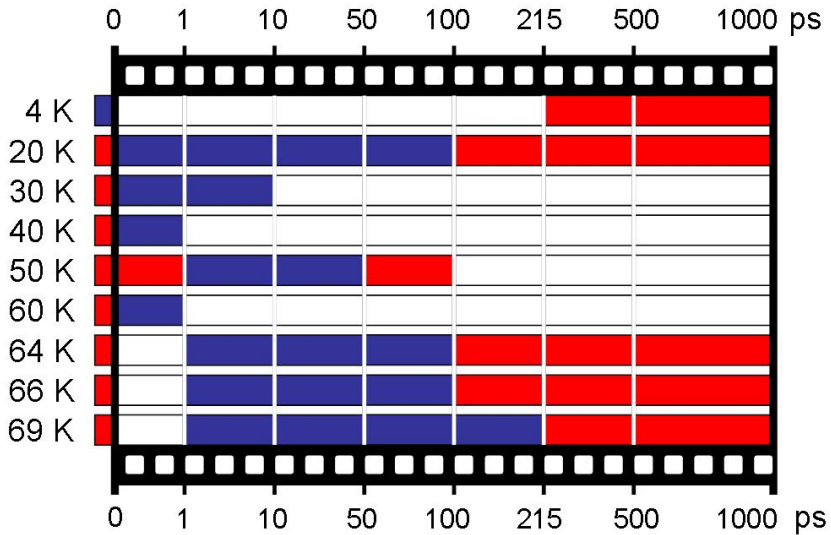


Figure 3.17: *Transient hysteresis for sample 4 at different temperatures and delays. A white bar means that the hysteresis loop stays constant with respect with the one at a smaller delay. A red bar means that the hysteresis loop changes towards an induced magnetization. A blue bar means that the hysteresis loop changes towards an induced magnetization. The first small bar on the left stands for the change in magnetization at 0 ps compared to -10 ps.*

The saturation $\Delta\theta$ rotation is about 0.004 degrees at +0.2 ps and 10 K with corresponds to 0.24% of θ . As was mentioned for sample one, if the induced demagnetization arises from heating, the coercivity has to change as well. This can give a spike in the transient hysteresis with a height of about 1.2 degrees (which corresponds to the value of the remanence) and a width of about 0.2 mT. The used magnetic field step size in the measurements of sample 4 is 2.5 mT and is much larger than the width of the expected spike so it is possible that the spike can not be observed.

As can be seen in figure 3.19, the induced demagnetization at minus delays, probably due to heating, has a maximum at 40 K. The size of the heating effect depends on the slope of the magnetization in the magnetization versus temperature graph, on the heat capacity of the EuO film but also on the thermal conductivity of the whole sample including the substrate and the capping layer. The heat capacity increases with the temperature towards the orderings temperature. However, dM/dt has a maximum at the orderings temperature. This can give a maximum of the heating effect at intermediate temperatures: not at low temperatures where dM/dt is small and not at high temperature (close to T_c) where the heat capacity is large but somewhere in between. The reason that this behavior is not observed for sample 1 can be that the temperature dependence in the thermal conductivity of sample 1 is different which can be the case due to the different substrates, stoichiometry, number of defects.

The observed electronic effect in sample 4 also differs from that observed in sample 1, see figure 3.19. In this figure, the saturation Kerr rotation at (+100 mT, +1 ps) is subtracted from the saturation Kerr rotation at (+100 mT, -10 ps). The sign corresponds to an induced demagnetization for 20-69 K and to an induced magnetization for 4 K. This in contrast to the sign in sample 1 which corresponds to an induced demagnetization for 4 K and an induced magnetization for 20-69 K. However, for samples 1 and 4, there are no changes in the coercivity, indicating that we are not looking to a rotation of the magnetization. It is unclear why the signs are different for sample 1 and 4. For the first 10 ps, state filling effects can be important, which can result in a decrease in the proportionality constant and lead to a decrease of the saturation Kerr rotation. However, this must be the same for sample 1 and 4 since the same pump fluence is used.

To summarize, for sample 4, there is a change towards an induced magnetization (blue color in figure 3.17) in the 1-100 ps range roughly, for 20, 30, 50, 64, 66 and 69 K. For 20 and 69 K the shape of the hysteresis loop has even changed in an induced magnetization shape. In the 100-1000 ps range roughly, for 4, 20, 64, 66 and 69 K, there is a change towards an induced demagnetization indicating that there might be some heating. The instantaneous induced demagnetization at 0 ps is probably due to a change in the proportionality constant or due to change in the total angular momentum J after excitation. It is unclear why there is so much difference in the electronic effect between sample 1 and 4. The magnitude of the heating effect at minus delays is different for sample 1 and 4. This discussion will be continued at the end of chapter 4 after discussing the transient Kerr rotation (dynamics) and the transient reflectivity measurements.

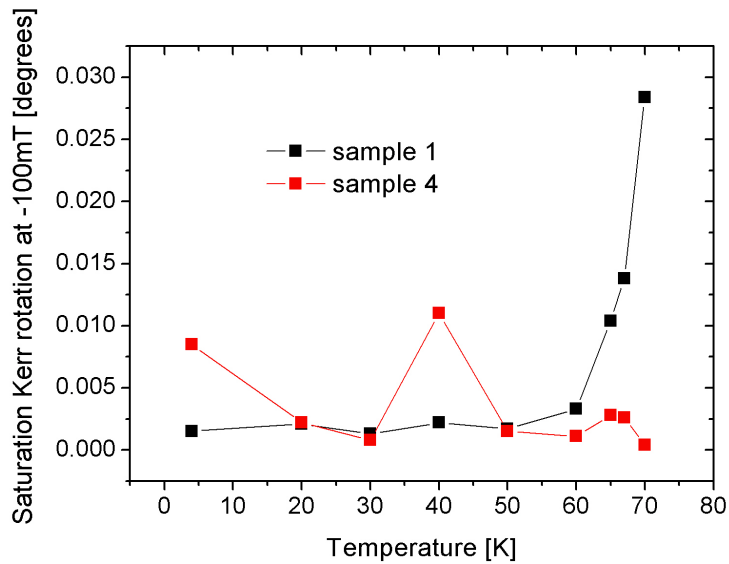


Figure 3.18: *Saturation Δ Kerr rotation of the transient hysteresis of sample 1 and 4 at -1 ps and -10 ps, respectively, for different temperatures.*

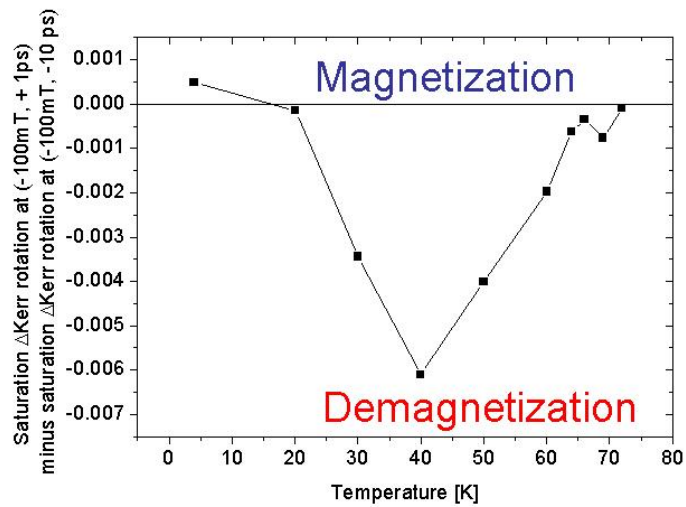


Figure 3.19: *Sign of the electronic effect determined from the difference in the saturation Kerr rotation at -10 ps and +1 ps.*

Chapter 4

Transient Kerr Rotation and Reflectivity

4.1 Transient Kerr Rotation Measurements

In this paragraph, the transient Kerr rotation measurements are shown for sample 1 (in the 45° geometry using linear polarized 800 nm pump and probe pulses). The applied magnetic field is 100 mT, so the saturation Δ Kerr rotation is measured. The data for different temperatures are shown in figure C.1 and C.2 in the appendix and summarized in figure 4.1 on the next page. The lines are shifted in such a way that the signal at minus delays is at $\Delta\theta=0$. Before this shift, all signals at negative delays were at negative $\Delta\theta$ indicating that it was an induced demagnetization. The dotted lines represents the amount of $\Delta\theta$ by which the lines are shifted: the black line for 20 K, the green line for 40 K and the orange line for 70 K. Stays the $\Delta\theta$ signal below the dotted line, then it still corresponds to an induced demagnetization. However, when the signal is above the dotted line, then there is an induced magnetization. For 20 K, right after the excitation at 0 ps, there is an induced magnetization. In the 0-100 ps range this induced magnetization is increasing followed by a decrease of the induced magnetization in the 100-1000 ps range. For 40 K there is an induced magnetization as well, which increases till 20 ps and decreases afterwards. For 30 and 50 K there is also an induced magnetization. It increases till 10 ps, which is the end of the measurement. At higher temperatures, the situation is different. For 60 K, the induced magnetization stays almost constant after excitation at 0 ps. Then there is a small decrease towards an induced demagnetization till 100 ps. After that it increases towards an induced magnetization. However, it does not reach the dotted line so there is no net induced magnetization. The data for 60 K however are quite noisy. For 65 K the magnetization stays constant right after excitation. After that it increases and reach the dotted line at about 12 ps. Then it decreases till about 150 ps, it increases again till 500 ps and decreases after 500 ps. There is (almost) no transient Kerr rotation signal for 70 and 80 K. The data are discussed in the second next paragraph after showing the transient reflectivity results.

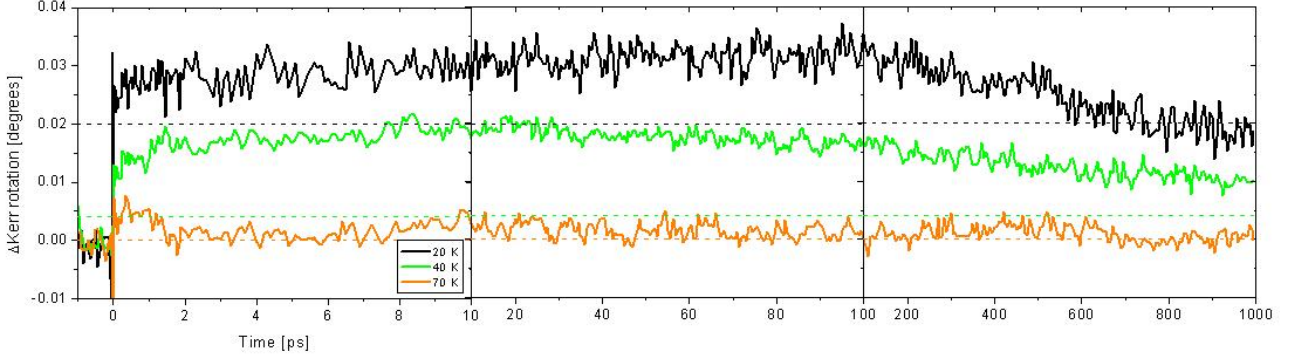


Figure 4.1: *Transient Saturation Kerr rotation of sample 1 for different temperatures.*

4.2 Transient Reflectivity Measurements

In this section, the transient reflectivity data for sample 1 are shown, see figure D.1 and D.2. This was measured as a probe for the carrier dynamics. In principle, we can do the same as was done for the Kerr effect.

$$\Delta R = f\Delta n_{photo} + \Delta f n_{photo} \quad (4.1)$$

f is some proportionality constant and n_{photo} is the number of photoexcited carriers. A change in the reflectivity can occur because of changes in the carrier concentration or due to changes in the proportionality constant. In this case it is quite clear that the proportionality constant can change as well, for instance when carriers relax to the bottom of the conduction. When the magnetization changes, the conduction band can shift resulting in a ΔR signal. How this exactly will influence ΔR , (positive signal or negative signal) is difficult to predict. In the first 10 ps, for different temperatures, a definite trend is evident. For 20 K ΔR is negative, after that it is increasing with temperature and becomes positive. The $\Delta R/R$ signal for larger delays will not be discussed. The only thing that I can say that it is a complex signal that is not just increasing first and decreasing afterwards. This is most likely due to changes in the proportionality constant. From this data it is difficult to extract a decay constant and this will not be done.

4.3 Discussion and Conclusion

The data of this chapter and the previous chapter is summarized in figure 4.2. For comparison, in figure 4.3, the data of sample 4 is shown. The general behavior for sample 1 in the 20-65 K range is as follows. At 0 ps there is an induced magnetization compared to -1 ps. In the 0-25 ps range the induced

effect is increasing towards an induced magnetization and in the 100-1000 ps range, the induced effect is decreasing towards an induced demagnetization, except for 60 K where the induced magnetization increases between 100 and 500 ps. For 20-50 K there is a net induced magnetization during the whole 1000 ps. For 65 K the magnetization increased compared to -1 ps but for most delays it still has the sign of an induced demagnetization.

When sample 4 is compared with sample 1, one can see that there are differences and similarities. One difference is that the electronic effect, which is the signal at +1 ps minus the signal at -1 ps (sample 1) or -10 ps (sample 4), corresponds to an induced magnetization for sample 1 and to an induced demagnetization for sample 4. The electronic effect is quite small, 0.35% for sample 4 and 1.7% for sample 1. However, the trend in the dynamics after +1 ps for both samples is similar. On short time scales, the first 25 ps, the induced effect is increasing towards an induced magnetization. However on long time scales, 100-1000 ps, the induced effect is decreasing towards an induced demagnetization.

Also the effect at minus delays is different. Whereas for sample 1 the heating effect is increasing towards the ordering temperature, sample 4 has a maximum at 40 K. We attribute this to the difference in the temperature dependence of the thermal conductivity which can be different for the two samples due to changes in the sample's structure (defects, stoichiometry, substrate, interface). This can also influence the electronic effect. There can be two competing effects on short timescales. First, the increase of the exchange interaction which can explain the induced magnetization for sample 1 and second, the spin polarization of the conduction band electrons. The hot conduction band electrons can spin-flip scatter with impurities or defects in an Elliot-Yafet mechanism. When it is assumed that the electrons during the excitation process does not flip their spins, this can give, together with heating effects, an induced demagnetization at +1 ps. Since the number of impurities or defects can be different for sample 1 and 4 (which can also lead to changes in the coercivity) the momentum scattering time can be different and when this time is shorter in sample 4 compared to sample 1, this can account for the observed differences. The spin orientation relative to the 4f moment may also affect the increase in the exchange interaction.

As discussed, for sample 1 the electronic effect corresponds to an induced magnetization whereas for sample 4 it corresponds to an induced demagnetization. However, for sample 4 at 20 K and 215 ps, there is an induced magnetization as well. The change from induced demagnetization at +1 ps towards an induced magnetization is a relatively slow process. The trend in the dynamics after +1 ps for both samples is similar. On short time scales the induced effect is increasing towards an induced magnetization. However on long time scales the induced effect is decreasing towards an induced demagnetization. On short timescales, after a few ps, the lattice temperature will rise and because of a (4f) spin-lattice interaction this can lead to a demagnetization. However what we have seen is an increase of the magnetization during the first 25 ps for most temperatures. It is possible that a cooler conduction electron gas can more effectively increase the exchange interactions. As was seen for sample 1 where the induced magnetization at +1 ps decreases with increasing temperature. The decrease on longer timescales (>100ps) can be explained by processes like carrier trapping, recombination and carrier diffusion. The goal of this conclusion was to introduce a possible explanation for what we have seen. However

more effort needs to be done, as will be discussed in the final chapter.

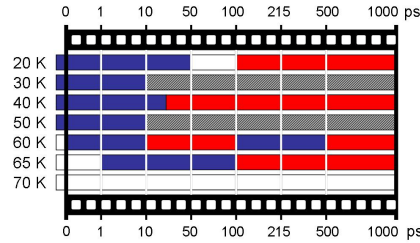


Figure 4.2: *Transient hysteresis for sample 1 at different temperatures and delays. A white bar means that the hysteresis loop stays constant with respect with the one at a smaller delay. A red bar means that the hysteresis loop changes towards an increase in the magnetization. A blue bar means that the hysteresis loop changes towards a decrease of the magnetization. The first small bar on the left stands for the change in magnetization at 0 ps compared to -1 ps. A grey bar means that for this region there are no data*

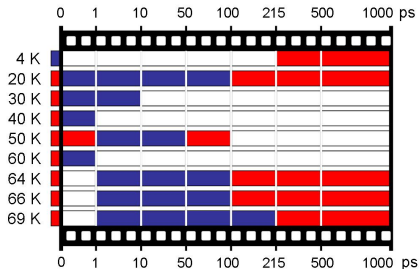


Figure 4.3: *Transient hysteresis for sample 4 at different temperatures and delays. A white bar means that the hysteresis loop stays constant with respect with the one at a smaller delay. A red bar means that the hysteresis loop changes towards an induced magnetization. A blue bar means that the hysteresis loop changes towards an induced demagnetization. The first small bar on the left stands for the change in magnetization at 0 ps compared to -10 ps.*

Chapter 5

Conclusion and Outlook

The goal of the EuO master research project is to study and to understand the magnetization dynamics in EuO but also to control the magnetism in EuO. Samples were made in Köln, samples were characterized and transient hysteresis measurement, transient Kerr rotation measurements and transient reflectivity measurements were performed. During the whole year but especially at the end, we tried to understand the data. What happened: induced magnetization or induced demagnetization and is there trend?

The Theory chapter was written to provide some ideas what kind of things can happen with the magnetization in EuO after a strong laser pulse hits the sample and can probably also help to understand future experiments. Discussed was that the 5d conduction electrons can enhance the exchange interactions but also that the total magnetic moment can change after an optical excitation. In chapter 3 and 4 the results were presented. We succeed to make good quality EuO samples. They all have an ordering temperature of about 69 K. However the saturation Kerr rotation and coercivity of all the samples is different although an attempt was done to have the same grow conditions. Even samples with the same thickness are different. We attribute the differences in the coercivity and saturation Kerr rotation to the samples structure: the number of defects, the strain at the interface and the stoichiometry.

Also transient hysteresis experiments were performed. In sample 1 we were able to increase the magnetization by a strong linear polarized pump pulse in the 20-65 K temperature range. Suggested was that this increase of the magnetization at +1 ps occurs because the conduction electrons enhance the exchange interactions. At negative delays there is a transient hysteresis signal as well. The induced demagnetization at minus delays was attributed to heating. Although no change in coercivity was seen, which you would expect from heating, we reasoned that the change might be to small to measure.

In sample 4 the situation is different: a demagnetization was seen at +1 ps compared to -10 ps. This was attributed to the change in impurities/defects which changes the momentum scattering time. The shorter the momentum scattering time, the faster the conduction electron gas can demagnetize because of the Elliot-Yafet spin-flip scattering mechanism. Assumed was that right after excitation the conduction electrons are spin polarized (no spin flips during the excitation). When this effect is larger than the increase of the exchange interaction, this can lead to a demagnetization on short timescales.

Apart from the differences there were also similarities between sample 1 and 4. In the magnetization dynamics for both samples an increase of the magnetization compared to the induced magnetization at 0 ps was seen in the first 25-50 ps at most temperatures. However at larger delays, (> 100 ps) mostly changes towards an induced demagnetization were seen. The increase in the Kerr signal towards an induced magnetization can be due to changes in the proportionality constant but also due to an increase of the exchange constant. It is possible that a cooler conduction electron gas can more effectively increase the exchange interactions. As was seen for sample 1 where the induced magnetization at +1 ps decreases with increasing temperature. The decrease in the magnetization can occur because of heating.

As most master thesis will conclude, more experiments need to be done to provide a definite answer on what is exactly happening in EuO (microscopically) after a strong optical excitation. In future experiments we advise to measure apart from the Kerr rotation, the ellipticity as well. By this, better conclusion can be drawn, since this is a test if there are changes in the proportionality constant of the Kerr effect. This can be done by using an Photo Elastic modulator (PEM) for the probe beam and look to the signal on the frequency of the PEM (rotation) and the double frequency of the PEM (ellipticity) using a single photodetector coupled to a lock-in amplifier. When we do not want to use a PEM, the halve wave plate in front of the Wollaston prism can be replaced by a quarter wave plate. Now, by looking to the difference in signal on detector A and B, the ellipticity can be measured.

It is also very important to measure the absolute sign of the signal because this can make the difference between an induced magnetization and an induced demagnetization. When in future experiments the magnetization dynamics are measured, the Kerr rotation and ellipticity should be measured at plus and minus magnetic field. The signal at positive and negative fields should have an opposite sign but must be equal. Only when this is done it is possible to prove that really magnetization dynamics is studied.

Future experiments may include time-resolved photoluminescence experiments, to see how long the carriers live, but also transient hysteresis measurements using 1.2 eV pump pulses. Because in this case electron are excited to the bottom of the conduction band, the carriers do not have to relax in the conduction band and there is less heating. Now the electronic effect can be larger compared to the heating effect. When the experiment is performed right above the orderings temperature, because of the increased exchange interaction mediated by the conduction electrons, it might be possible to make a paramagnetic to ferromagnetic phase transition using linear polarized 1.2 eV pump pulses.

Another experiment, right below the orderings temperature, can be done using 1.0 eV circular polarized pump pulses. 1.0 eV is somewhere in the conduction band tail. By the inverses Faraday effect which is a Raman-like coherent optical scattering process, circular polarized laser pulses can induce a static magnetic field [48]. Because the absorption at 1.0 eV is small, the effect of a magnetic field pulse can be studied. Since Eu-rich EuO is a GMR compound, a magnetic field pulse can increase the amount free carriers. This can be probed by THz pulses which are sensitive to free electrons. Free carriers can enhance the exchange interactions. The possible increase of the magnetization can be followed in the transient hysteresis using 800 nm linear polarized probe pulses.

Chapter 6

Acknowledgements

First I want to thank Paul van Loosdrecht for being a very good and nice supervisor. On every moment, I could come by to your office to ask or discuss something, which I really appreciated. Further I want to thank Dmitry for doing the measurements together with me in the first part of the year, for the discussions and for proofreading my thesis. Of course I want to thank the whole Optical Condensed Matter Physics group as well for the nice atmosphere in the group, and especially Dima, Pedro, Audrius and Arjen for helping me in the lab, and Bram for the discussions during the coffee breaks.

The samples that I made, together with Ronny Sutarto, were synthesized in Köln in the group of Hao Tjeng. I want to thank them for the two weeks that I spend in Köln. Finally I want to thank Petra Rudolf for being my referent and for reading the 101 pages (!!!) of my thesis.

Bibliography

- [1] A.V. Kimel, G.V. Astakhov, G.M. Schott, A. Kirilyuk, D.R. Yakovlev, G. Karczewski, W. Ossau, G. Schmidt, L.W. Molenkamp, Th. Rasing Physical Review Letters, **92**, 237203, (2004)
- [2] H. Ott, S.J. Heise, R. Sutarto, Z. Hu, C.F. Chang, H.H. Hsieh, H.-J. Lin, C.T. Chen, L.H. Tjeng, Physical Review B, **73**, 09407, (2006)
- [3] P.G. Steeneken, *PhD thesis*, University of Groningen, (2002)
- [4] C. Kittel, *Introduction to Solid State Physics*, John Wiley, New York (1996)
- [5] K. Ahn, A. O. Pecharsky, K. A. Gschneidner, V. K. Pecharsky, Journal of Applied Physics, **97**, 063901, (2004)
- [6] L. Passel, O.W. Dietrich, J. Ab-Nielsen, Physical Review B, **14**, 4897, (1974)
- [7] N. Miyata, B.E. Argyle, Physical Reviews, **157**, 448, (1967)
- [8] W.P. Wolf, Physical Reviews, **5**, 1152, (1957)
- [9] D.B. Gosh, M. De, S.K. De, Physical Review B, **70**, 115211, (2004)
- [10] A. Mauger, C. Godart, Physical Reports, **141**, 51, (1986)
- [11] J.B. Torrance, M.W. Shafer, T.R. McGuire, Physical Review Letters, **29**, 1168, (1972)
- [12] M.R. Oliver, J.O. Dimmock , A.L. McWhorther, T.B. Reed, Physical Review B, **5**, 1087, (1972)
- [13] Y. Shapira, S. Foner, T.B. Reed, Physical Review B, **8**, 2299, (1973)
- [14] H. Rho, C.S. Snow, S.L. Cooper, Z. Fisk, A. Comment, J-Ph Ansermet, Physical Reviews Letter, **88**, 127401, (2002)
- [15] J.P. Desfours, J.P. Nadai, M. Averous, Solid State Communications, **20**, 691, (1976)
- [16] C. Llinares, E. Monteil, G. Bordure, C. Paparoditis, Solid State Communications, **13**, 205, (1973)
- [17] T.J. Konno, N. Ogawa, K. Wakoh, K. Sumiyama, K. Suzuki, Japanese Journal of Applied Physics, **35**, 6052, (1996)

- [18] K. Kajita, T. Masumi, Applied Physics Letters, **21**, 332, (1972)
- [19] D.I. Khomskii, G.A. Sawatsky, Solid State Communications, **102**, 87-99, (1997)
- [20] D.I. Khomskii, *Lecture notes*, Groningen, (2004/2005)
- [21] J.B. Goodenough, *Magnetism and the Chemical Bond*, John Wiley, New York, (1963)
- [22] C.J. Ballhausen, *Ligand field theory*, McGraw-Hill, Boston (1962)
- [23] N.V. Nguyen, J.B. Goodenough, Physical Review B, **52**, 324, (1995)
- [24] T. Kasuya, IBM Journal of Research and Development, **14**, 214, (1970)
- [25] P.H. Taylor, O. Heinonen, *Condensed Matter Physics*, Cambridge University Press, Cambridge, (2002)
- [26] B. Chevalier, A. Wattiaux, J.L. Bobet, Journal of Physics: Condensed Matter, **18**, 1743, (2006)
- [27] W. Nolting, S. Rex, S. Mathi Jaha, Journal of Physics: Condensed Matter, **9**, 1301, (1997)
- [28] M.B. Salamon, M. Jaime, Reviews of Modern Physics, **73**, 583, (2001)
- [29] R. Schiller, W. Nolting, Solid State Communications, **118**, 173, (2001)
- [30] S. Blundell, *Magnetism in Condensed Matter*, Oxford University Press, Oxford, (2001)
- [31] M.H. Abd Elmeguid, R.D. Taylor, Physical Review B, **42**, 1048, (1990)
- [32] S. Heathman *et al.*, Journal of Alloys and Compounds, **230**, 89, (1995)
- [33] A.K. Zvezdin, V.A. Kotov, *Modern Magnetooptics and Magneto-optical Materials*, Institute of Physics Publishing, Dublin, (1997)
- [34] M. Fox, *Optical Properties of Solids*, Oxford University Press, Oxford (2001)
- [35] E. Hecht, A. Zajac, *Optics*, Addison Wesley, Boston, (2003)
- [36] Z.J. Yang, M.R. Scheinfein, Journal of Applied Physics, **74**, 6810, (1993)
- [37] C.Y. You, S.C. Shin, Journal of Applied Physics, **84**, 541, (1998)
- [38] Jeong-Won Lee, Jonggeal Kim, Sang-Koog Kim, Jong-Ryul Jeong, Sung-Chul Shin, Physical Review B, **65**, 144437, (2002)
- [39] D.A. Mazurenko, *PhD thesis*, Universiteit Utrecht, (2004)
- [40] J.P. Callan, A.M.-T. Kim, C.A.D. Roeser, E. Mazur, *Ultrafast Dynamics and Phase Changes in Highly Excited GaAs*, Harvard University, Internal report

- [41] B. Koopmans, J.J.M. Ruikhrok, F. Dalla Longa, W.J.M.de Jonge, Physical Review Letters, **95**, 267207, (2005)
- [42] E. Beaupaire, J.C. Merle, A. Daunois, J.-Y. Bigot, Physical Review Letters, **76**, 4250, (1996)
- [43] G.P. Zang, W. Hübner, Physical Review Letters, **85**, 3025, (2000)
- [44] J. Wang, C. Sun, J.Kono, A. Oiwa, H. Munekata, L.J. Sham, Physical Review Letters, **95**, 167401, (2005)
- [45] Pil Hung Son, K.W. Kim, Physical Review B, **66**, 035207, (2002)
- [46] W. Hübner, K.H. Bennemann, Physical Review B, **53**, 3422, (1996)
- [47] J. Lettieri, V. Vaithyanathan, S. K. Eah, J. Stephens, V. Sih, D. D. Awschalom, J. Levy, D. G. Schloma, Applied Physics Letters, **83**, 975, (2003)
- [48] A.V. Kimel, K. Kirilyuk, P.A. Usachev, R.V. Pisarev, A.M. Balbashov, Th. Rasing, Nature, **435**, 655, (2005)

Appendix A

Hysteresis

In the appendix, all the hysteresis, transient hysteresis, transient Kerr rotation and transient reflectivity data are shown in different sections. In this section the hysteresis loops for sample 4 are shown, measured with 800 nm light with a 45 degree angle of incidence. The applied magnetic field makes a angle of 45 degrees with the sample plane.

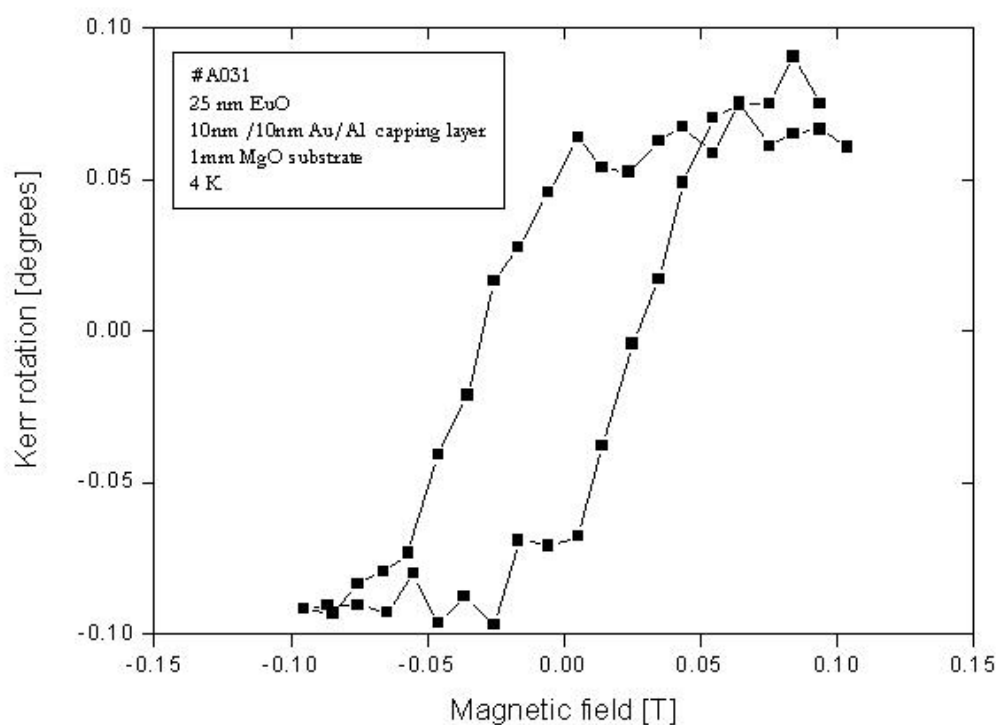


Figure A.1: Hysteresis loop of sample 3 at 4 K.

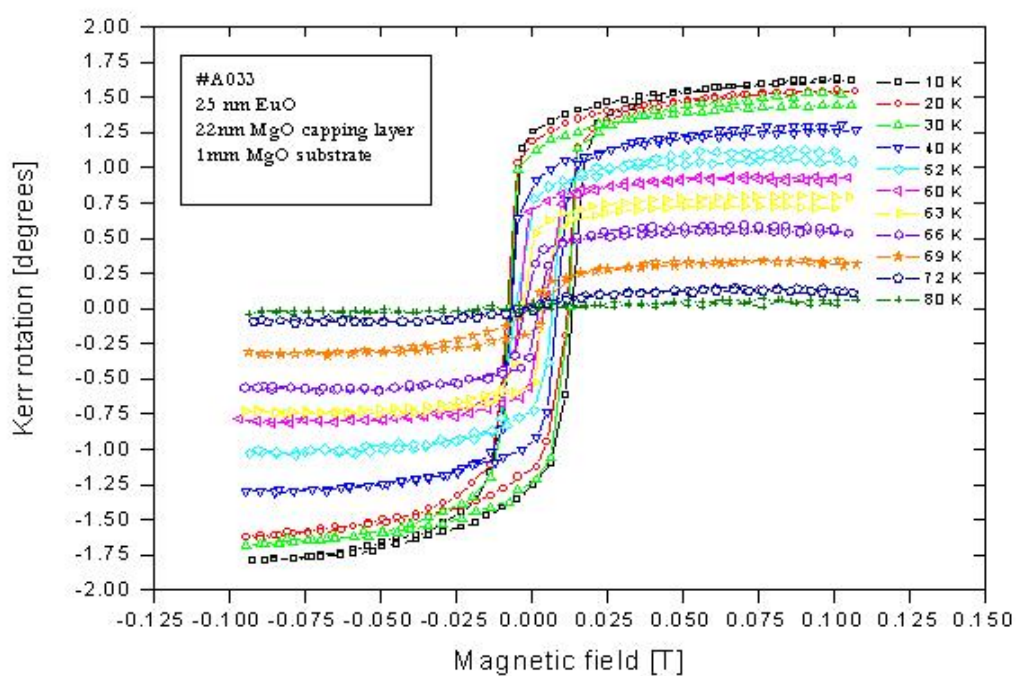


Figure A.2: *Hysteresis loop of sample 4 at different temperatures.*

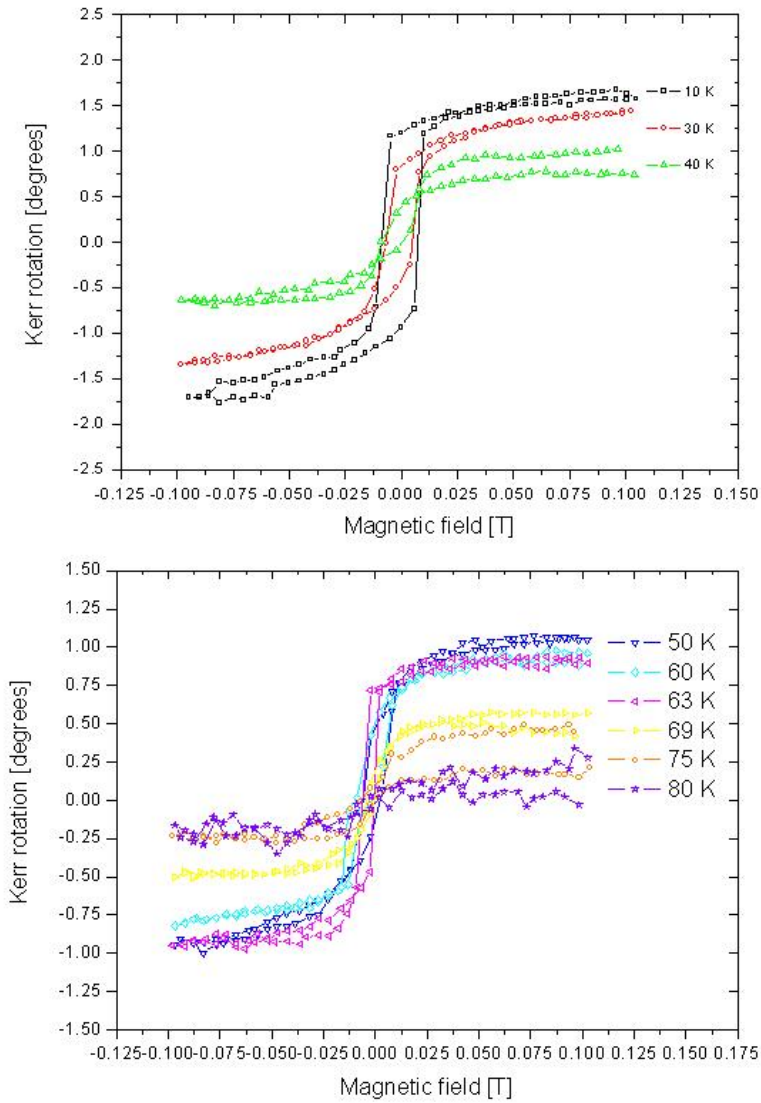


Figure A.3: Hysteresis loop of sample 5 at different temperatures.

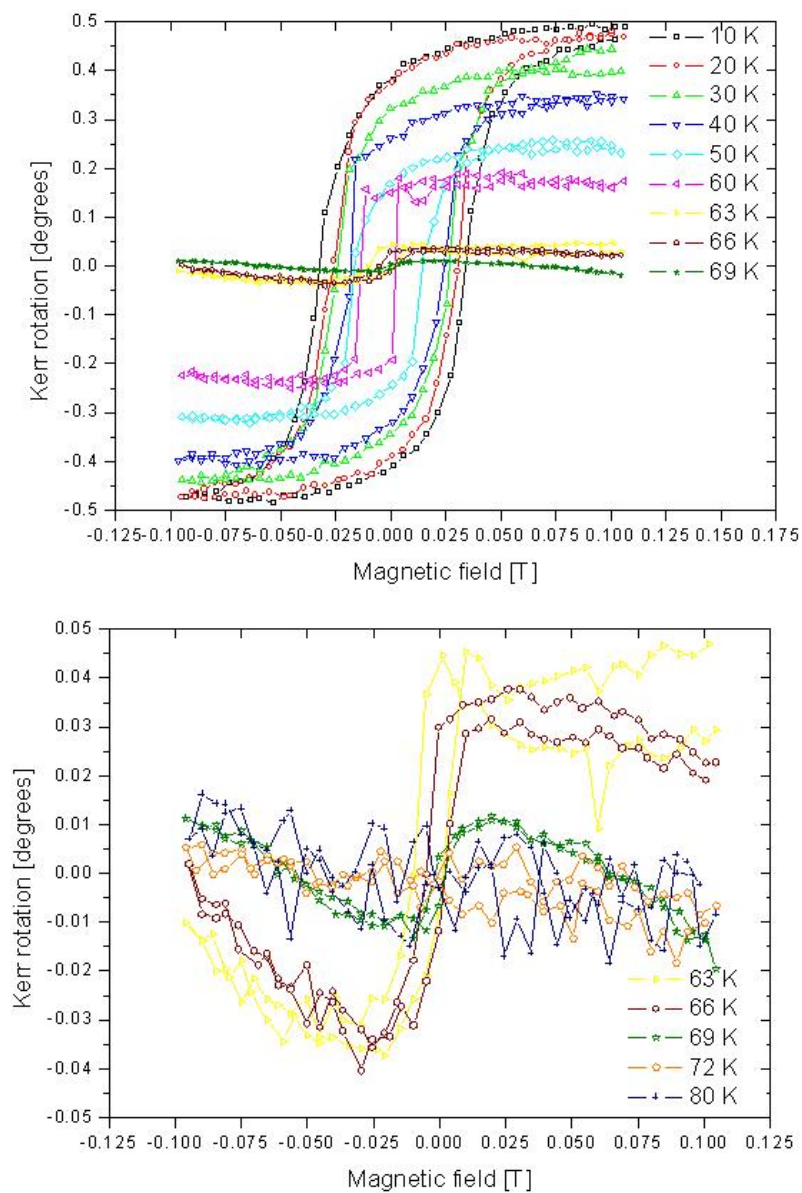


Figure A.4: Hysteresis loop of sample 6 at different temperatures.

Appendix B

Transient Hysteresis

In this section the transient hysteresis data for sample 4 are shown measured with 800 nm pump and probe beams with a 45 degree angle of incidence for the probe. Transient hysteresis loops are measured at different temperatures. The applied magnetic field makes a angle of 45 degrees with the film plane. The pump fluence is about 1 mJ/cm².

The results at 4 K for different pump probe delays are shown in figure B.1. The observed shape corresponds to an induced demagnetization. At minus 10 ps, most likely because of the heating as discussed before, there is an induced demagnetization. When the loops at positive delays are subtracted from the one at minus 10 ps, the electronic contribution is obtained, at least at short timescales were heating plays no role and assuming that the proportionality constant for the Kerr effect does not change. For the first and second graph in figure B.1 the hysteresis did not change to much with respect to the loop at minus delays. There is a very small induced magnetization at 0 ps (the maximum in the Kerr rotation/ pump- probe delay graph) with respect to the loop at -10 ps. After that, from 0 to 215 ps, the hysteresis loop did not change. At longer timescales, from 215 ps, the induced demagnetization becomes larger. This is, however, not only due to the electronic contribution anymore since there is also heating.

The data for 30 K are shown in figure B.2 and figure B.3. The saturation Kerr rotation at -10 ps at 30 K is very small indicating that the sample has its original temperature (30 K) after 1250 ns. At 0 ps there is an induced demagnetization compared to -10 ps. The induced demagnetization decreases slightly (towards an induced magnetization) with increasing pump probe delay from 0 to 10 ps. From about 50 ps, the transient hysteresis loop stays constant. In contrast with sample 1, there is an induced demagnetization at +1 ps for sample 4 whereas there is an induced magnetization in sample 1.

The time-dependent behavior for 40 K is shown in figure B.4 and B.5 and is different. At minus delays there is a quite large induced demagnetization and at plus delays there is hardly no change. In the 0-1 ps range, there is a change towards an induced magnetization. At larger delays there are almost no changes in the transient hysteresis loop.

The data for 50 K are shown in figure B.6. At -10 ps there is a small induced demagnetization. At 0 ps the induced demagnetization has increased compared to -10 ps. In the 0-1 ps range there is an increase in the induced demagnetization

as well. In the 1-50 ps range there is change towards an induced magnetization. After 75 ps there are almost no changes in the transient hysteresis.

Let us look to the data for 60 K, see figure B.7. Again, at -10 ps there is an induced demagnetization. At 0 ps the induced demagnetization has increased compared to -10 ps, followed by a change towards an induced magnetization in the 0-1 ps range. After +1 ps there is hardly no change in the hysteresis loop.

The behavior for 64 K, 66 K and 69 K is very similar and is shown in figures B.8, B.9 and B.10, respectively. First there is an induced demagnetization at 0 ps compared to -10 ps, followed by a change towards an induced magnetization in the 1-100/215 ps range and a change towards an induced demagnetization in the 100/215-1000 ps range. For 69 K, at 215 ps, the shape is that of a induced magnetization. Above the orderings temperature at 72 K no hysteresis is observed anymore, see B.11.

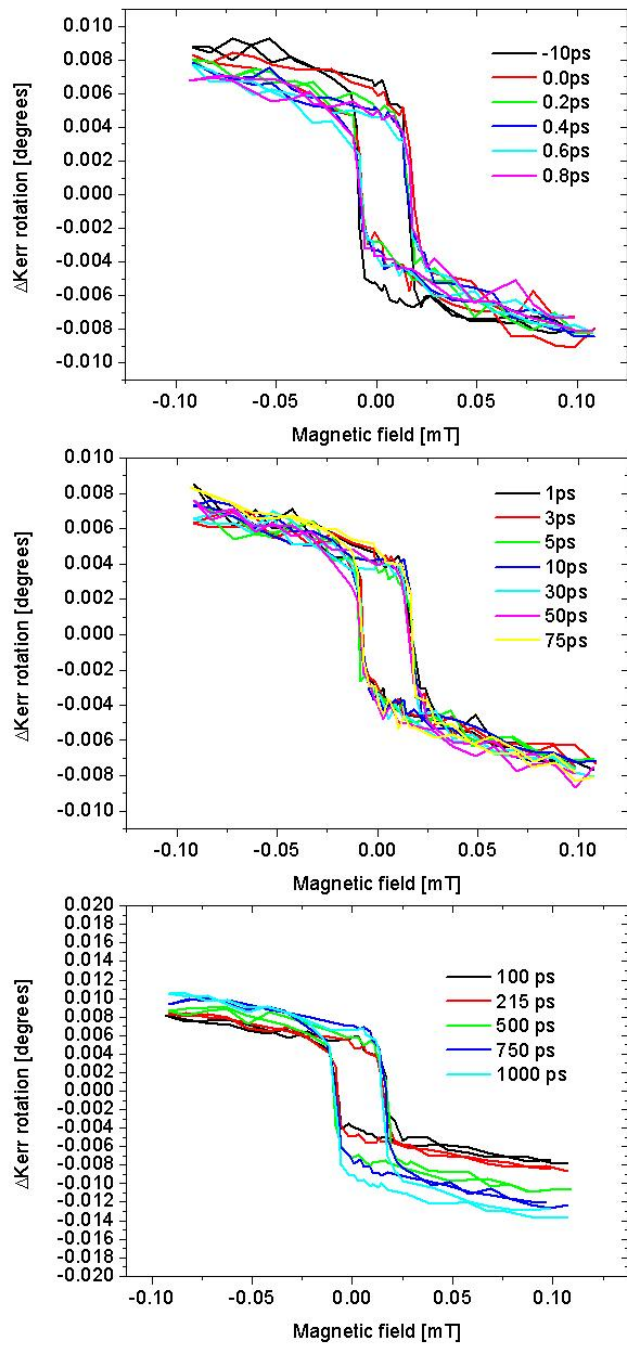


Figure B.1: Transient hysteresis for sample 4 at 4 K for different pump probe delays.

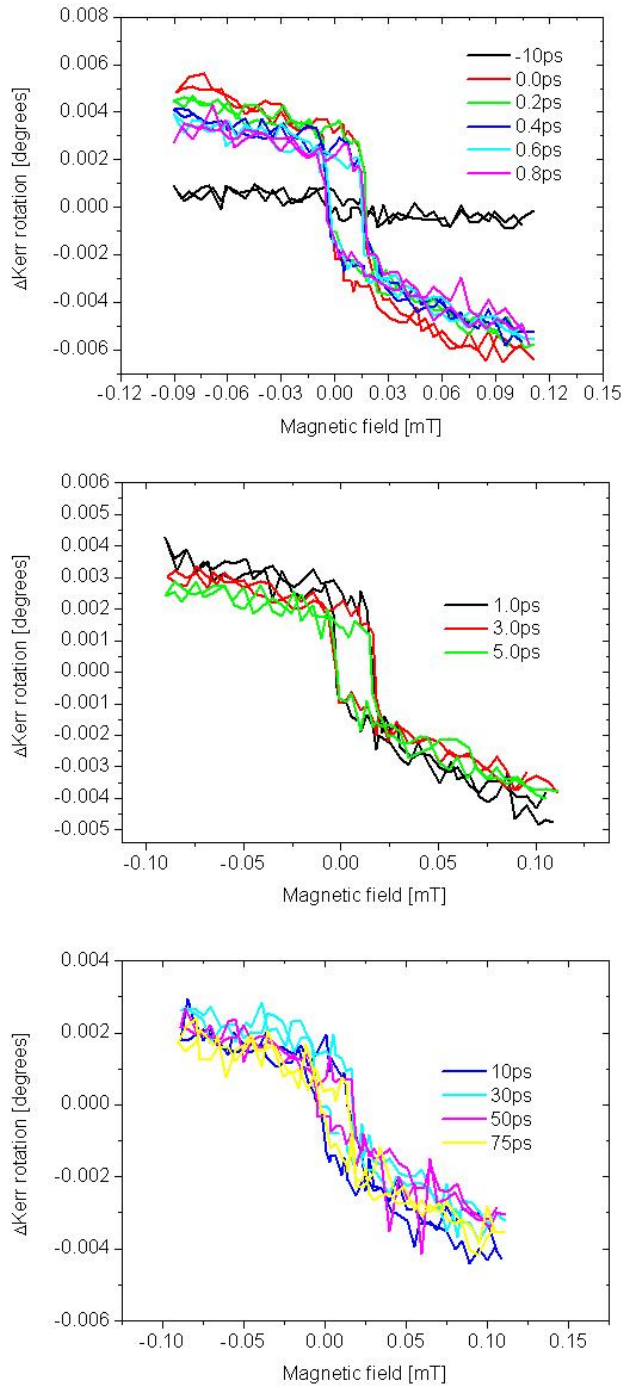


Figure B.2: *Transient hysteresis for sample 4 at 30 K for different pump probe delays.*

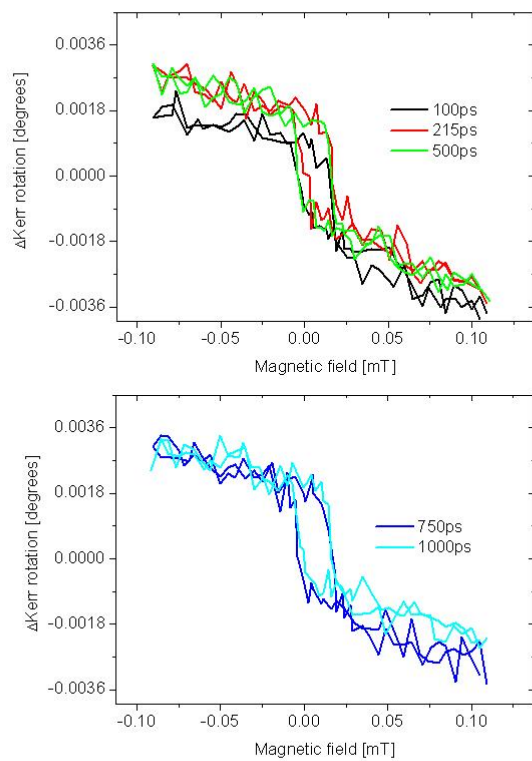


Figure B.3: *Transient hysteresis for sample 4 at 30 K for different pump probe delays.*

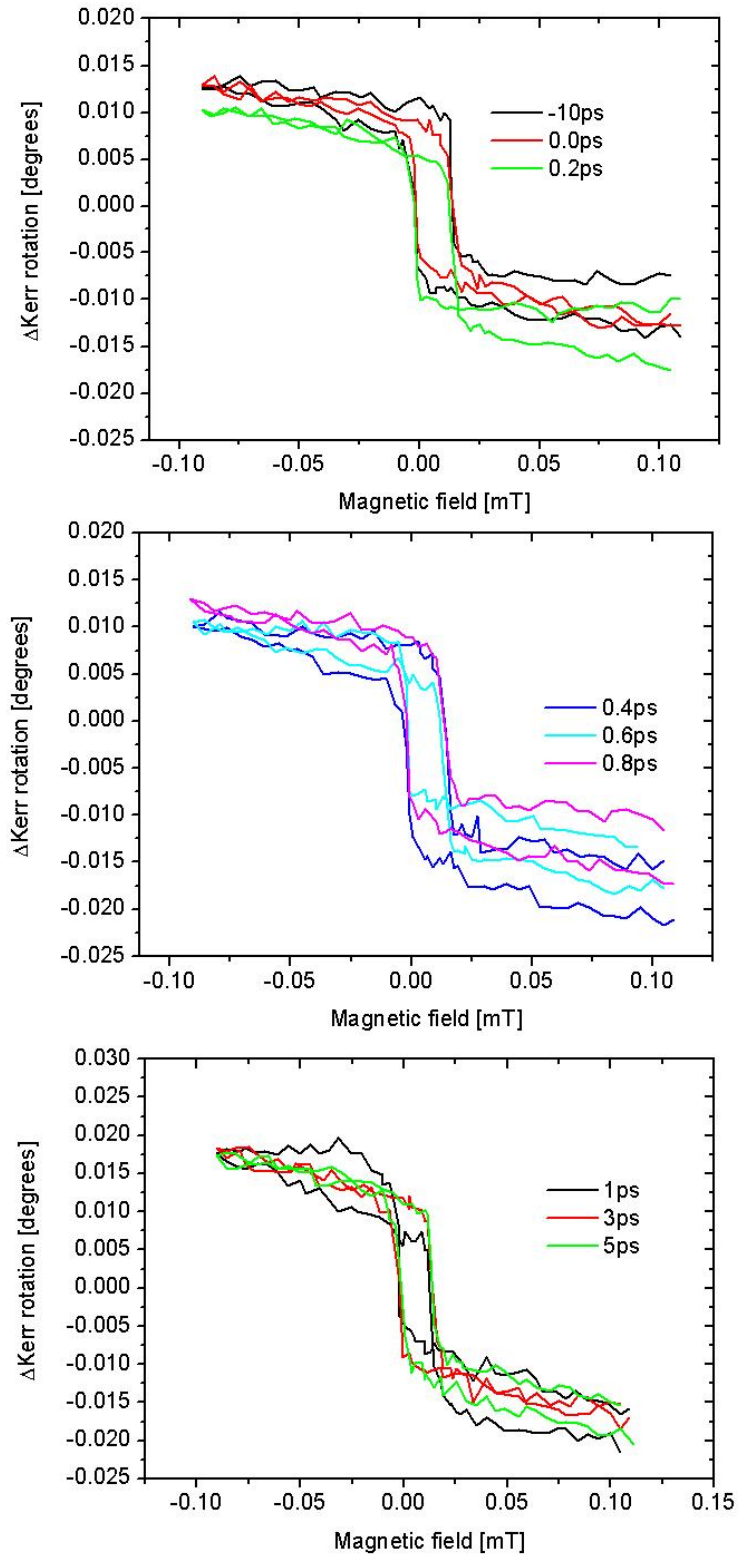


Figure B.4: Transient hysteresis for sample 4 at 40 K for different pump probe delays.

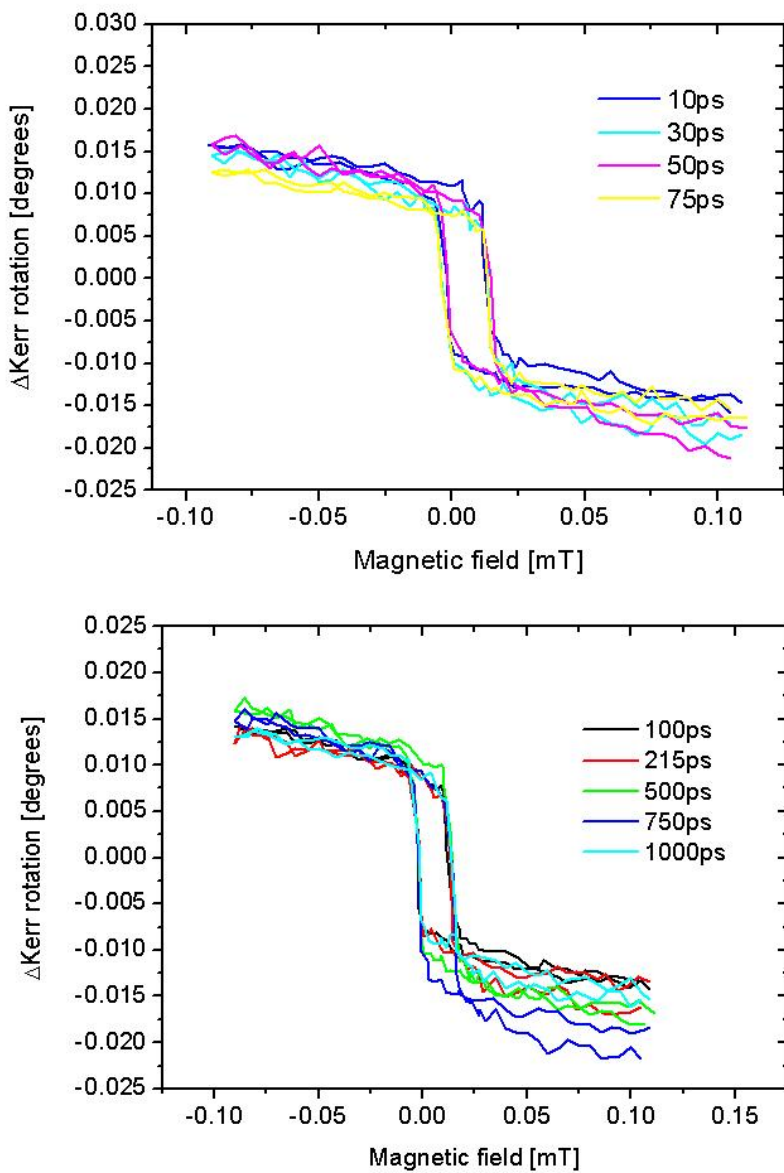


Figure B.5: *Transient hysteresis for sample 4 at 40 K for different pump probe delays.*

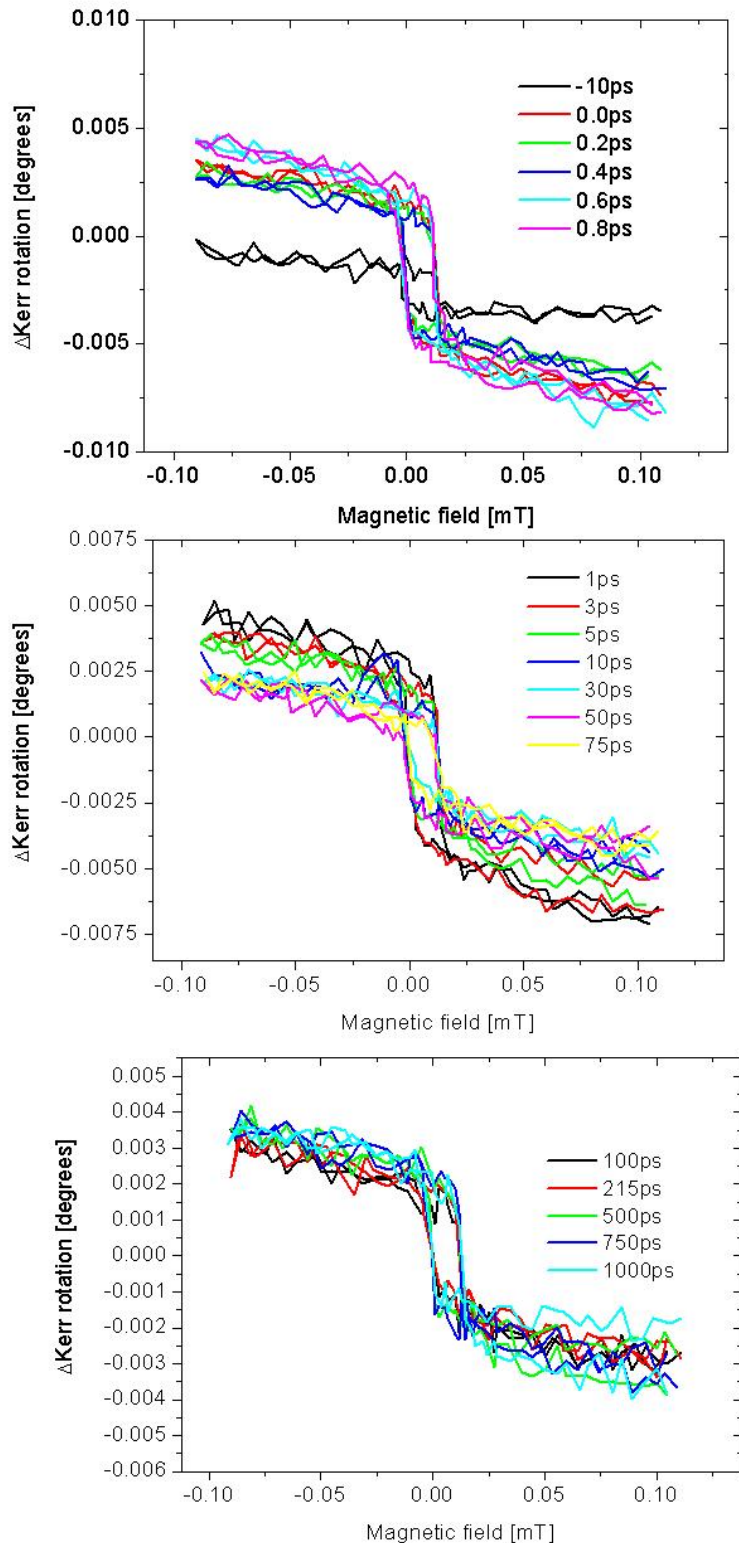


Figure B.6: *Transient hysteresis for sample 4 at 50 K for different pump probe delays.*

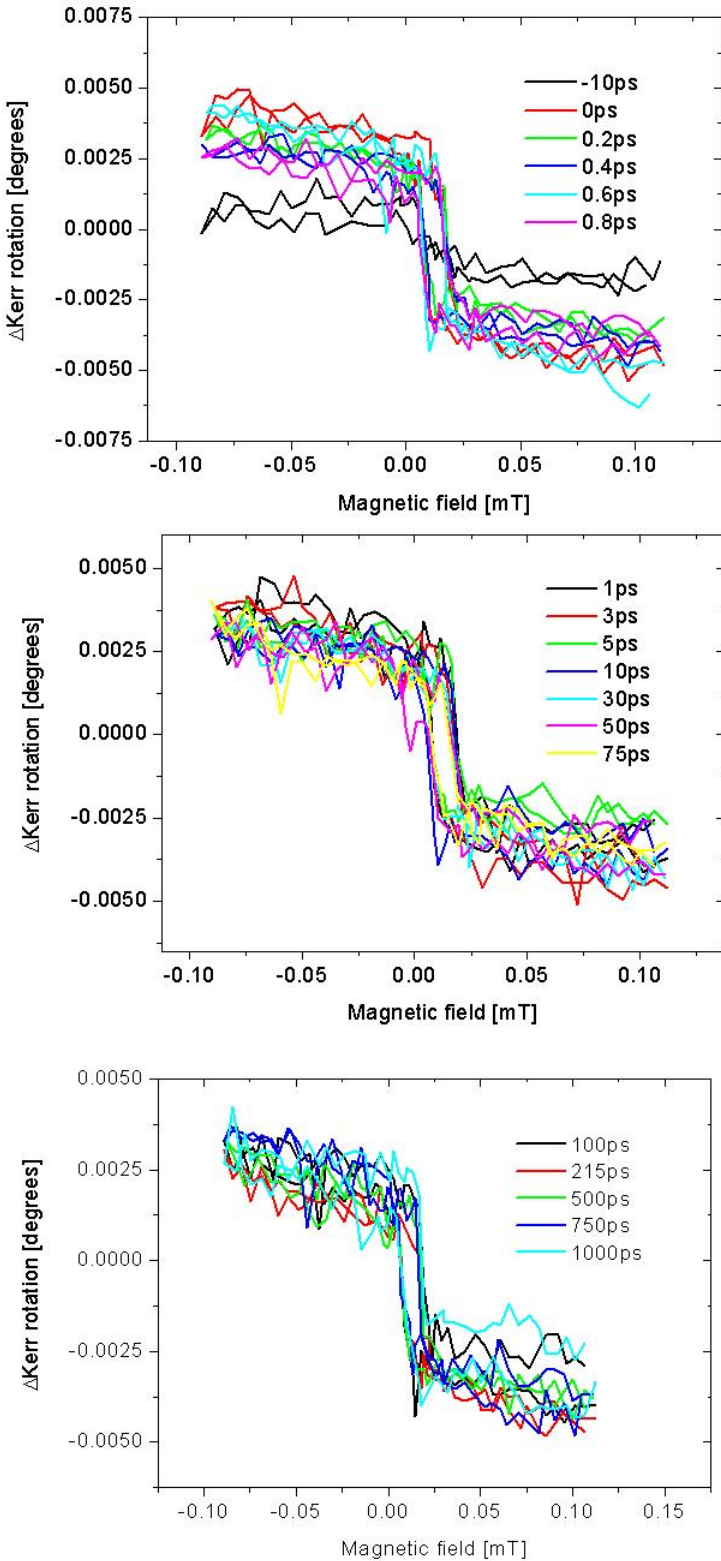


Figure B.7: Transient hysteresis for sample 4 at 60 K for different pump probe delays.

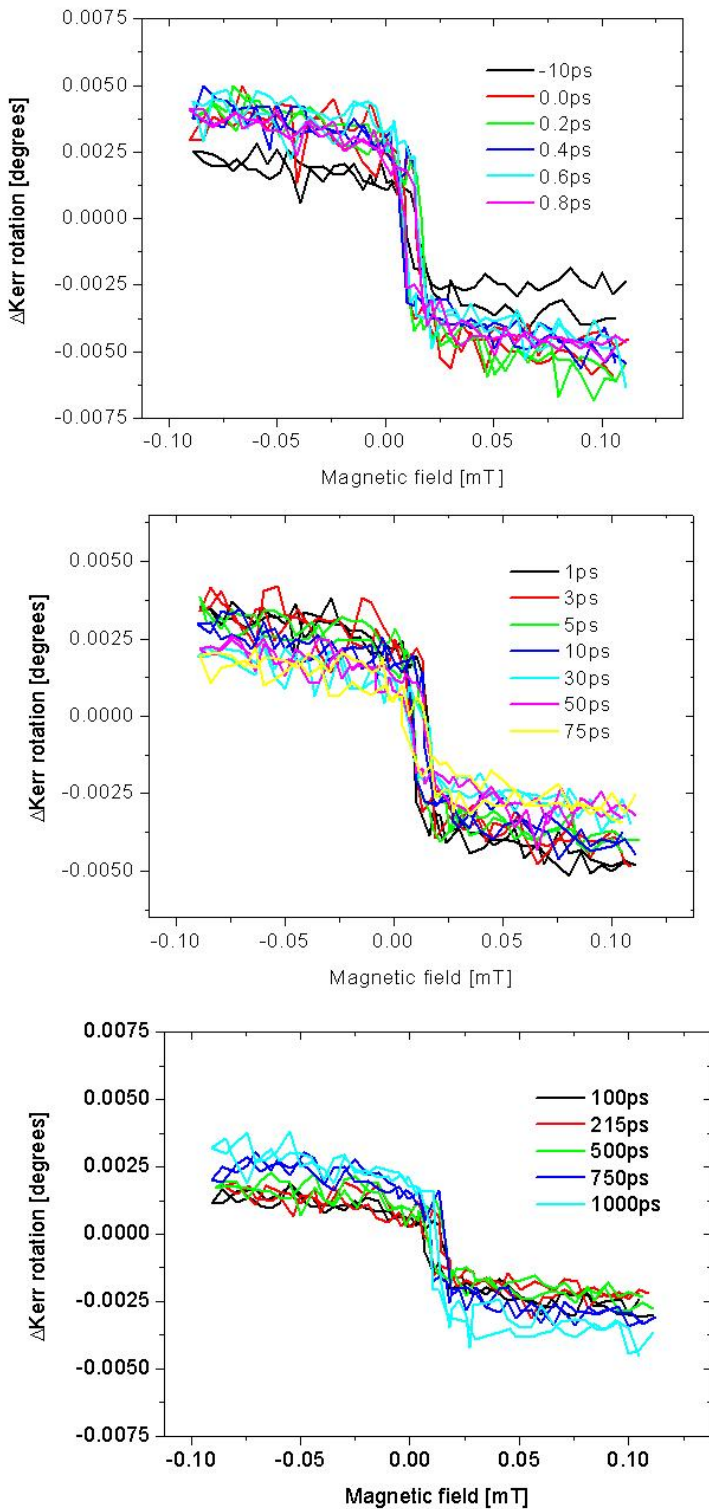


Figure B.8: *Transient hysteresis for sample 4 at 64 K for different pump probe delays.*

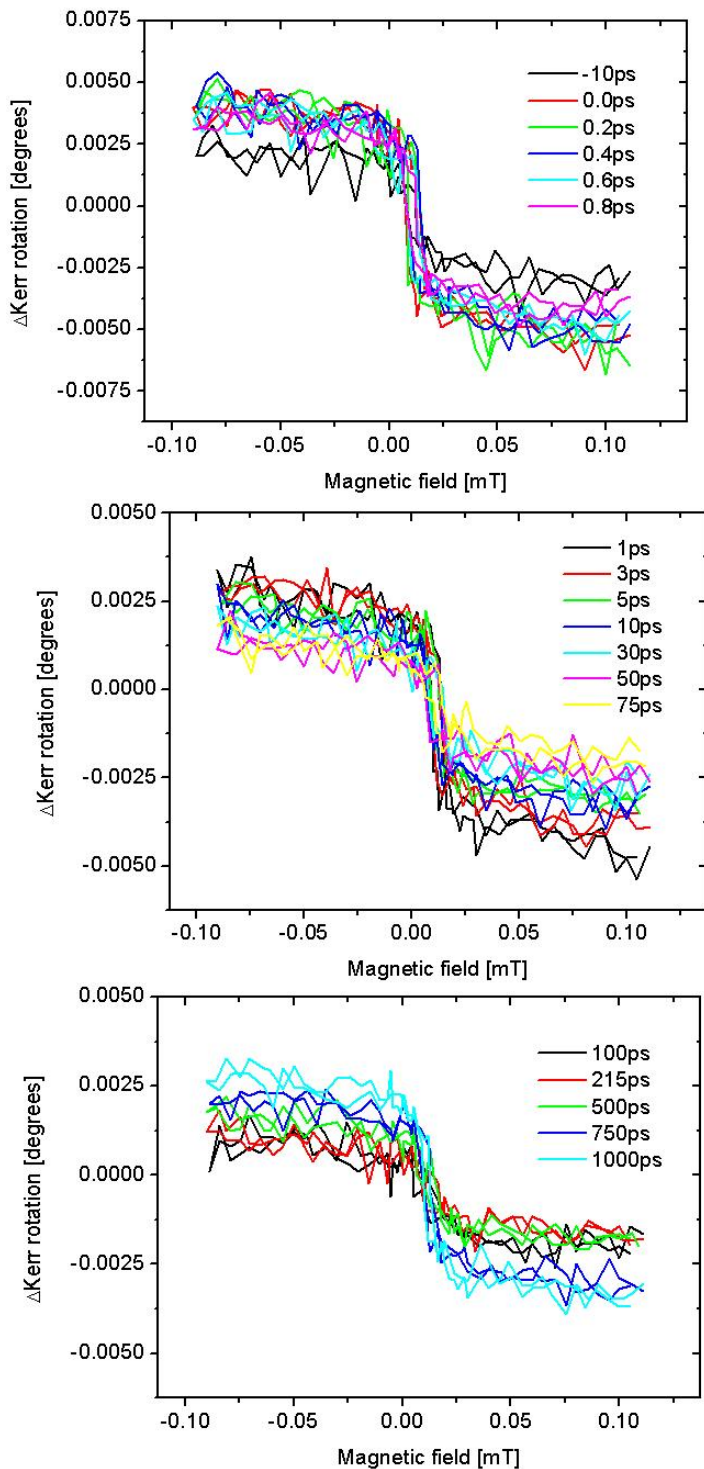


Figure B.9: *Transient hysteresis for sample 4 at 66 K for different pump probe delays.*

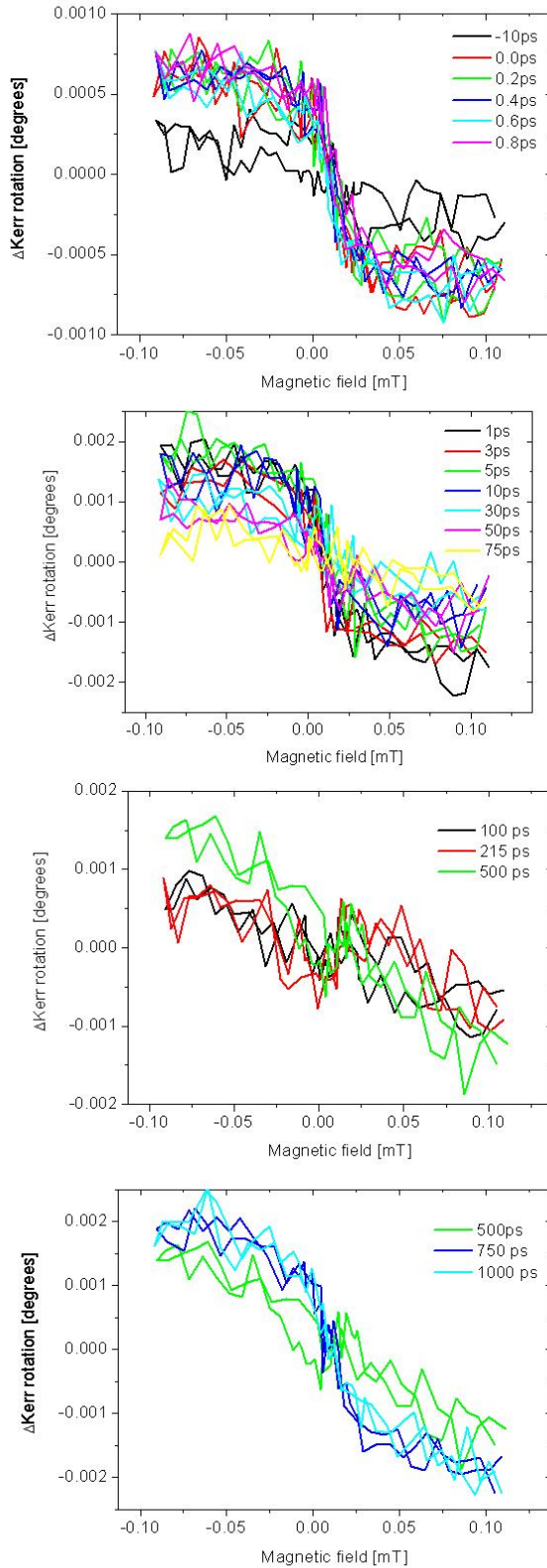


Figure B.10: *Transient hysteresis for sample 4 at 69 K for different pump probe delays.*

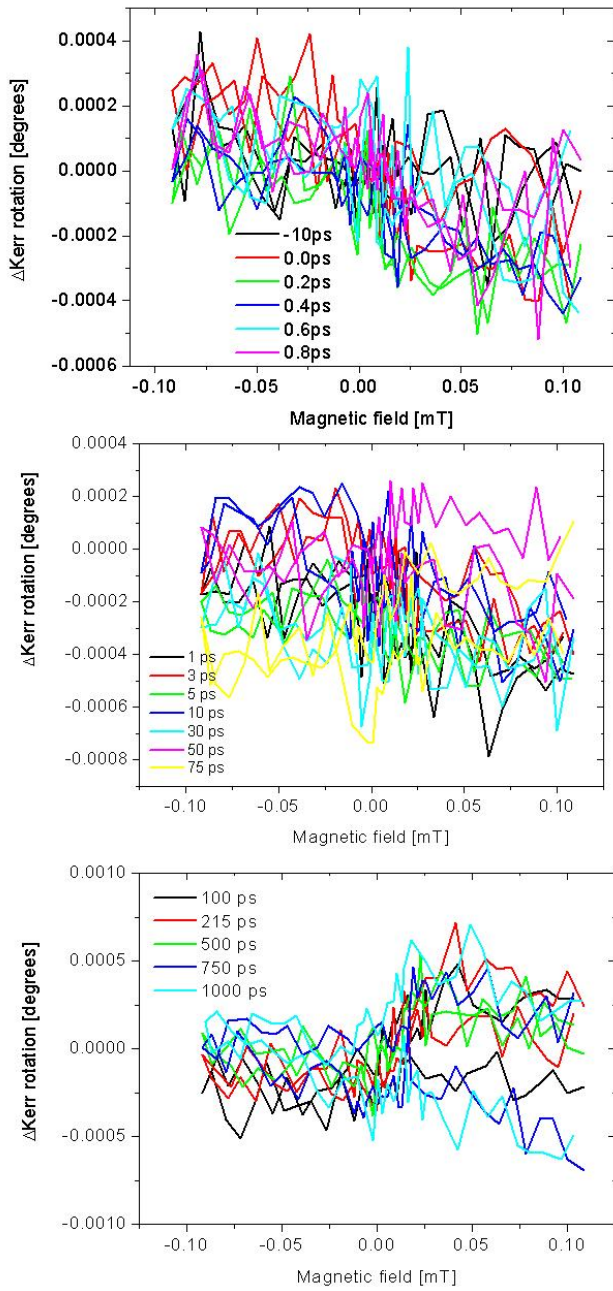


Figure B.11: *Transient hysteresis for sample 4 at 72 K for different pump probe delays.*

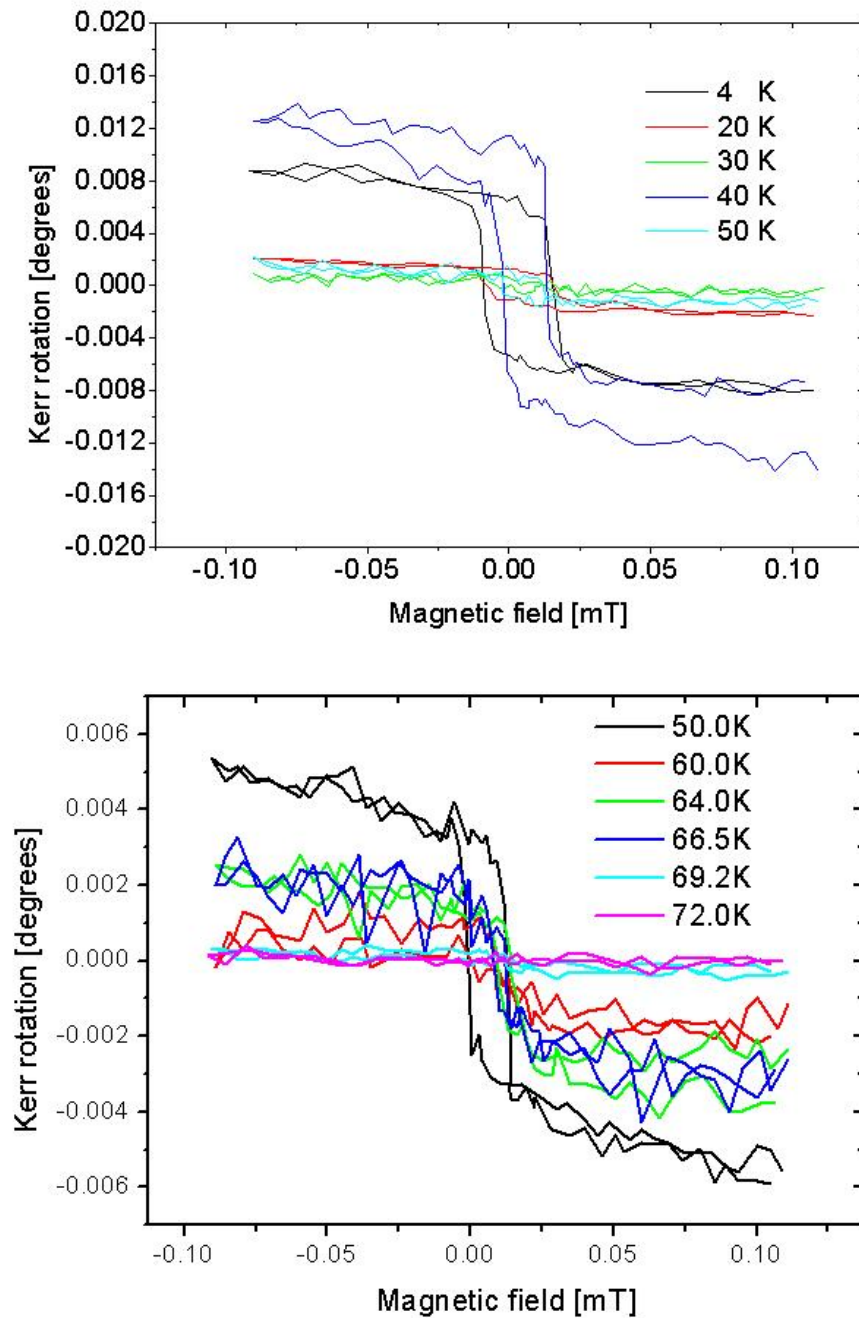


Figure B.12: *Transient hysteresis for sample 4 at -10 ps for different temperatures.*

Appendix C

Transient Kerr Rotation

In this section the transient Kerr rotation (dynamics) data for sample 1 are shown, measured with 800 nm pump and probe beams with a 45 degree angle of incidence for the probe. Transient Kerr rotation dynamics are measured at different temperatures. The applied magnetic field makes a angle of 45 degrees with the film plane. The pump fluence is about 1 mJ/cm².

The lines are shifted in such a way that the signal at minus delays is at $\Delta\theta=0$. Before this shift, all signals at negative delays were at negative $\Delta\theta$ indicating that is an induced demagnetization. The dotted lines represents the amount of $\Delta\theta$ by which the lines are shifted: the black line for 20 K, the red line for 30 K and so on. Stays the $\Delta\theta$ signal below the dotted line, then it still corresponds to an induced demagnetization. However, when the signal is above the dotted line, then there is an induced magnetization.

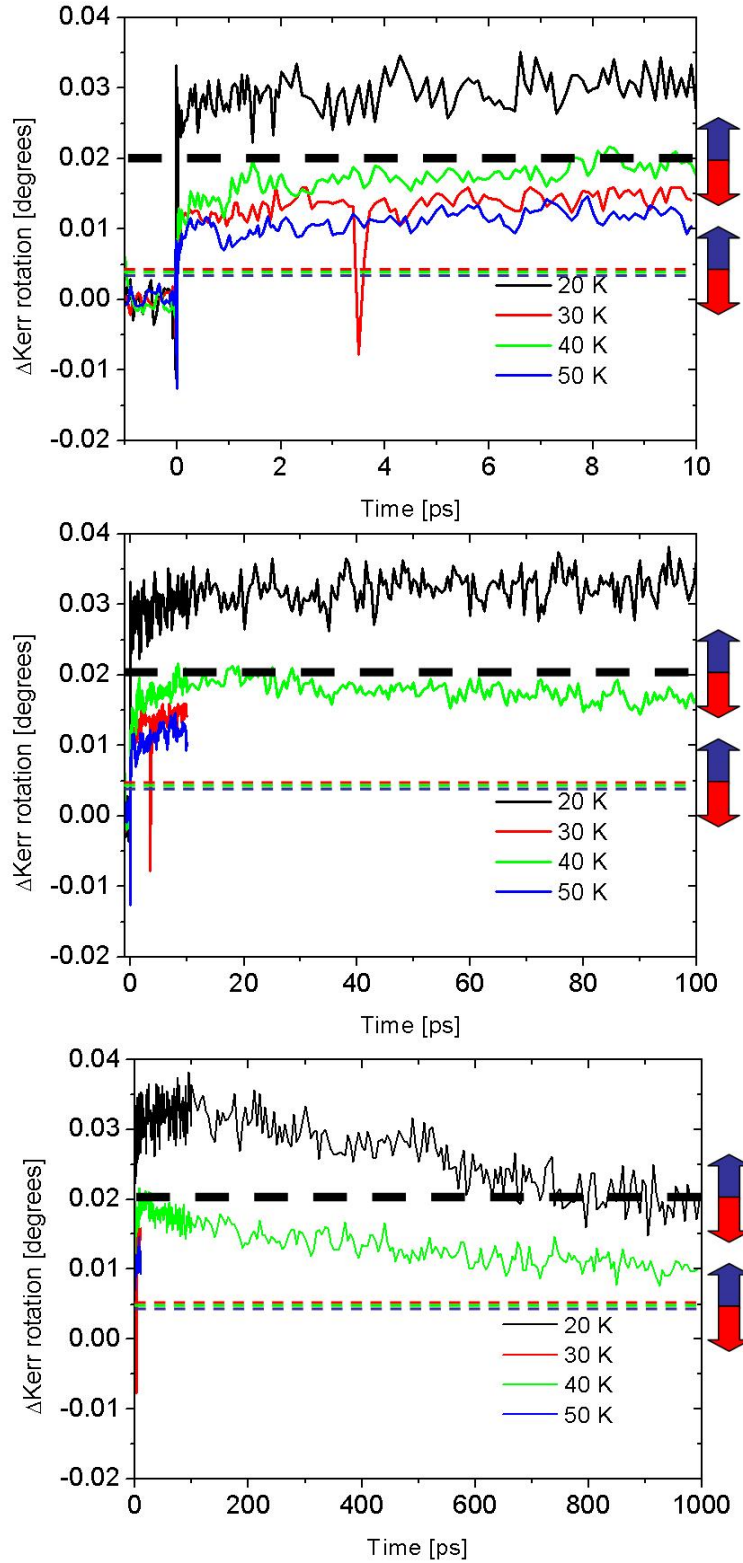


Figure C.1: *Transient Saturation Kerr rotation of sample 1 for different temperatures. The different graphs have different time windows.*

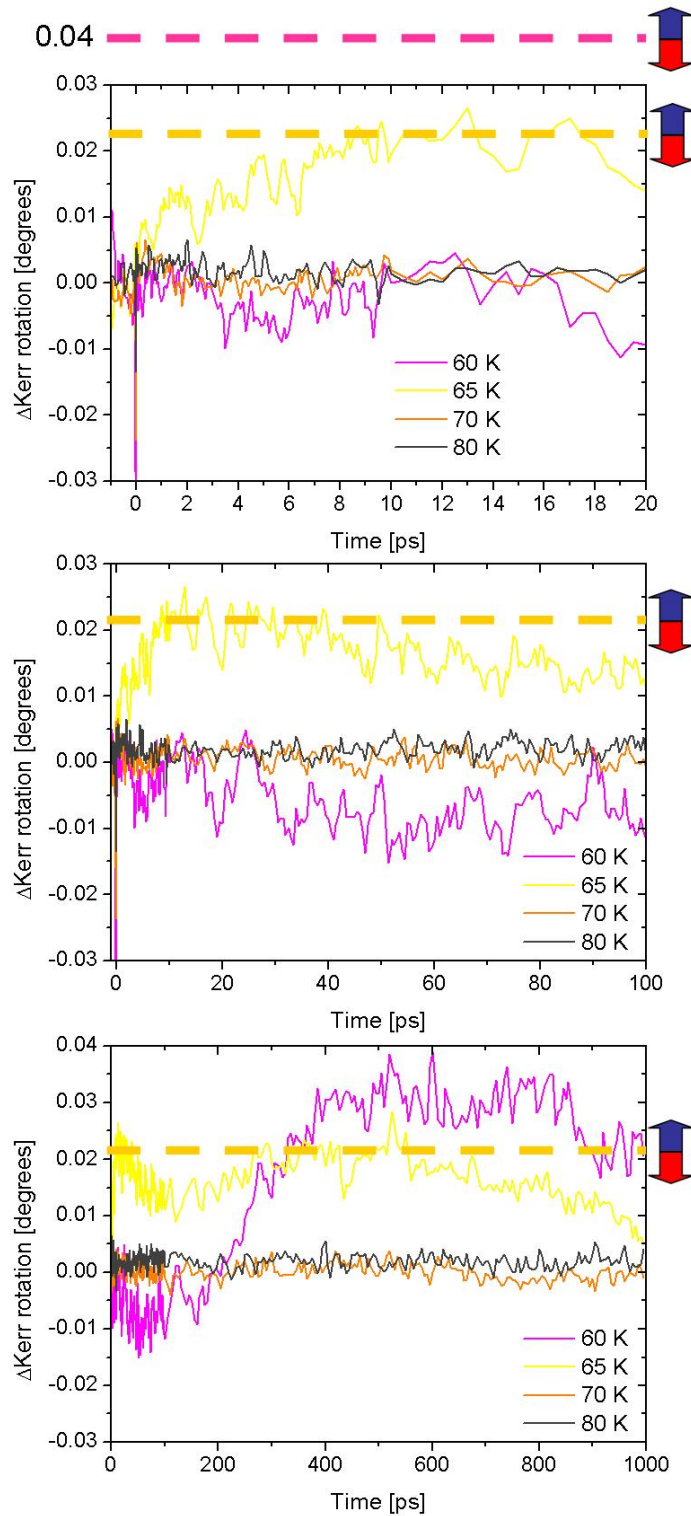


Figure C.2: Transient Saturation Kerr rotation of sample 1 for different temperatures. The different graphs have different time windows.

Appendix D

Transient Reflectivity

In this section the transient reflectivity (dynamics) data for sample 1 are shown, measured with 800 nm pump and probe beams with a 45 degree angle of incidence for the probe. Transient reflectivity dynamics are measured at different temperatures. The applied magnetic field makes a angle of 45 degrees with the film plane. The pump fluence is about 1 mJ/cm^2 . The transient reflectivity data are measured at the same time as the transient Kerr rotation measurements.

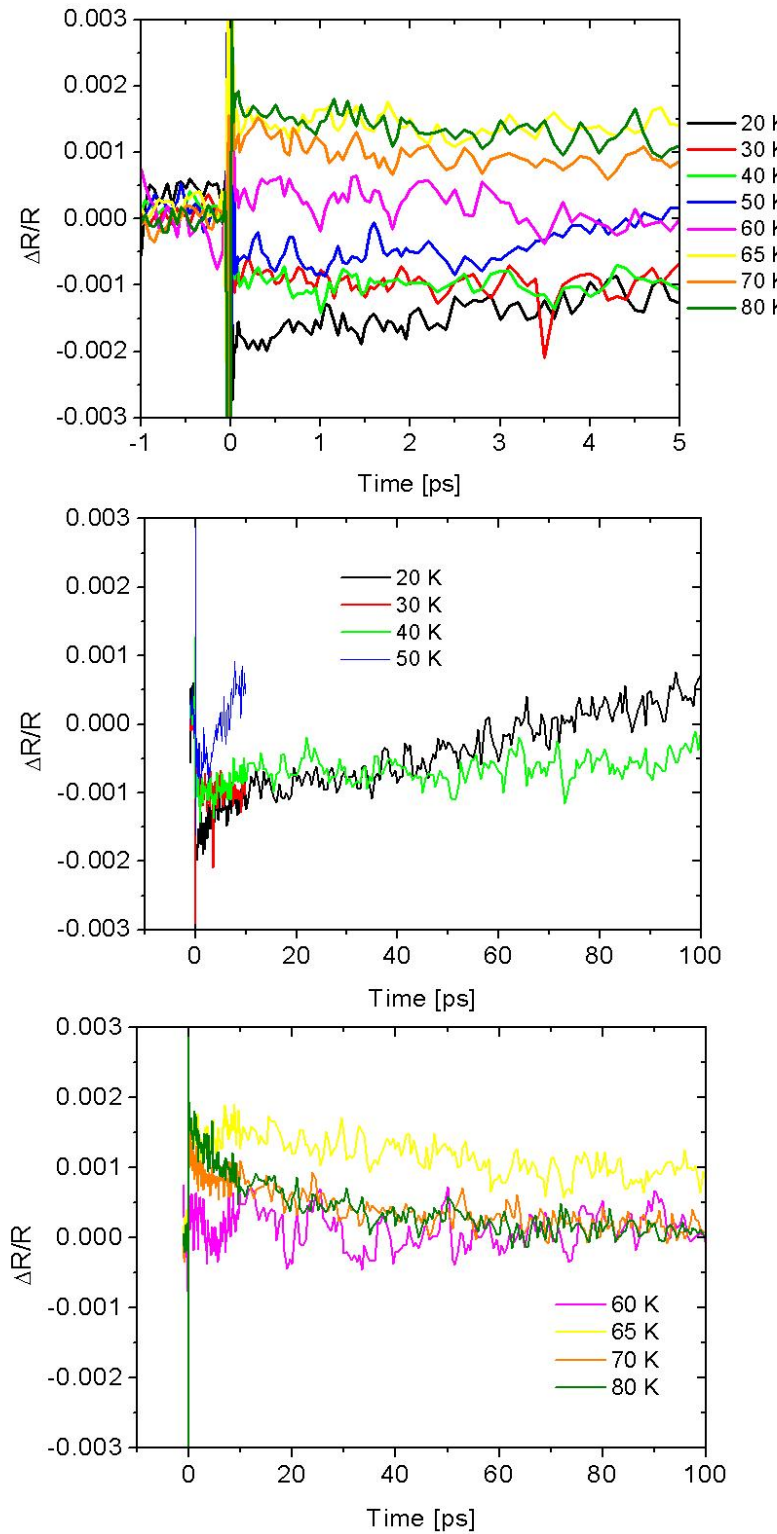


Figure D.1: Transient Reflectivity of sample 1 for different temperatures. The different graphs have different time windows and different temperatures.

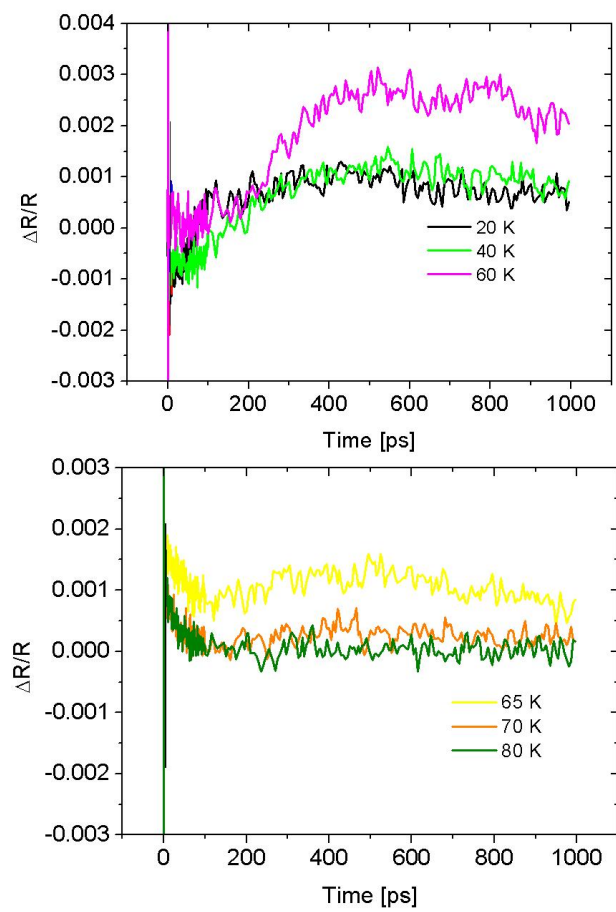


Figure D.2: *Transient Reflectivity of sample 1 for different temperatures. The different graphs have different time windows and different temperatures.*